HOT-TORSION EXPERIMENTS ON ALUMINUM AND ALUMINUM ALLOYS

by

Ufuk BALKIR

B.S. in A.E., İstanbul Technical University, 1983

Submitted to the Institute for Graduate Studies in Science and Engineering in partial fulfillment of the requirements for the degree of

Master of Science

in

Mechanical Engineering

Boğaziçi University

1986

HOT-TORSION EXPERIMENTS ON

ALUMINUM AND ALUMINUM ALLOYS

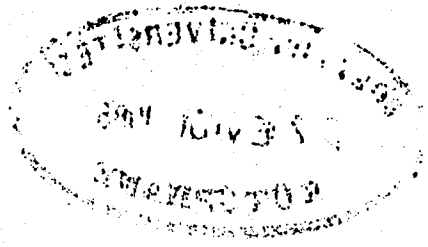

APPROVED BY

Doç. Dr. Sabri Altıntaş
(Thesis Supervisor)

S. Altıntaş

Yrd. Doç. Dr. Turan Özturan

Doç. Dr. Öktem Vardar

DATE OF APPROVAL: 3.7.1986

ACKNOWLEDGEMENTS

I would like to express my most sincere appreciation to my thesis supervisor Doç. Dr. Sabri ALTINTAŞ for his most helpful advice and guidance throughout the course of this work.

I also wish to express my gratitude to Prof. Dr. Şefik GÜLEÇ, Head of the Material Research Department, for permission to carry out this research in TÜBİTAK.

My grateful appreciation goes to Dr. Mustafa GEVREK for his invaluable guidance in theoretical work, to Mr. Suat TUNCEL for photography, and to Mr. Sinan ONURLU and Mr. Mehmet DEMİRKOL for extremely useful discussions.

I am particularly grateful to Mr. Sadettin OZAN and Mr. Sadullah OTUK for their careful work in specimen preparation and assistance in performing the tests.

Finally, I wish to thank all technical staff of the Material Research Department for their assistance.

June, 1986 Ufuk BALKIR

HOT-TORSION EXPERIMENTS ON ALUMINUM AND ALUMINUM ALLOYS

ABSTRACT

In this study, the effects of temperature and strain rate on the deformation behaviour of aluminum 1100 and aluminum 2024 are investigated.

The fundamentals of hot-torsion tests are briefly reviewed and testing methods are explained in detail. Then two important concepts used in data evaluation are introduced: critical radius and effective length.

In the experimental work, specimens are tested at different temperatures and strain rates under the effect of torsional loading. For both materials, temperature and strain rate are found to be effective not only on the magnitude of the flow stress, but on the shape of the flow curve as well. The strain-rate-sensitivity of materials increased parallel to the increase in temperature.

ÖZET

Bu çalışmada, sıcaklık ve genleme hızının alüminyum 1100 ve alüminyum 2024 malzemelerinin şekil değişimi davranışı üzerindeki etkileri incelenmiştir.

Sıcak burulma deneylerinin esasları kısaca gözden geçirilmiş ve deney yöntemleri ayrıntılı olarak açıklanmıştır. Ardından verilerin değerlendirilmesinde kullanılacak olan iki önemli kavram tanıtılmıştır: kritik yarıçap ve etkin uzunluk.

Deneysel çalışmada ise, numuneler farklı sıcaklıklarda ve farklı genleme hızlarında burulma yükü etkisi altında bırakılmışlardır. Her iki malzeme için de sıcaklık ve genleme hızının sadece akma gerilmesinin değeri üzerinde değil, aynı zamanda akma eğrisinin şekli üzerinde de etkili olduğu gözlenmiştir. Sıcaklık artışı ile birlikte malzemelerin genleme hızına olan duyarlılıkları da artmaktadır.

TABLE OF CONTENTS

LIST OF FIGURES

page

LIST OF TABLES

LIST OF SYMBOLS

K	:	Constant used in equations (19), (41), and (56).
L	:	Gage length of specimen.
L_E	:	Effective length of specimen.
L_{EI}, L_{EII}	:	Effective lengths of specimens with $L=0$ and $L\neq 0$, respectively.
m	:	Strain rate sensitivity index.
M	:	Twist moment, torque.
n	:	Strain hardening exponent.
p	:	A material parameter equal to the sum of strain rate sensitivity index and strain hardening exponent.
r	:	Local radius.
r^*	:	Critical radius.
R	:	Specimen radius.
R_i	:	Internal radius of a tubular specimen.
R_E	:	The contribution of a transition zone to deformation.
R_N	:	Notch radius.
$R(x)$	:	The function of variation of radius along the axis of specimen.
S	:	Slope of torque-radius curve.
T	:	Temperature.
x	:	Variable changing along the axis of specimen.
y	:	Variable changing in perpendicular direction of the specimen axis.

γ, γ_R : Shear strain at specimen surface.

$\dot{\gamma}$, $\dot{\gamma}_R$: Shear strain rate at specimen surface.

γ_r : Shear strain at local radius r.

$\dot{\gamma}_r$: Shear strain rate at local radius r.

γ^* : Shear strain at critical radius.

$\dot{\gamma}^*$: Shear strain rate at critical radius.

ε : True strain.

$\dot{\varepsilon}$: True strain rate.

θ : Twist angle.

$\dot{\theta}$: Rate of change of twist angle.

ϑ : Twist rate to twist ratio.

σ : Flow stress.

ζ : Shear stress.

$\overline{\zeta}$: Shear stress that is assumed constant for differential testing method.

ζ_i : Shear stress at the internal radius of a tubular specimen.

I. INTRODUCTION

The mechanical behaviour of metals at high temperatures and under high rates of deformation is a subject that has received considerable attention in recent years /1-4/. This interest is mainly originated from the extensive usage of hot forming processes of metals in industry. Many important metal forming techniques, such as rolling, drawing, forging and extrusion necessitate an understanding of the plastic behaviour of various metals and alloys for their successful forming under different working conditions.

From engineering point of view, the knowledge of metals' behaviour is of great importance when deciding upon such practical considerations as the selection of a machine tool and the allocation of available equipment for different forming processes. In view of research purposes, on the other hand, this is fundamental to the understanding of the laws and mechanisms governing deformation processes.

Calculation of the optimum parameters for a given deformation and the improvement of a metal-forming technique require the knowledge of the relationship between flow stress and the parameters affecting it. From this point of view, material flow curves (stress-strain curves) are the main sources of knowledge that facilitates the

understanding of metals' behaviour.

Flow stress is an important parameter in mechanical working. This term is taken to be the true stress which initiates plastic deformation in a material under a uniaxial state of stress.The flow stress is a function of true strain, strain rate, temperature and the structure of the material. Within the term "structure", many variables are included. For example, chemical composition, method of production, heat treatment, precipitates, phase- and grain boundaries and their textures, segregations, dislocation densities and dislocation arrangements are structural parameters. In some studies /5,6/, however, these parameters are assumed to be well defined and do not change appreciably during a plastic deformation process; hence their influence is not considered. In this case, the flow stress of a material is related to process parameters such as true strain ε, strain rate $\dot{\varepsilon}$ and temperature T, in the following form:

$$\sigma = f(\varepsilon, \dot{\varepsilon}, T) \qquad (1)$$

It is not possible, however, to express the flow stress in terms of true strain at various temperatures and strain rates by a single mathematical equation which is valid for all materials. These parameters must therefore be obtained from experimental studies carried out at the temperatures and strain rates that actually exist during the forming operation for each material.

Hot torsion testing /7-14/ is an increasingly popular method in determination of the flow stress at various strains, strain rates, and temperatures. From many points of view, it has advantageous aspects

over other testing methods used for the same purpose, i.e. tension, compression, and upsetting tests. In this method, high strains can be attained at constant surface strain rate and without plastic instability. Hot torsion testing is also a very convenient tool for hot-workability studies /15-19/.

The purpose of the present investigation that employes hot-torsion technique can be summarized as follows:

a. to study the mechanisms governing the deformation process of aluminum-base materials at high temperatures;

b. to obtain the flow curves of aluminum 1100 and aluminum 2024;

c. to study the effects of temperature and strain rate on the flow stress and on the shape of the flow curve;

d. to examine the temperature effect on strain rate sensitivity of aluminum-base materials;

e. to observe the effects of temperature and strain rate on length changes of aluminum under the effect of torsional loading.

In the following, Section II is a brief review of the fundamentals of hot-torsion testing method. Different testing techniques will be given in Section III. In Section IV, the important concepts used in data evaluation will be explained. The experimental work and results will be presented in Sections V and VI, respectively. Then an interpretation of the results and a comparison with the previous studies will be given in Section VII. In the last section, the conclusions of this study will be cited.

II. FEATURES AND APPLICATIONS OF HOT-TORSION TESTING METHOD

The hot torsion test has been in general use since 1950's and several reviews /15,17,19/ have compared this technique with other methods that are used to simulate industrial hot working processes. In recent years, much work has been focused on finding new methods that provide high loading rates; and, with the advance of new and sophisticated testing techniques /2,4,13/ , loading rates have been extended into dynamic range. Today, hot torsion tests at constant true strain rates in the range of 10^{-5} to 10^{4} rad/s can be carried out up to very high strains with no plastic instability.

2.1. CHARACTERISTIC FEATURES

In a torsion test, the mode of deformation is shear and, therefore, theoretically deformation should occur without any change in dimensions of the sample. This means that by twisting the test piece at a fixed angular velocity a constant true strain rate can be obtained up to the start of fracture. From this point of view, torsion test is very convenient for testing materials at elevated temperatures, when the material's behaviour depends strongly on the strain rate. With tension and compression testing methods, on the

other hand, constant true strain rates are very difficult to obtain even if specially shaped cams are used.

The hot torsion test is capable of producing true strains of the order of 20. The true strains attainable by tensile and compression tests are 0.3 and 2.3, respectively. In the latter methods, uniaxiality of stress is lost when necking or barreling occurs. Therefore, complicated measuring techniques are required to extend the analysis beyond the region of uniform strain and a considerable amount of work is also needed in the calculation of flow stress and true strain.

Hot torsion tests are necessary for simulation to many industrial metal forming processes, because the strain rates that conventional tensile-testing and compression-testing machines give are considerably lower than those prevailing during these operations.

When the shear stresses and strains are converted to equivalent tensile stresses and strains according to the Von Mises criterion, torsion flow curves are almost identical to tension or compression flow curves for the same strain rate and temperature. The inter-dependence of surface strain rate, effective stress and temperature is the same as that for compression and tension tests.

The main problem in torsion testing is the non-uniform variation in strain and strain rate across the specimen cross section, where they increase from zero on the axis to maximum values at the surface. It is the surface values which are commonly reported. This variation gives rise to problems of interpretation, because the surface work hardens more than the core and the mechanisms of deformation may be different. The use of tubular specimens largely avoids these difficulties,

but gives rise to others. If the wall thickness is reduced too greatly, the specimen will fail by buckling rather than by torsion.

In the course of a torsion test, if the stationary end is free to move in axial direction, the specimen may change length, giving rise to changes in torsional strain and strain rate. The dilatation may either be extension (aluminum), or contraction (most materials including steels) and, for certain materials and conditions, may reverse as the test proceeds /15,19,20/. This length changes can be taken into account in the calculation, although the extra effort spent in measurement and analysis is seldom worthwhile. If the stationary end of the sample is not free to move axially, induced tensile or compressive stresses arise and alter the stress state. While these longitudinal stresses are usually small compared to the shearing stresses and can be ignored, they may be important in influencing the torsional strain to fracture. In tubular specimens, longitudinal compressive stresses are accompanied by radial bulging of the gage section.

Like all other testing techniques and processes, heat is generated during torsional deformation and hence temperature changes occur. If the deformations are applied slowly, such as in quasi-static loading conditions, the heat is conducted away from the deformed regions and the entire body is essentially in an isothermal condition. At the other extreme, when deformations are rapidly applied by the high velocity impact or explosive loading, the process is essentially adiabatic; the generated heat does not have time to redistribute. For intermediate rates of deformation, however, it is important to consider both the heat generation and the heat conduction. Different numerical

techniques have been employed /21-23/ for calculating radial and axial temperature distribution during torsion testing.

2.2 APPLICATIONS

Torsion test at high temperatures is a widely used method for hot workability studies /15-19/ and for simulation to industrial hot working processes /24-28/, such as extrusion, drawing, forging and rolling.

Hot workability is the ability of a metal or alloy to be deformed under conditions of high temperature (0.5 T_m, where T_m is the melting temperature in degrees Kelvin) and relatively high strain rates (10^{-1} to 10^{3} s^{-1}). The two characteristics that govern hot workability are strength and ductility. By using hot torsion testing method, these two can be determined from torque-twist angle data and number of twists to failure, respectively. The superiority of the method is that high strains can be attainable at constant surface strain rate. Additionally, this method provides close control of variables, ease of determining optimum conditions for new materials, and a possibility for relating the structure to properties determined.

A simulation between industrial processes and hot torsion test can also be settled, on condition that the ranges of temperature, strain, strain rate, and intermittent deformation cycles of interest is reproduced. For example, processes such as extrusion, or rolling where the total strain is applied in one operation is simulated by stopping the test after a predetermined number of revolutions. Simulation of interrupted deformation can be carried out by programming

an electromagnetic clutch in the drive system. A further variable in such operations is temperature because, in general, the temperature of the metal decreases continuously due to the large increase in area and consequent heat loss. In laboratory hot torsion tests, artificial cooling must be used to simulate the practical conditions.

Hot torsion test data may also be used directly to derive a suitable constitutive relationship for a material /5,17,29-39/. Calculation of the deformation of metals subjected to stresses between yield and fracture requires constitutive relations valid at large plastic strains. Many such relations connect $\sigma, \varepsilon, \dot{\varepsilon}$, T in a differential or closed analytical form. The values of material parameters appearing in these expressions depend on the thermo-mechanical history of the material. Therefore, some or all of the variables σ, ε, $\dot{\varepsilon}$ and T may not satisfy the requirements for state variables of the system. However, their usefullness in computations or their accessibility to experimental measurements often overrides fundamental objections, resulting in constitutive relations valid for a restricted range of material histories and deformation conditions.

In recent times, many advances have been made in numerical analysis methods - such as finite element technique - /40,41/ as a means of solving metal forming problems. The success of these methods depends very much upon the availability of basic material-property data. For high strains, these data are supplied from hot torsion test results.

III. TORSION TESTING METHODS

During the torsional deformation torque M is registered as a function of the angle of twist θ . The accurate conversion of the torque-twist data into equivalent strain-equivalent stress data is required for reliable formability predictions, particularly at large strains.

The conversion process consists of two stages. Firstly, the shear stress ζ is calculated from the torque M and the shear strain γ from the angle of twist θ . Then a yield criterion is used for calculation of equivalent strain and equivalent stress.

For the first stage, it is usually assumed that the following conditions concerning specimen geometry and material are fulfilled /42/ :

i) The specimen does not have any notch;

ii) The material is isotropic, homogeneous, and incompressible.

Therefore, a proportionality can be considered between shear strain and the radial distance r (Figure 1) :

$$\gamma_r(\theta) = \frac{r\,\theta}{L} \qquad \text{for} \quad 0 \leqslant r \leqslant R \tag{2}$$

where L is the gage length and θ is the angle of twist.

As can easily be seen, the shear strain varies from zero at the axis of the specimen to maximum at the surface:

$$\gamma_R(\theta) = \frac{R\,\theta}{L} \tag{3}$$

Here, R is the specimen radius and L is the gage length.

The strain rate varies in a similar manner:

$$\dot{\gamma}_r = \frac{r\,\dot{\theta}}{L} \quad , \quad \dot{\gamma}_R = \frac{R\,\dot{\theta}}{L} \tag{4}$$

where $\dot{\theta}$ is the rate of change of twist angle.

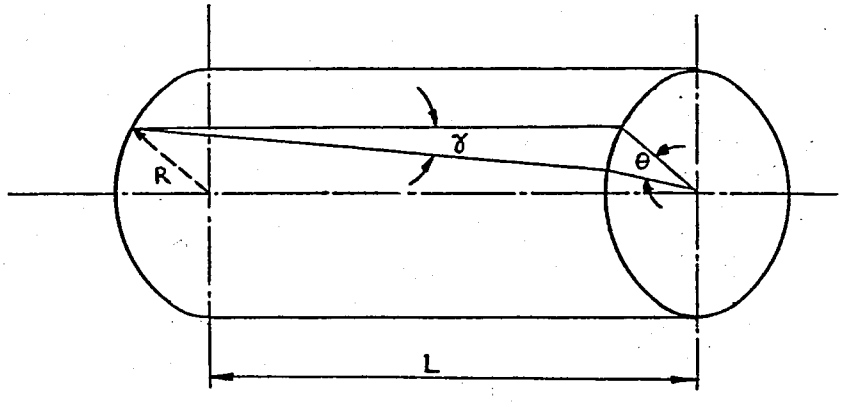

Figure 1 - Scheme of Torsion Test on Solid Specimens.

At any instant during twisting, the shear stress ζ which depends on both γ and $\dot{\gamma}$ will be an unknown function of r. The calculation of shear stress from the torque is rather difficult

since the torque only gives information about shear stress through the integral equation:

$$M = 2\pi \int_0^R \zeta r^2 dr \qquad (5)$$

where M is the developed torque, R is the radius of the specimen, and r is the local radius inside the specimen.

The existing evaluation techniques of equation (5) are reviewed below.

3.1 NADAI'S METHOD

This well-known method requires that the shear stress depends only on the shear strain /43/. Therefore its use is restricted to strain rate insensitive materials. Accordingly, it cannot be applied at elevated temperatures, where the rate sensitivity is no longer negligible.

All the assumptions made are given below:

i) the material is homogenous and isotropic;

ii) shear stress is a function of only shear strain;

iii) the relative rotation of cross-sections is proportional to the distance between them;

iv) radii remain straight;

v) plane sections remain plane during twisting.

If the variable r in equation (5) is changed into γ by using the relationships (2) and (3):

$$M = \frac{2\pi R^3}{\gamma_R^3} \int_0^{\gamma_R} \zeta(\gamma)\gamma^2 d\gamma \qquad (6)$$

Since the function $\zeta = \zeta(\gamma)$ is not known, this integration cannot be carried out. In this case, a mathematically rigorous determination of shear stress is only possible for a singular radial distance, the surface of test piece. That is, if M is considered only as a function of γ_R, equation (6) can be differentiated with respect to γ_R and the following equation, known as Nadai's formula, is obtained:

$$\zeta = \zeta(\gamma_R) = \frac{1}{2\pi R^3}\left(3M + \gamma_R \frac{dM}{d\gamma_R}\right) \qquad (7)$$

This famous equation can also be written in the following form:

$$\zeta = \zeta(\theta) = \frac{1}{2\pi R^3}\left(3M + \theta\frac{dM}{d\theta}\right) \qquad (8)$$

According to the Nadai's formula, the flow curve of a material can be found from its torque-twist curve by using a graphical method. As can easily be seen from Figure 2, the following relationship exists between the variables, T and θ, and the graphical values :

$$3M + \theta\frac{dM}{d\theta} = 3\,\overline{AP} + \overline{CP} \qquad (9)$$

Therefore equation (8) will take the final form:

$$\zeta = \frac{1}{2\pi R^3}\left(3\overline{AP} + \overline{CP}\right) \qquad (10)$$

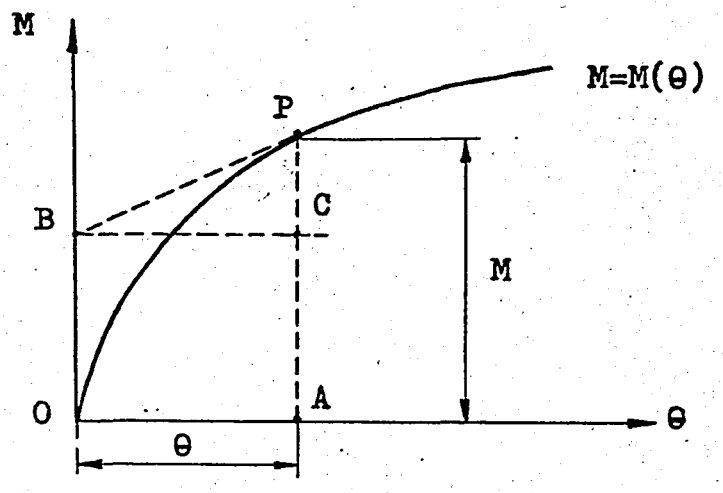

Figure 2 - Torque-Twist Angle Diagram.

A curve fitting computer program can be used to obtain the equation $M=M(\theta)$; then, with the use of another program shear stress can be calculated from equation (10).

Since it has the advantage of a graphical solution, Nadai's method has been extensively used at room temperature studies /44-46/.

This method can also be extended to give the shear stresses in tubular specimens. For this purpose, an approximation of the form of equation (8) is suggested /47/ :

$$\tau = AM + B\theta \frac{dM}{d\theta} \qquad (11)$$

where A and B are constants. In order to find suitable values of A and B, elastic and fully-plastic solutions for the shear stress are used as boundary conditions. Taking R_i as the inner diameter of tubular specimen, elastic and fully plastic solutions are given in the following forms, respectively.

$$\zeta = \frac{2\,R\,M}{\pi\,(R^4 - R_i^4)} \tag{12}$$

$$\zeta = \frac{3\,M}{2\pi\,(R^3 - R_i^3)} \tag{13}$$

Inserting the values of ζ from equations (12) and (13) in equation (11), with $\theta\,(dM/d\theta)$ equal to M and zero respectively, one obtains two simultaneous equations for A and B. Solving these, equation (11) becomes :

$$\zeta = \frac{1}{2\pi}\left[\frac{3M}{R^3 - R_i^3} + \left(\frac{4R}{R^4 - R_i^4} - \frac{3}{R^3 - R_i^3}\right)\theta\frac{dM}{d\theta}\right] \tag{14}$$

This equation is, of course, only an approximation. But it is clearly an exact solution for the elastic and fully plastic situations. It is also exact for the special case of a solid specimen since it reduces to equation (8) when R_i is zero. This solution also tends to be the correct solution for thin-walled tubes because it always lies between the upper and lower bound solutions for a strain hardening material (i.e. $dM/d\theta > 0$).

3.2 THE METHOD OF FIELDS AND BACKOFEN

Nadai's method requires modification for high temperature applications since it is based on the assumption that the stress is independent of strain rate. An analysis developed by Fields and Backofen /48/ considers the strong strain rate dependence of flow

stress at high temperatures and is built on Nadai's method.

Assumptions made in the derivation of Fields and Backofen formula are given below :

i) material is homogenous and isotropic;

ii) relative rotation of cross-sections is proportional to the distance between them;

iii) radii remain straight;

iv) plane sections remain plane during twisting;

v) shear stress ζ is a unique function of the current shear strain γ and shear strain rate $\dot{\gamma}$, without regard to the detailed history of the test, that is, to the twist and twist rate paths followed.

Fields and Backofen's formula given below

$$\zeta = \frac{M}{2\pi R^3}\left(3 + \frac{\theta}{M}\frac{dM}{d\theta}\right) \qquad (15)$$

is identical in form to equation (8), i.e. Nadai's formula, but it is not restricted to rate-insensitive materials. In the light of the last assumption stated above, the twist moment M can be considered as a unique function of the amount of twist θ and twist rate $\dot{\theta}$. In this case any current value of the twist moment M (for a given θ_1) obtained from an actual test at constant twist rate $\dot{\theta}_1$ can also be reached by a suitable special test conducted at an increasing twist rate given by $\theta = \varrho_1 \theta$, where $\varrho_1 = \dot{\theta}_1/\theta_1$ (Figure 3) /49/. Because of the assumed history independence of the material, a complete torque-twist curve for constant $\dot{\theta}$ can be constructed from suitably chosen data points

taken from the series of special tests conducted at decreasing values of ϱ. For the latter type of test, the last term of equation (15) can be expressed as

$$\left(\frac{\theta}{M}\right)\frac{dM}{d\theta} = \left(\frac{\theta}{M}\right)\left(\frac{\partial M}{\partial \theta}\Big|_{\dot{\theta}}\right) + \left(\frac{\theta}{M}\right)\left(\frac{\partial M}{\partial \dot{\theta}}\Big|_{\theta}\right)\frac{d\dot{\theta}}{d\theta} \qquad (16)$$

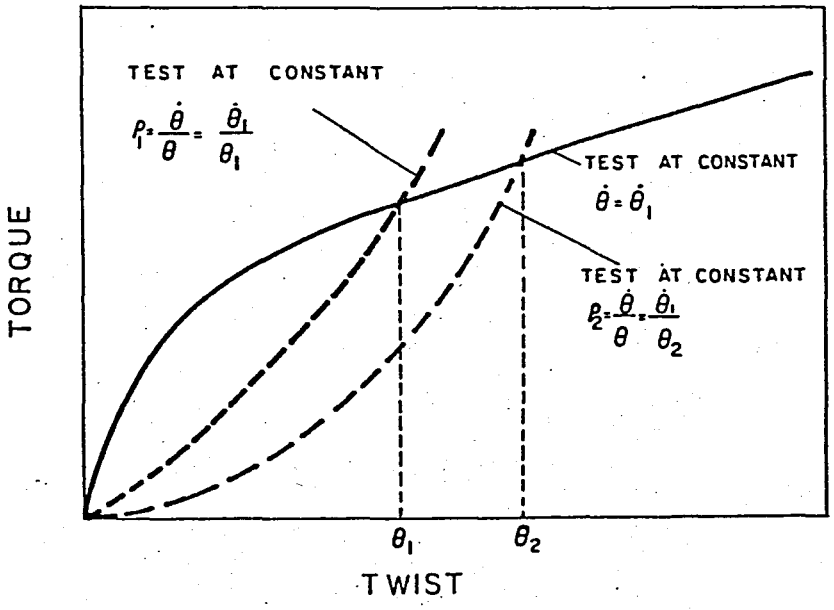

Figure 3 - Torque-twist Curves Obtained by Torsion Testing: at a Constant Twist Rate (Full Line) and at a Constant Twist Rate to Twist Ratio (Broken Lines) /49/.

and since $(\dot{\theta}/\theta) = \text{constant} = (d\dot{\theta}/d\theta)$, this equation becomes

$$\left(\frac{\theta}{M}\right)\frac{dM}{d\theta} = \frac{\partial \ln M}{\partial \ln \theta}\Big|_{\dot{\theta}} + \frac{\partial \ln M}{\partial \ln \dot{\theta}}\Big|_{\theta} = n + m \qquad (17)$$

where n and m are the strain hardening exponent and the strain rate sensitivity index, respectively. Thus, for the special test, equation (15) turns into the following form, which is the famous formula of Fields and Backofen :

$$\zeta = \frac{M}{2\pi R^3}(3+n+m) \tag{18}$$

However, for engineering materials, the special tests are unnecessary for the reason outlined above, and equation (18) can be applied directly to the results obtained at constant $\dot{\theta}$.

At low temperatures, the m values are of the order of a few thousandths, and therefore can be overlooked in the calculations of shear stress. At high temperatures, on the other hand, n is negligible for the same reason. For intermediate temperatures, both n and m are significant and should be taken into consideration.

Fields and Backofen's formula can be extended to give the shear stress values for the hot-torsion of tubular specimens /50/. Assuming that

$$\zeta = K \dot{\gamma}^m \gamma^n \tag{19}$$

where

$$\gamma = \frac{r\,\theta}{L} \tag{20}$$

and

$$\dot{\gamma} = \frac{r\,\dot{\theta}}{L} \tag{21}$$

and replacing shear stress ζ in the moment integral, equation (5), by its value in equation (19), one obtains :

$$M = 2\pi \int_{R_i}^{R} \zeta r^2 dr = 2\pi \int_{R_i}^{R} r^2 K\left(\frac{r\dot{\theta}}{L}\right)^m \left(\frac{r\theta}{L}\right)^n dr \qquad (22)$$

where R_i is the internal radius of the tubular specimen. Integration of this equation gives :

$$M = \frac{2\pi}{3+m+n}\left[R^3\zeta - R_i^3\zeta_i\right] \qquad (23)$$

where ζ_i denotes the shear stress at the internal radius of the tube.

This equation is generally used /11/ in the following modified form :

$$\zeta = \frac{M(3+m+n)}{2\pi(R^3 - R_i^3)} \qquad (24)$$

Sample calculations show that /11/ the use of equation (24) results in errors of 1 to 3 percent in ζ . Hence, equation (24) is employed in data analysis rather than the more complicated exact expression (23).

In some investigations /16/, however, by considering strain and strain rate across the wall of a thin-walled tube to be constant, a simpler expression for converting torque to shear stress is employed. In this case, the shear stress ζ at any instant will be constant throughout the tube :

$$M = 2\pi\zeta \int_{R_i}^{R} r^2 dr \qquad (25)$$

This integration gives the shear stress as

$$\zeta = \frac{3\,M}{2\pi(R^3 - R_i^3)} \tag{26}$$

Then the corresponding shear strain and shear strain rate will be :

$$\gamma = \frac{R + R_i}{2\,L}\,\theta \tag{27}$$

$$\dot{\gamma} = \frac{R + R_i}{2\,L}\,\dot{\theta} \tag{28}$$

The disadvantage of tubular specimens is that they tend to buckle at relatively low strains and the main advantage of the torsion test is lost. The wall thickness of a tubular specimen should be so chosen as not to cause buckling. But it should be as small as possible at the same time, because in such a case only ζ can be considered as a constant value throughout the wall-thickness.

Because of its relative simplicity, Fields and Backofen method is widely used, particularly for carrying out rolling simulations. It suffers, however, from three limitations /49/ :

The first kind of limitation can be attributed to the hypothesis of history independence. That is, the shear stress ζ is not, in general, a unique function of γ and $\dot{\gamma}$. As shown in Figure 4, if at a given strain of γ_1, the strain rate is suddenly increased from $\dot{\gamma}_1$ to $\dot{\gamma}_2$, the resulting flow curve remains below the curve determined by testing at $\dot{\gamma}_2$ continously. Thus, two values of stress, ζ_2 and ζ_2 , are defined for the same conditions (γ_1 , $\dot{\gamma}_2$) and it is appearent that ζ is not

a unique function of γ and $\dot{\gamma}$. The inaccuracy induced by the hypothesis $\zeta = \zeta(\gamma,\dot{\gamma})$, however, is almost always within a few percent.

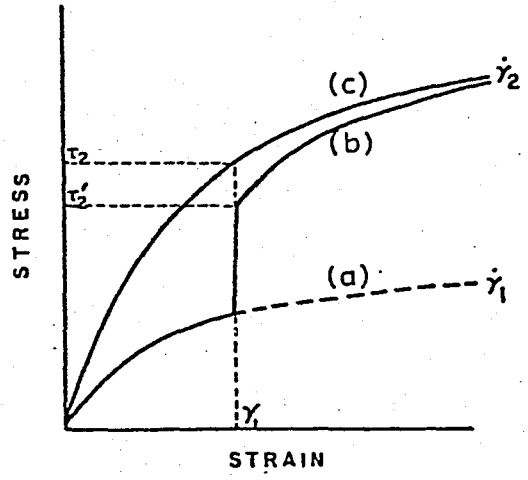

Figure 4 - Typical flow stress behaviour of a rate sensitive work hardening material. At a strain rate of $\dot{\gamma}_1$ and a strain of γ_1(curve (a)), the sample is submitted to a sharp increase in strain rate to $\dot{\gamma}_2$(curve (b)). The resulting flow stress ζ_2' is lower than the flow stress ζ_2 developed at γ_1 when straining is continuous at $\dot{\gamma}_2$(curve (c)). [49].

The second kind of inaccuracy is due to the formalism itself and is of considerable importance because its effect increases with the strain. In short, if equation (18) is directly applied to an experimental torque-twist curve which exhibits a normal amount of scatter, the stress-strain curve obtained will show an increasing scattering with strain (Figures 5 and 6). This is because of the increasing relative inaccuracy inherent in the Fields and Backofen formula. On the other hand, when an initially smoothed torque-twist curve is used, smooth stress-strain curves are, of course, obtained.

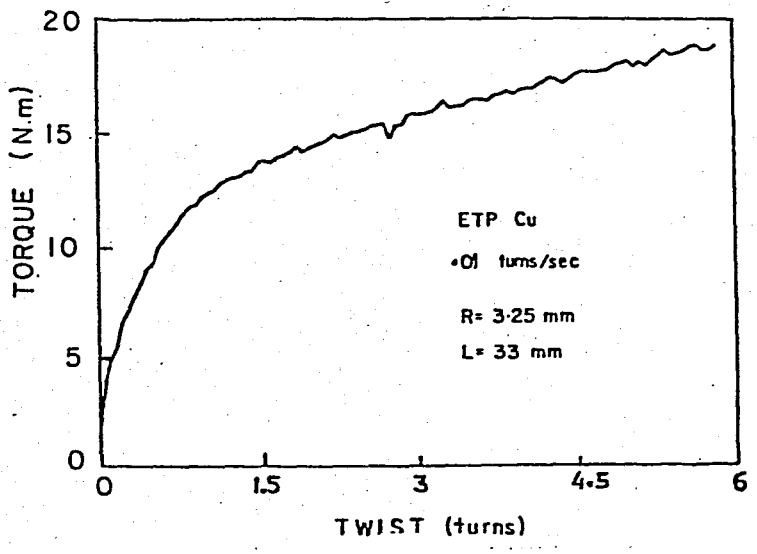

Figure 5 - Torque-twist curve obtained using a computerized torsion machine. Note the nearly constant experimental scatter due principally to noise in the measuring circuit /49/.

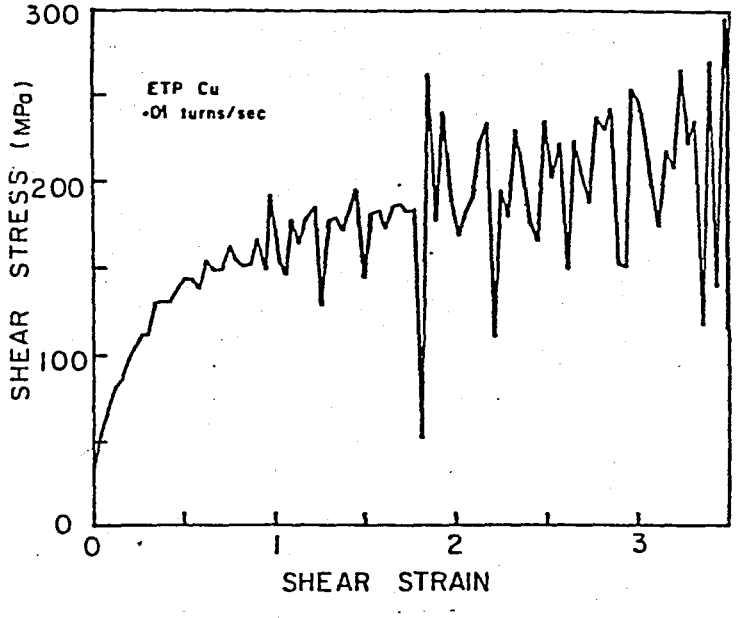

Figure 6 - Shear stress - shear strain relation calculated from the data of Figure 5 by the method of Fields and Backofen. The width of the scatter band increases with strain because of the increasing relative inaccuracy inherent in the Fields and Backofen formula /49/.

The third limitation inherent in this method is associated with the manner in which the slope of the $\ln M$ versus $\ln \theta$ curve is

determined. For a given value of M and $(\partial M/\partial \theta)|_{\dot{\theta}}$, the slope

$$\frac{\partial \ln M}{\partial \ln \theta}\Big|_{\dot{\theta}} = \frac{\theta}{M}\left(\frac{\partial M}{\partial \theta}\right)\Big|_{\dot{\theta}} \qquad (29)$$

is strogly influenced by the value of θ, which may not be available if the prior loading history is not known.

3.3 DIFFERENTIAL METHOD

This technique requires two tests to be carried out at the same twist rate with samples of radii R_1 and R_2 close to each other. The difference between twist moments, $M_2 - M_1$, required to twist the two samples at a constant θ can be considered as the torque required to twist a tube whose thickness is the same as the difference in radii of the two samples /49,51/.

By assuming that the shear stress is nearly constant and equal to $\bar{\zeta}$ in the thin layer (R_1, R_2), the torque difference at a given twist will be given as

$$M_2 - M_1 = 2\pi \int_{R_1}^{R_2} \zeta r^2 dr = 2\pi \bar{\zeta} \frac{R_2^3 - R_1^3}{3} \qquad (30)$$

Therefore the shear stress value will be

$$\bar{\zeta} = \frac{3(M_2 - M_1)}{2\pi(R_2^3 - R_1^3)} \qquad (31)$$

and corresponding shear strain and shear strain rate values will be

$$\bar{\gamma} = \frac{R_1 + R_2}{2L}\theta \quad ; \quad \dot{\bar{\gamma}} = \frac{R_1 + R_2}{2L}\dot{\theta} \tag{32}$$

In this technique, the advantage of using thin-walled tubular samples is combined with that of using solid samples.

The inaccuracy inherent in the calculation of $\bar{\bar{\tau}}$ from equation (31) is high if the difference between twist moments $M_2 - M_1$ is small, that is, at small strains or when the radius difference is small.

When applying differential method, care should be taken in machining the specimens to the required tolerances. Furthermore, a good reproducibility should be obtained since scatter in torque measurements is magnified in determination of shear stress.

The number of specimens used in this method is twice the number of those used in the method of Fields and Backofen.

3.4 SURFACE SHEAR STRESS METHOD

This method is based on the assumption that the shear stress at a radius r is affected only by the history of this particular location, and not by the developments at neighboring locations, nor in the extreme by the history of the outermost layer of the material. Namely,

$$\tau = \tau(r) \neq \tau(r,R) \tag{33}$$

Other assumptions in this analysis are /49/ :

i) radii remain straight during testing;

ii) no length changes take place;

iii) no flow localization occurs.

Under these conditions, the derivative of the moment integral, equation (5), with respect to the radius R, at a given twist, twist rate and radius r can be written as :

$$S(\theta,\dot{\theta}) = \frac{\partial M}{\partial R}\Big|_{\theta,\dot{\theta}} = 2\pi \zeta_r r^2 \qquad (34)$$

Here r is the radius value at which the slope of the torque-radius curve is calculated for a given θ and $\dot{\theta}$. It is evident from equation (34) that the precise value of the current shear stress at r can be determined from the knowledge of the slop $S(\theta,\dot{\theta})$ of the torque-radius curve at this radius.

The values of the corresponding strain and strain rate are :

$$\gamma = \frac{r\theta}{L} \quad , \quad \dot{\gamma} = \frac{r\dot{\theta}}{L} \qquad (35)$$

The experimental procedure is the following:
Experiments are carried out on specimens of increasing radii. From the set of torque-twist curves obtained, the torque-radius relation is determined for each twist value of interest (Figure 7).

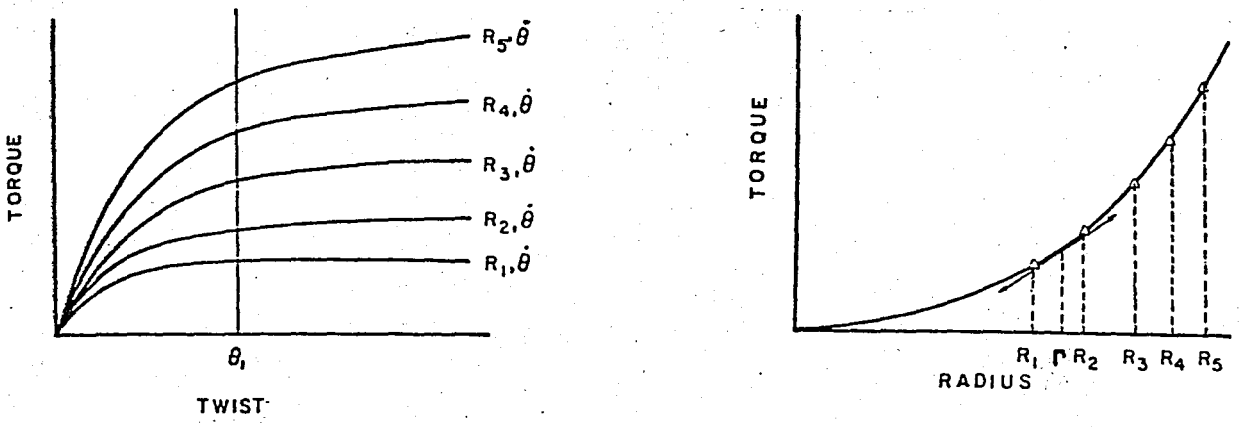

(a) (b)

Figure 7 - Method of calculation of the slope $(\partial M/\partial R)|_{\theta,\dot{\theta}}$.
(a) At a given twist θ_1, a set of torque-radius data is abstracted from the results determined on samples of increasing radii.
(b) A smooth curve is fitted to the torque-radius data of Figure 7-(a), from which the slope $(\partial M/\partial R)|_{\theta,\dot{\theta}}$ is calculated.

Each of these curves is then fitted by means of a log M versus R polynomial. The degree of the polynomial has a marked effect on the local slope. The slope $S(\theta,\dot{\theta})$ is then calculated by taking the derivative of this polynomial at a certain R value. Substituting this into the equation (34), one obtains the shear stress value for this strain and strain rate.

The accuracy of this method is directly linked to the accuracy with which the slope can be determined. In other words, it depends on the number of specimens of different radii. The use of only two specimens for a given strain rate and temperature leads to the least accuracy. In such a case, equation (34) will be modified to :

$$\frac{M_2 - M_1}{R_2 - R_1} = 2\pi \zeta_r r^2 \qquad (36)$$

The surface shear stress method shows accordance with the method of Fields and Backofen at low strains and with the differential method at large strains.

IV. EVALUATION OF TORQUE-TWIST DATA

The torque-twist data recorded during a hot torsion test is not useful from engineering point of view. Therefore, it requires a conversion to stress-strain values. The method which is most widely employed for this purpose is that of Fields and Backofen. However, a direct conversion of torque-twist data to shear stress-shear strain values by the use of this method, or any of others mentioned in the last chapter, may, in some cases, lead to serious errors. This is mainly because the length of the deformation zone is generally greater than the predetermined gage length, and for such reasons as machining marks, oxidation, etc. the stress and strain at the specimen surface are highly distorted.

To avoid from the effects of these sources of uncertainty, some modifications are made in data evaluation. An explanation of these modifications is given below together with the yield criteria used if true stress-true strain values are required rather than shear stress-shear strain values.

4.1 CRITICAL RADIUS CONCEPT

The conventional method of determining flow curves from torsion

test data consists of calculating shear stress from the following equation of Fields and Backofen :

$$\tau = \frac{M}{2\pi R^3}\left(3 + \frac{\dot{\theta}}{M}\left(\frac{\partial M}{\partial \theta}\Big|_{\dot{\theta}}\right) + \frac{\dot{\theta}}{M}\left(\frac{\partial M}{\partial \dot{\theta}}\Big|_{\theta}\right)\right) \qquad (37)$$

and shear strain from the formula below :

$$\gamma = \frac{R\,\theta}{L} \qquad (38)$$

The calculation of stress and strain for the surface of the specimen is mathematically correct. However, stress and strain are strongly distorted at the surface because of machining marks, oxidation, etc., and also because of the notch effect. Additionally, the shear stress is calculated from equation (37) is very much affected by experimental errors which propagate through the partial derivatives of torque. An improved solution should not contain derivatives of measured curves.

Therefore, it is recommended /42,50,52-54/ to calculate stress and strain at a radial distance smaller than the specimen radius, i.e. for a position inside the specimen. This is only possible by renouncing a rigorous mathematical determination of stress. So, an "error of approximation" is put up with the new procedure of determining a physically senseful solution.

It is mentioned that at a given torque and at a certain radius inside the specimen, shear stress has a value which is equal for different courses of flow curve. This radius value is called

"critical radius". Among a number of different definitions of critical radius, the most useful one is the following :

$$\frac{\partial \zeta(r,p,T)}{\partial p} = 0 \quad \text{for} \quad r = r^{*} \tag{39}$$

where r^{*} is the critical radius, T is temperature and p is a parameter defined as the sum of strain hardening exponent (n) and, strain rate sensitivity index (m) :

$$p = n + m \tag{40}$$

To take the partial derivative in equation (39), it is assumed that shear stress ζ at any radius r is related to the shear strain γ and shear strain rate $\dot{\gamma}$ at that radius by the following equation :

$$\zeta = K \dot{\gamma}^{m} \gamma^{n} \tag{41}$$

where K is a constant.

After the substitution of equation (41) into the torque integral, and carrying out the integration one obtains the following relationship for shear stress at any radius r :

$$\zeta = \frac{M}{2\pi R^{3}}(3+m+n)\left(\frac{r}{R}\right)^{m+n} \tag{42}$$

Using equation (40) and taking the partial derivative of ζ with respect to p, as mentioned in equation (39), critical radius is

found as :

$$r^{*} = R\, e^{-\frac{1}{3+p}} \tag{43}$$

It can be shown that the critical radius obtained from equation (39) depends only very weakly on p.

If equation (42) is written in the following form :

$$\zeta = \frac{M}{2\pi R^3}(3+p)\left(\frac{r}{R}\right)^{p} \tag{44}$$

and is plotted for different values of p (Figure 8), the curves obtained for shear stress versus radial distance intersect almost at one point. Therefore, the critical radius can practically always be approximated by :

$$r^{*} = \frac{3}{4} R \tag{45}$$

For this value, the shear stress will be given with an accuracy better than one percent by the equation :

$$\zeta(r^{*},T) = \zeta^{*}(T) \qquad \frac{3M}{2\pi R^3} \tag{46}$$

and, the shear strain will be :

$$\gamma(r^{*}) = \gamma^{*} = \frac{3}{4}\,\gamma_{R} \tag{47}$$

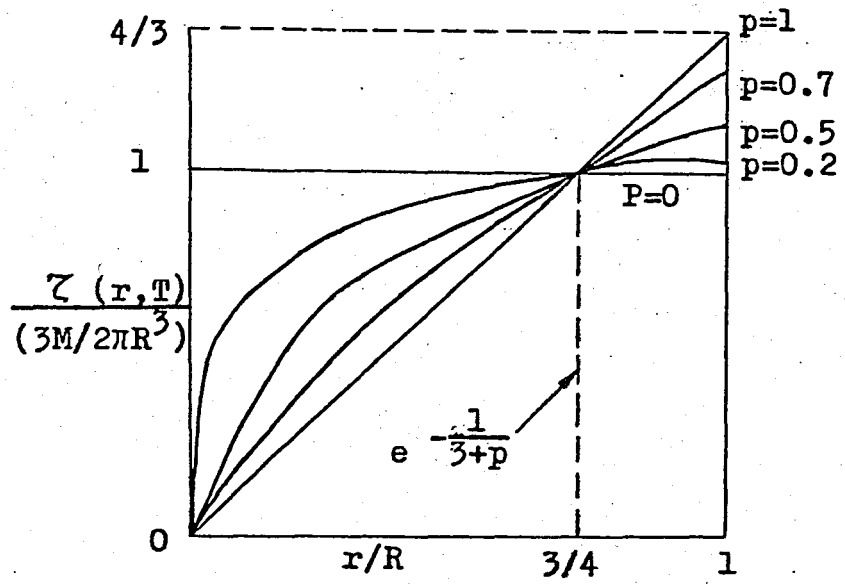

Figure 8 - Shear stress in an imaginary solid specimen without a notch as a function of radial distance at a given torque /42/.

The concept of "critical radius" can be extended for tubular specimens /42/ by using equation (39) and by following the same procedure as in the derivations of equation (42) and equation (43). Therefore, the relationship below is obtained for a specimen with inside radius R_i and outside radius R :

$$\frac{r^*}{R} = \frac{(R_i/R)^{1/[1-(R/R_i)^{3+p}]}}{e^{1/(3+p)}} \qquad (48)$$

The critical radius given by equation (48) depends very weakly on the value of p. For practical purposes the critical radius can be approximated with the following expression :

$$\frac{r^*}{R} \approx 0.91 \quad \text{for} \quad (R_i/R) = 0.8 \text{ and } 0.1 \leq p \leq 0.5 \qquad (49)$$

In this case, the accuracy is better than one percent.

The shear strain at $r=r^*$, on the other hand, will be :

$$\gamma^* \approx 0.91 \ \gamma_R \tag{50}$$

and the shear stress calculated from the torque integral with $m+n=0$ will be

$$\zeta = \frac{3M}{2\pi(R^3 - R_i^3)} \tag{51}$$

The use of a "critical radius" in calculation of flow curves minimizes the problems associated with the structural gradient across the diameter of the specimen. Since the relationship between surface shear stress and torque derived by Fields and Backofen is in the following form,

$$\zeta = \frac{M}{2\pi R^3}(3+m+n) \tag{52}$$

and this suffers from the disadvantage that m and n must be known for the shear stress to be determined accurately from the measured torque. Furthermore, as n varies with strain and m varies with strain rate, conversion is tedious even if the values are known. Therefore, it is advantageous to calculate the deformation parameters at the critical radius rather than at the specimen surface, because of the insensitivity of this radius to the value of $m+n$ and hence the structural gradient within the specimen.

For the method of determining strain and stress at critical radius, calculation of the so-called notch factor is not necessary. That is, notch effect can almost be neglected at this radius, while notch has the strongest effect at the specimen surface. Even if there is a strong notch effect caused by the shape of short specimens, stress and strain at the critical radius will not be affected by it.

Calculation of stress and strain for a critical radius inside the specimen seems to cause a loss of information since the flow curve obtained in this way is defined for a smaller range of strain than that one obtained from stress and strain at the surface. However, this appearent "loss of information" is accepted in favour of an improved accuracy of results. The same holds for the range of strain rate for which the flow curve is determined.

4.2 EFFECTIVE LENGTH CONCEPT

The maximum strain rate which can be obtained by using conventional test pieces (the length of which is large compared with the diameter) on a usual torsion testing machine is one order of magnitude lower than those obtained in metal forming processes. To obtain higher strain rates is torsion test two ways can be followed :

1. Using a faster testing apparatus
2. Using specimens with a high ratio of R/L

Here R is the radius and L is the gage length of the specimen. Since the strain rate is defined as :

$$\dot{\gamma}_R = \frac{R\,\dot{\theta}}{L} \tag{53}$$

first method is concerned with increasing $\dot{\gamma}_R$ by increasing $\dot{\theta}$, while the second one is concerned with doing the same thing by increasing R/L ratio. In this case, changing specimen dimensions seems to be the more economic solution of this problem.

The specimens used consist of a cylindrical section of length L, square or cylindrical heads and rounded transitions between heads and cylindrical section. The rounded zones are called "transition zones" and are characterized by notch radius R_N.

For a given specimen radius R and a notch radius R_N, a variation of strain rate is obtained by geometrical means, i.e. by varying the length L of the cylindrical section, including L=0 (Figure 9).

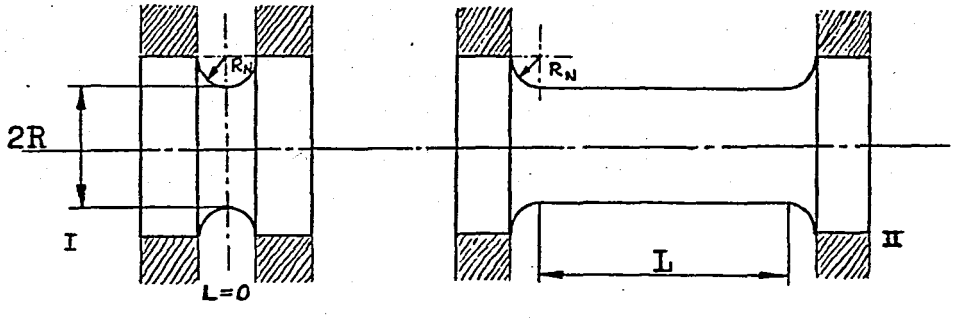

Figure 9 - Short and long specimens.

Although very high strain rates can be achieved with extremely short specimens, the concept of specimen length, in this case, must be rigorously investigated than for long specimens. This necessity originates from the penetration of deformation into the transition zones.

To determine the length participating in plastic deformation of short specimens, "effective length (L_E)" is defined. This quantity is applicable to specimens of any length, including $L=0$, and gives the correct value of strain when inserted into the following equation:

$$\gamma_R = \frac{R\,\theta}{L_E} \tag{54}$$

The relation between the effective lengths of specimens of types I and II in Figure 9 is given by the following equations :

$$L_{EI} = 2\,R_E \quad \text{and} \quad L_{EII} = L + 2\,R_E \tag{55}$$

where R_E is the contribution of a transition zone to deformation. Equation (55) holds under the assumption that notch effect can be neglected. This assumption cannot cause an essential error if stress and strain are calculated for the critical radius where the notch correction is negligible.

Assuming the relationship,

$$\tau = K\,\dot{\gamma}^m\,\gamma^n \tag{56}$$

for shear stress, the following equation is derived for the calculation of R_E :

$$R_E = \int_0^{R_N} \left[\frac{R}{R(x)}\right]^{(3+p)/p} dx \tag{57}$$

where R(x) is the function of variation of radius along the axis of the specimen with R(0)= R.

Equation (57) holds under the assumptions that the material is homogeneous, incompressible, and isotropic. From this equation, it follows that the effective length does not depend only on specimen geometry, but also on the material through the parameter p.

For tubular specimens, the R_E value can be calculated from the following relationship /42/

$$R_E = \int_0^{R_N} \left[\frac{R^{3+p} - R_i^{3+p}}{[R(x)]^{3+p} - R_i^{3+p}} \right]^{1/p} dx \qquad (58)$$

where R_i is the internal radius of tubular specimen. The special case of solid specimens iscontained in this equation, since by inserting $R_i = 0$, equation (57) is obtained.

4.3 YIELD CRITERIA

The shear stress-shear strain values obtained from torque-twist curves are either used directly or they are converted to true stress-true strain values by using a yield criterion. For this purpose, either Tresca or von Mises criterion is employed.

The values of true stress, true strain and true strain rate according to Tresca criterion will be :

$$\sigma = 2\zeta \quad , \quad \varepsilon = \gamma/2 \quad , \quad \dot{\varepsilon} = \dot{\gamma}/2 \qquad (59)$$

and according to von Mises criterion they will be :

$$\sigma = \sqrt{3}\,\zeta \;,\; \varepsilon = \gamma/\sqrt{3} \quad , \quad \dot{\varepsilon} = \dot{\gamma}/\sqrt{3} \tag{60}$$

There exists a difference of 15 percent between these two criteria. This causes a large difference of the absolute height of flow stress, while the relative shape of flow curve and strain-rate-sensitivity are not strongly affected.

Furthermore, both criteria are based on the common assumption that stress is independent of strain rate. Since hot-torsion tests are often carried out on strain-rate-sensitive materials applying either the von Mises or the Tresca criterion implies a fundamental contradiction. Until now, however, no yield criterion seems to be known which takes into account strain-rate-sensitivity of materials and which still is simple enough for practical applications.

It should be mentioned that the largest uncertainty in the evaluation of hot-torsion test results is caused by the yield criterion used.

V. EXPERIMENTAL WORK

Hot-torsion tests were performed on specimens made of aluminum 1100 and aluminum 2024 materials. In order to reveal the effects of temperature and strain rate, tests were carried out at three different temperatures and four different rates of deformation.

Using the techniques of optical microscopy, both materials were examined metallographically in both initial and deformed conditions. This examination was mainly directed to study the microstructure-property relationships and to search the existence of a critical-radius-zone on the microstructure of a deformed specimen.

5.1 PRELIMINARY WORK

5.1.1 Materials

The high-temperature deformation characteristics of two materials, aluminum of commercial purity (Aluminum 1100), and aluminum alloy 2024, were studied through a series of hot torsion tests. Both materials were supplied from FENIŞ. The chemical analysis of aluminum alloy 2024 revealed the existence of the following elements within the structure: 3.82 pct. Cu, 1.01 pct. Si, 0.98 pct. Mn, 0.93 pct. Zn, 0.90 pct. Mg, 0.86 pct. Fe, and 0.012 pct. Cr.

Both materials were in ingot form initially. Billets of cylindrical shape were cut from these ingots and extruded (Figure 10) into the form of rods with 25 mm. diameter under the conditions given in Table I. The specimens used were machined from these rods. No heat treatment process were applied prior to machining, because any improved material property, which would be gained from the processes, might disappear at testing temperatures.

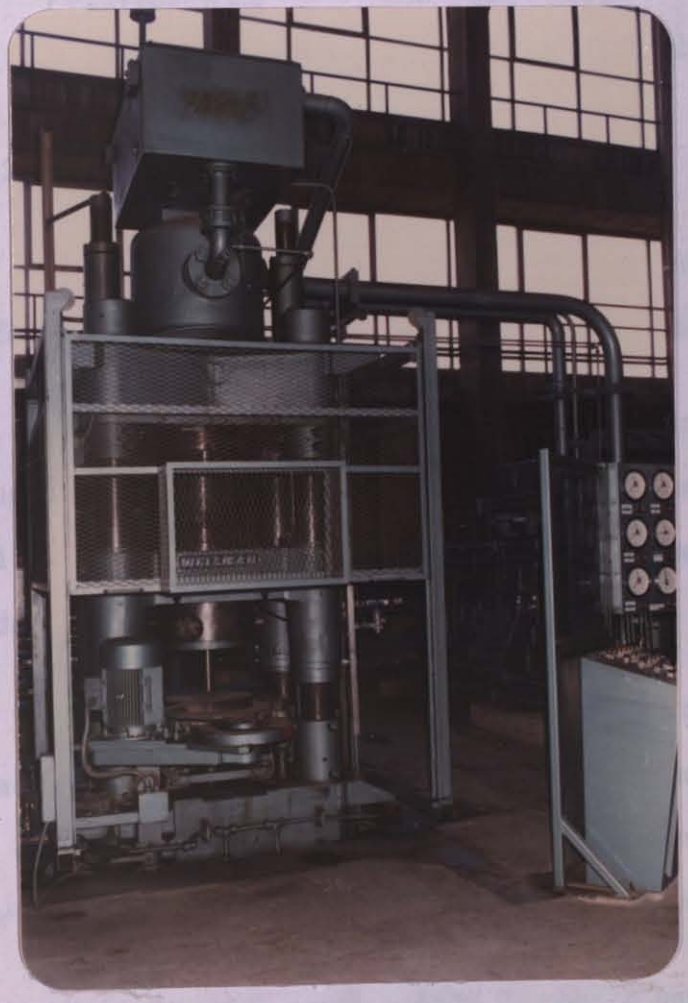

Figure 10 - Extrusion press with 500-ton capacity.

TABLE I - Extrusion Conditions

	Aluminum 1100	Aluminum 2024
Billet Temperature	400°C	400°C
Container Temperature	350°C	350°C
Ram Speed	5 mm/s	5 mm/s
Container Diameter	80 mm	80 mm
Die Diameter	25 mm	25 mm
Extrusion Ratio	10.24	10.24
Cooling Type	Air-cooled	Water-quenched

5.1.2 Specimen Design

The optimum specimen shape is determined by a number of different requirements, some of which are in contradiction.

On one hand, a specimen should be as short as possible, because in this case very high strain rates can be reached. Additionally, the heat generated during deformation is easily conducted off through the specimen heads.

On the other hand, the specimen should be as long as possible because in this case the notch effect can be neglected. In addition, the effective lengths cannot be determined accurately for extremely short specimens, as proved by experimental results.

Moreover, the notch radius R_N should not be too small, since otherwise notch effect will become so strong as to initiate fracture at rather low strains.

With all these aspects in view, the optimum specimen geometry is roughly given in literature /42.50/ by the following two conditions :

$$\frac{1}{2} \leq R/L \leq 2 \quad \text{and} \quad \frac{1}{4} \leq \frac{R_N}{R} \leq 1 \tag{61}$$

The main dimensions, i.e. L, R and R_N, of hot-torsion test specimen used in this investigation was determined in accordance with these optimum specimen geometry conditions. The sample was short enough to give surface shear strain rates higher than those conventional torsion-test samples reach. But it was also long enough not to cause any uncertainty originated from notch effect or from the determination of effective length. This specimen, for which R_N/R ratio and R/L ratio was chosen 7/15 (3.5 mm/7.5 mm) and 1/2 (7.5 mm/15 mm), respectively is shown in Figure 11.

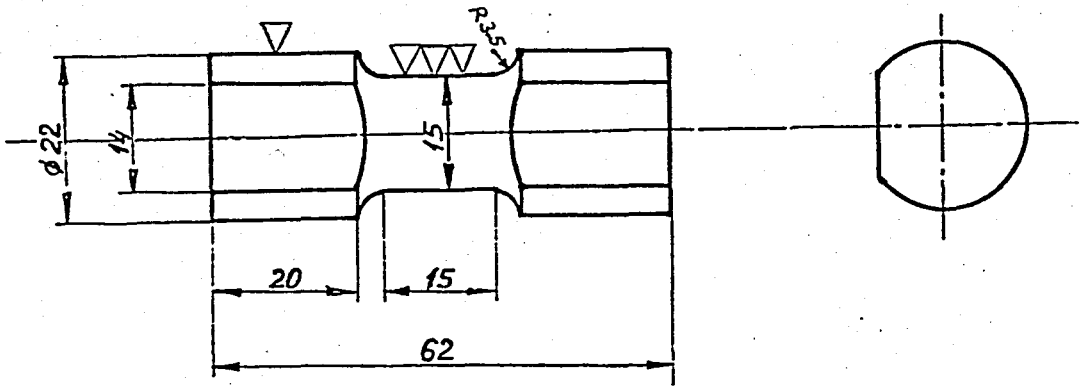

Figure 11 - Hot-torsion Test Specimen (Dimensions are in mm.)

5.1.3 Specimen Joining System Design

In order to place the specimen and the high-temperature furnace between the chucks of testing machine (Figure 12) two extension rods (Figure 13) were used. These rods were made of 15 CrNiSi, a material durable to high temperatures.

During experiments, the furnace was hung on the grooves of upper extension rod and hot-torsion test specimen (Figure 11) was joined, in vertical position, to torsion load cell at the upper end and to lower torsion fixture at the lower end through the extension rods and chucks.

The ends of extension rods where specimen is placed were so designed as to prevent the specimen from any rotation relative to the rods during tests. The flat parts of specimen heads were pressed by two bolts on each end through steel keys.

The main difficulty encountered was the elimination of the eccentricity between the axes of specimen, rods and testing machine. Specimens were joined to extension rods on a lathe and eccentricity was controlled closely by means of a comparator. In most of the tests, eccentricity could not be completely eliminated, but it was always lowered up to a level of 0.02 mm.

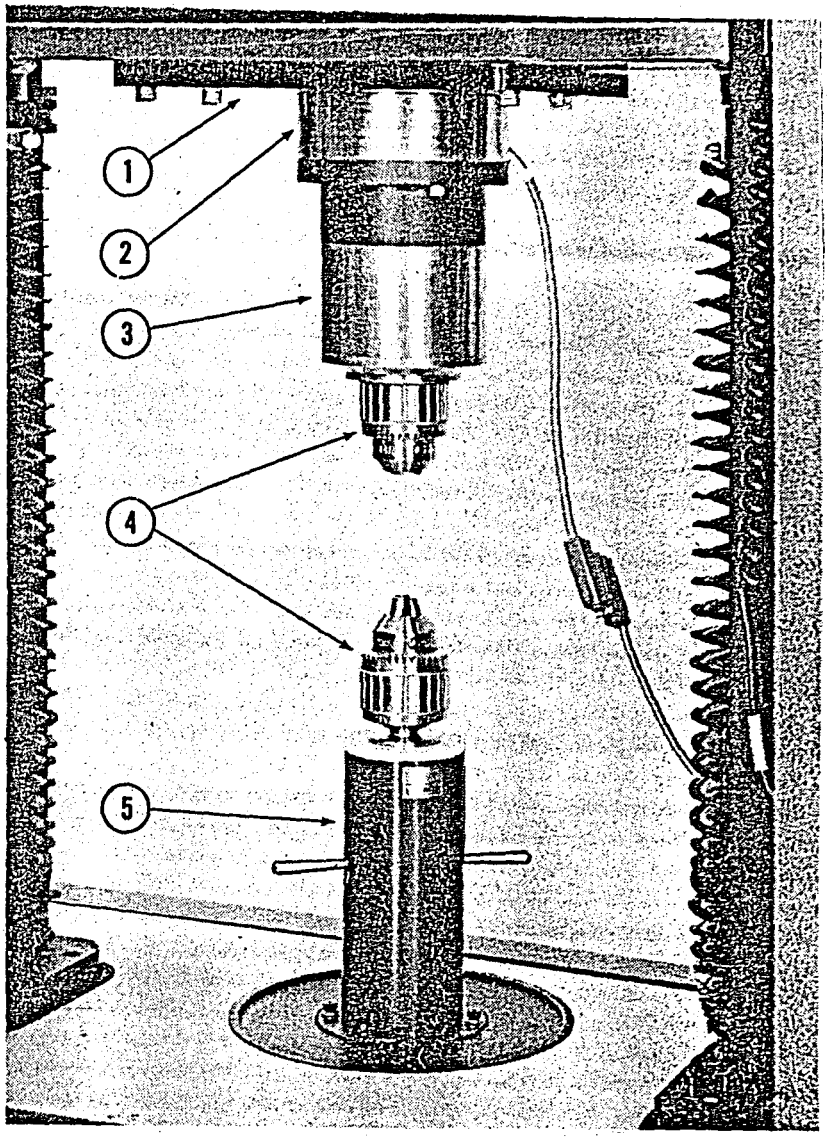

Figure 12 - Torsion Test Accessory. (1) Adapter Plate; (2) Torsion Cell Spacer; (3) Torsion Load Cell; (4) Specimen Chucks; (5) Lower Torsion Fixture.

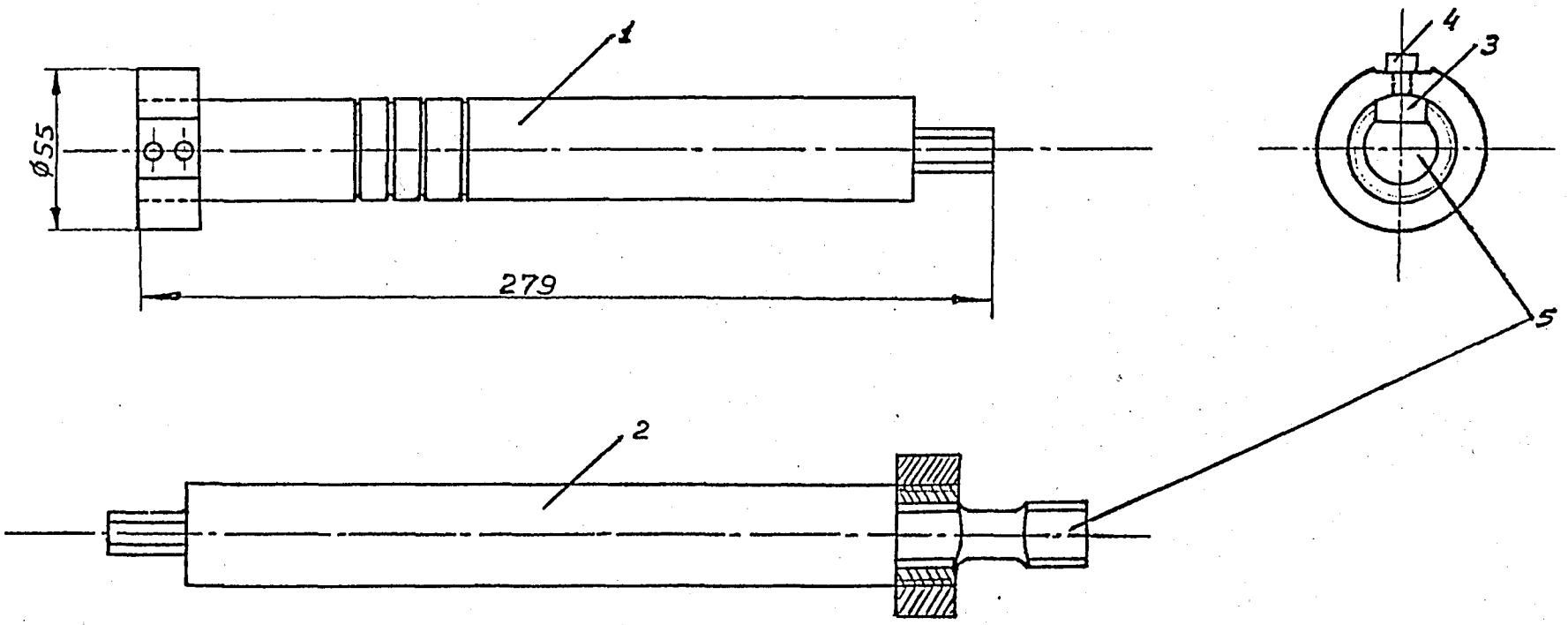

Figure 13 - Extension rods and specimen joining system. (1) Upper Extension Rod; (2) Lower Extension Rod; (3) Key; (4) Bolt; (5) Specimen.

5.1.4 Testing Machine Preparation

Hot-torsion tests were carried out by using an Instron TT-1115 universal testing machine (Figure 14).

Figure 14 - Instron TT-1115 Universal Testing Machine with Torsion Test Accessory and High Temperature Furnace.

The following scenario of preparation was repeated every time prior to testing:

a) Controlling the axes of load cell and lower torsion fixture chucks for eccentricity by the use of a comparator;

b) Positioning the lower torsion fixture chuck, which is movable in axial direction, at a place where it can compensate the upward or downward displacement of crosshead and the length change of specimen during testing, thus preventing the test from gaining a tension-torsion or a compression-torsion character.

c) Zeroing, balancing and calibrating the load weighing

system electronically;

d) Placing the pen at a desired position on chart and setting the chart movement direction of recorder;

e) Inserting the free ends of extension rods into the chucks and tightening;

f) Eliminating any pre-load, which may come during tightening, with very small rotations of the lower torsion fixture;

g) Setting the mechanical restriction switch in accordance with the maximum allowable crosshead displacement;

h) Setting the chart speed in accordance with the testing speed of specimen;

i) Hanging the high-temperature furnace on the upper extension rod and making the thermocouple connections;

j) Setting the testing temperature, the speed of rotation, and the full scale load of chart;

k) Switching the heating system on.

5.2 HOT-TORSION EXPERIMENTS

Hot torsion experiments were performed on aluminum 1100 specimens at temperatures of 250^{o}C, 350^{o}C and 450^{o}C, and on aluminum 2024 specimens at temperatures of 250^{o}C ,300^{o}C and 350^{o}C. For both materials, the speeds of rotation was chosen as follows: 21.32 rpm, 5.33 rpm, 1.066 rpm, and 0.2132 rpm.

During testing, the applied torque was recorded as a function of twist angle and the records were, then, used in determination of material flow curves.

5.2.1 Heating and Temperature Control

In order to heat the specimens up to testing temperatures and holding at these temperatures during the test, a cylindrical furnace of 500-watt capacity was used (Figures 14 and 15). This furnace was hung on the grooves of the upper extension rod.

While heating the specimen to testing temperature and holding there for the achievement of a steady state regime, temperature was controlled by means of a thermocouple touching the surface of the specimen. Just before testing began, this thermocouple was pulled back and - by means of another thermocouple placed in furnace wall - furnace temperature was kept constant at the value corresponding to the testing temperature of the specimen. The reasons of this change were:

i) the danger of fracture that specimen-thermocouple faced during the deformation of test piece;

ii) the failing temperature-control caused by the separation of thermocouple from specimen surface.

In the evaluation of torsion test data it was assumed that isothermal conditions were achieved during testing. This is because the strain rates applied are not very high, and the specimen used is short enough to conduct off all the heat generated during deformation through its heads..

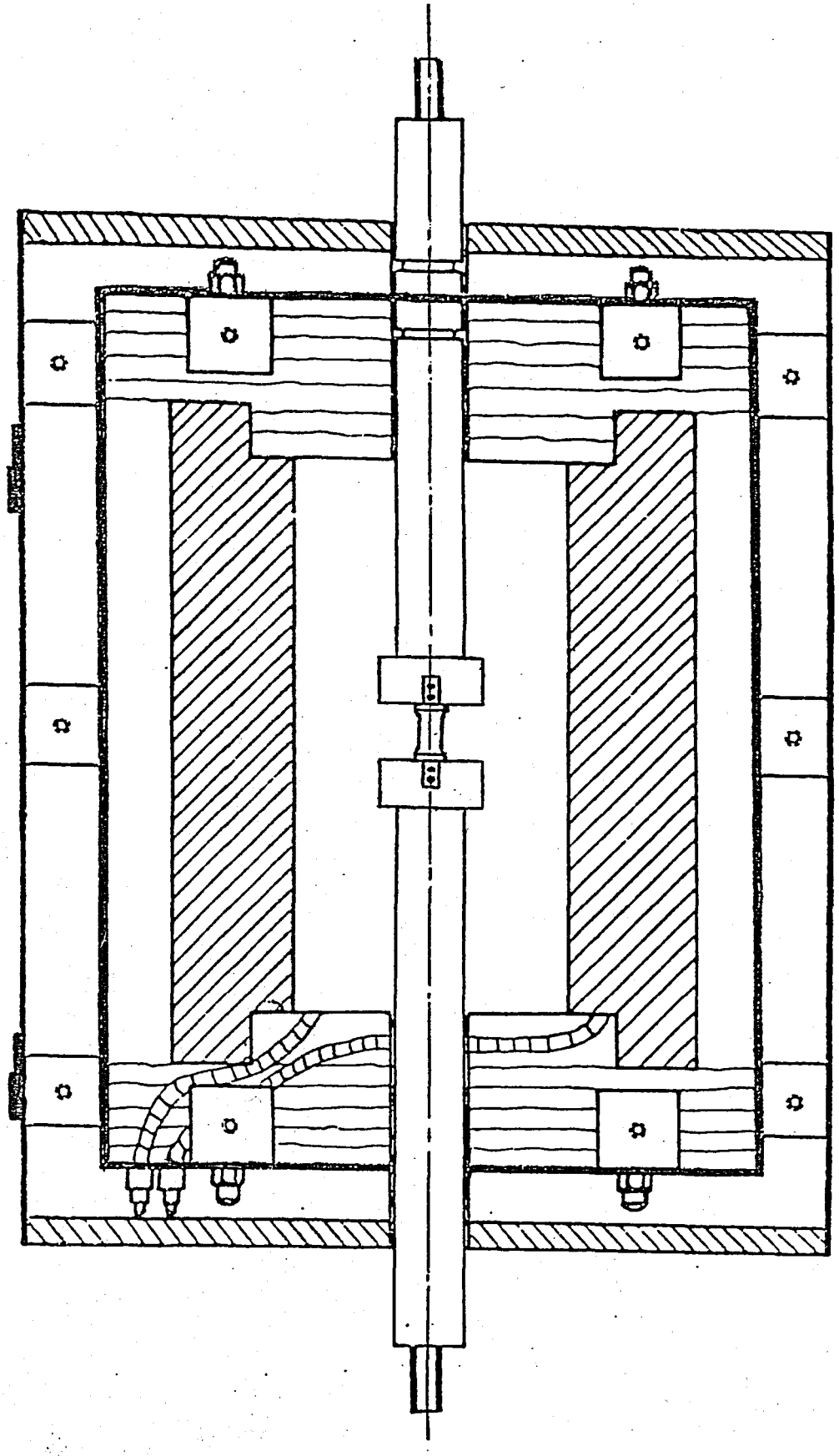

Figure 15 - High-temperature Furnace.

5.2.2 Torque-Twist Angle Data Recording

During testing, moment is applied by the rotation of lower torsion fixture and measured by a torsion load cell of 2000 kg.cm capacity. The signal from load cell is sent to an X-Y recorder. While the moment values are recorded along the Y-axis of the recorder, the corresponding twist angle values are recorded along the X-axis. Knowing the moment corresponding to full scale of the chart, the moment at any point can be directly read from these records. For twist angle values, on the other hand, a simple conversion is necessary and this is made easily after determination of how much angular displacement corresponds to a unit displacement on the chart.

For a successful recording, full scale moment value and chart speed should be determined conveniently prior to testing. In this study, full scale moment values were chosen in the light of previous experiments performed before the current one. Chart speeds, on the other hand, were selected such that they were neither so high as to cause the use of too much graph paper nor so low as to hide any important detail of torque-twist curve.

5.3 METALLOGRAPHIC EXAMINATION

By the use of polishing and optical microscopy techniques, a metallographic examination was carried out on specimens deformed at high temperatures and, then, cooled in air. The initial microstructures of materials were also included in this investigation for comparison purposes.

Disc-shaped parts were sectioned from the middle of deformed specimens. For aluminum 2024 specimens, this zone was the fracture zone, while for aluminum 1100 specimens it was the zone where deformation had reached maximum level.

In order to make handling easy and to facilitate placement on the microscope stage, the disc-shaped samples were mounted in bakelite cases under the effect of temperature and pressure. For this purpose, a specimen mount press was used.

On a belt surfacer, the surfaces of mounted specimens were grinded until they became flat. Extreme care was exercised during this operation in order to prevent the surfaces from damaging through overheating.

Polishing of specimens were carried out mechanically, on emery papers of increasing fineness, on polishing cloth, and on diamond paste. In order to examine the quality of polished surfaces under microscope, the samples were cleaned with detergent-added water, with alcohol, and finally dried in a stream of hot air.

After obtaining surfaces of desired quality, an etching operation was performed. Chemical etching, and electrolytic etching (Figure 16) were applied for aluminum 2024 and aluminum 1100 specimens respectively. Details related to etching reagents and etching methods of these two materials are given in Table II.

The microstructures of etched specimens were observed with a Reichert Metapan table microscope (Figure 17) and microphotographs were taken with different magnification ratios.

Figure 16 - Electrolytic Etching Apparatus.

TABLE II - Etchants used in microscopic examination of aluminum-base materials.

Material	Etchant	Composition	Application Procedure
Aluminum 2024	Keller's Reagent	2 ml HF (48 %), 3 ml HCl (conc.), 5 ml HNO_3 (conc.), 190 ml Water	- Immerse for 8 to 15 sec., - Wash in stream of warm water, - Blow dry. (Do not remove etching products from surface.)
Aluminum 1100	Barker's Reagent	4 to 5 ml HBF_4 (48 %), 200 ml water	Electrolytic: - Use Al, Pb or stainless steel for cathode, specimen is anode. - Anodize 40 to 80 sec. at about 0.2 amp. per sq.cm. (about 20 V dc). (Check results on microscope with crossed polarizers.)

Figure 17 - Reichert Metapan Table Microscope.

VI. RESULTS

6.1 MATERIAL FLOW CURVES

During hot torsion tests torque was recorded as a function of chart movement, and then, torque-chart movement curves were smoothed carefully (Figure 18) to obtain smooth flow curves after a series of calculations.

The torque value at any point was directly read from these records, while a conversion was needed for the determination of corresponding twist angle value. Knowing the speeds of rotation and chart movement, a simple conversion was applied for determining how much angular displacement corresponds to a unit displacement on the chart. Hence, torque-twist angle data were obtained for each testing condition (Appendix A).

In order to evaluate the torque-twist angle data so obtained the following relationships were used and calculations were carried out for critical radius :

Shear stress at critical radius :

$$\zeta^{*} = \frac{3\,M}{2\,\pi\,R^{3}} \tag{62}$$

Shear strain at critical radius :

$$\gamma^{*} = \frac{3}{4} \frac{R\theta}{L_E} \tag{63}$$

Shear strain rate at critical radius :

$$\gamma^{*} = \frac{3}{4} \frac{R\dot{\theta}}{L_E} \tag{64}$$

Here,

M = Twist moment applied,

θ = Twist angle,

$\dot{\theta}$ = Rate of change of twist angle,

R = Specimen radius,

L_E = Effective length.

Using equation (62), twist moment values were directly converted to shear stress values at critical radius. For the conversion of twist angle and rate of change of twist angle values to shear strain and shear strain rate values at critical radius, on the other hand, determination of effective lengths was needed for each material and for each testing temperature.

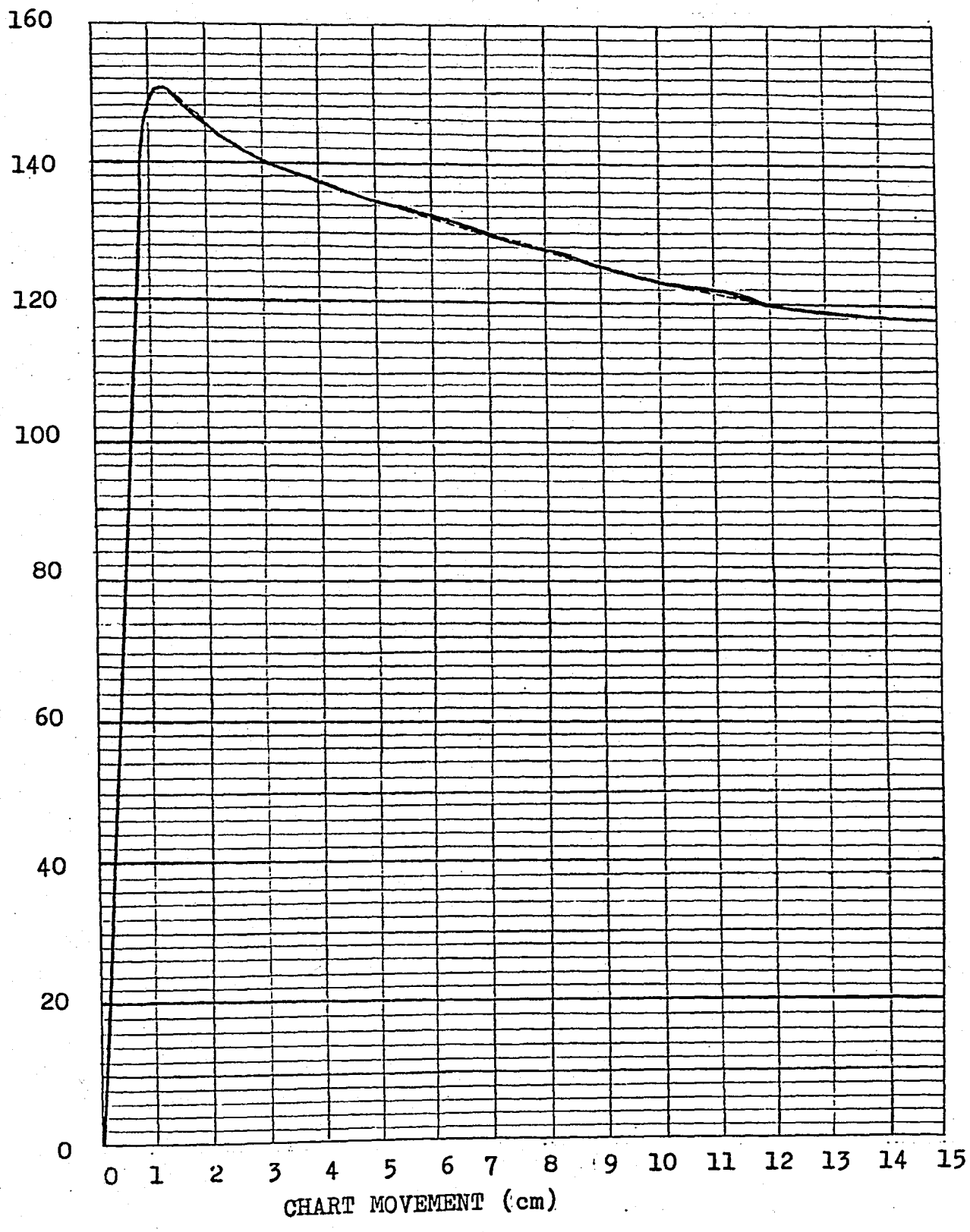

Figure 18 - Torque vs. chart movement curve of aluminum 1100 before and after smoothing, $T = 350^{o}C$, $\dot{\theta} = 2.233$ rad/s. (Broken lines indicate smoothing process).

Effective length of a specimen, i.e. the length of the zone participating in deformation, at a certain temperature was calculated from the following relationship,

$$L_E = L + 2 \int_0^{R_N} \left[\frac{R}{R(x)}\right]^{(3+p)/p} dx \qquad (65)$$

where L is the gage length and R is the radius of specimen, R_N is the notch radius, p is a material parameter and R(x) is the function of variation of radius along the axis of specimen with $R(0) = R$.

To carry out this calculation, the procedure below is followed:

1) Determination of p values :

The material parameter p is given by

$$p = n + m \qquad (66)$$

where n is the strain hardening exponent and m is the strain rate sensitivity index. Therefore, p values are found only through the calculation of n and m parameters. Keeping this fact in view, n values were calculated as the slopes of ln M versus ln θ diagrams at constant strain rate. m values, on the other hand, were obtained as the slopes of ln M versus ln $\dot{\theta}$ diagrams at constant strain. Because n values were found nearly one order of magnitude smaller than m values at the same temperature, the following approximation was made :

$$p = m \qquad (67)$$

To obtain a unique m at each temperature, the method of least squares was employed for m values corresponding different constant strains at this temperature. Finally, three strain rate sensitivity coefficients, corresponding to three different testing temperatures, were found for each material; and these were taken as equal to p values.

2) Determination of the R(x) function :

In accordance with Figure 19, the function of variation of radius along the axis of specimen was defined as

$$R(x) = R + y(x) \quad \text{for} \quad 0 \leq x \leq R_N \tag{68}$$

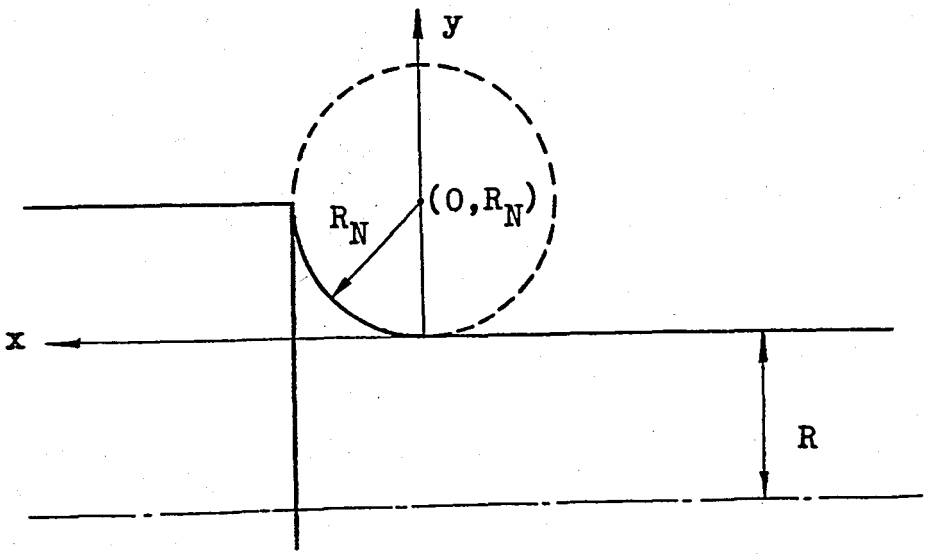

Figure 19 - Determination of radius function.

After writing the equation of the imaginary circle as

$$x^2 + (y - R_N)^2 = R_N^2 \tag{69}$$

and solving this equation for y, the function of variation of radius was obtained :

$$R(x) = R + R_N - \sqrt{R_N^2 - x^2} \tag{70}$$

3) Integration :

Using the computer program given in Appendix B, the integral in equation (65) was evaluated numerically after the substitution of equation (70). In this evaluation Riemann method was used; R and R_N were taken as 7.5 mm and 3.5 mm, respectively; and the operation was repeated for each p value.

4) Calculation of effective lengths :

Taking the gage length L equal to 15 mm, effective lengths were calculated from equation (65).

Strain rate sensitivity coefficients and effective lengths of two materials tested are given in Table III.

TABLE III - Strain Rate Sensitivity Coefficients and Effective Lengths of Materials

Material	Temperature (^{o}C)	Strain Rate Sensitivity Coefficient(m)	Effective Length L_E(mm)
Aluminum 1100	250	0.1004	17.28
	350	0.1530	17.76
	450	0.2016	18.10
Aluminum 2024	250	0.0795	17.04
	300	0.1317	17.58
	350	0.1554	17.78

With these L_E values at hand, shear strain and shear strain rate at critical radius were calculated from equations (63) and (64), respectively. Then, material flow curves were plotted for constant temperatures and constant shear strain rates.

In order to see the effects of temperature and strain rate on the deformation behavior of materials separately, flow curves were plotted once for different strain rates at constant temperatures, and once for different temperatures at constant strain rates.

Figure 20 shows the effects of temperature on the deformation behavior of aluminum 1100 for four different constant shear strain rates. Here, shear stress at critical radius is plotted as a function of shear strain at the same location. From 20(a) to 20(d), each figure belongs to a different constant shear strain rate and includes flow curves obtained for three temperature values (250^{o}C, 350^{o}C,

450^{o}C). Shear strain rates range from 6.84×10^{-3} rad/s to 0.694 rad/s and are given in decreasing order in Figures 20(a) to 20(d).

Temperature effects on the behavior of aluminum alloy 2024 are shown in Figure 21 for four different constant shear strain rates. Here, again, the variations of shear stress and shear strain are given for the critical radius. Temperature values are 250^{o}C, 300^{o}C and 350^{o}C for this material. From Figure 21(a) to Figure 21(d), each figure belongs to a different constant shear strain rate and they are ordered according to the decreasing shear strain rates.

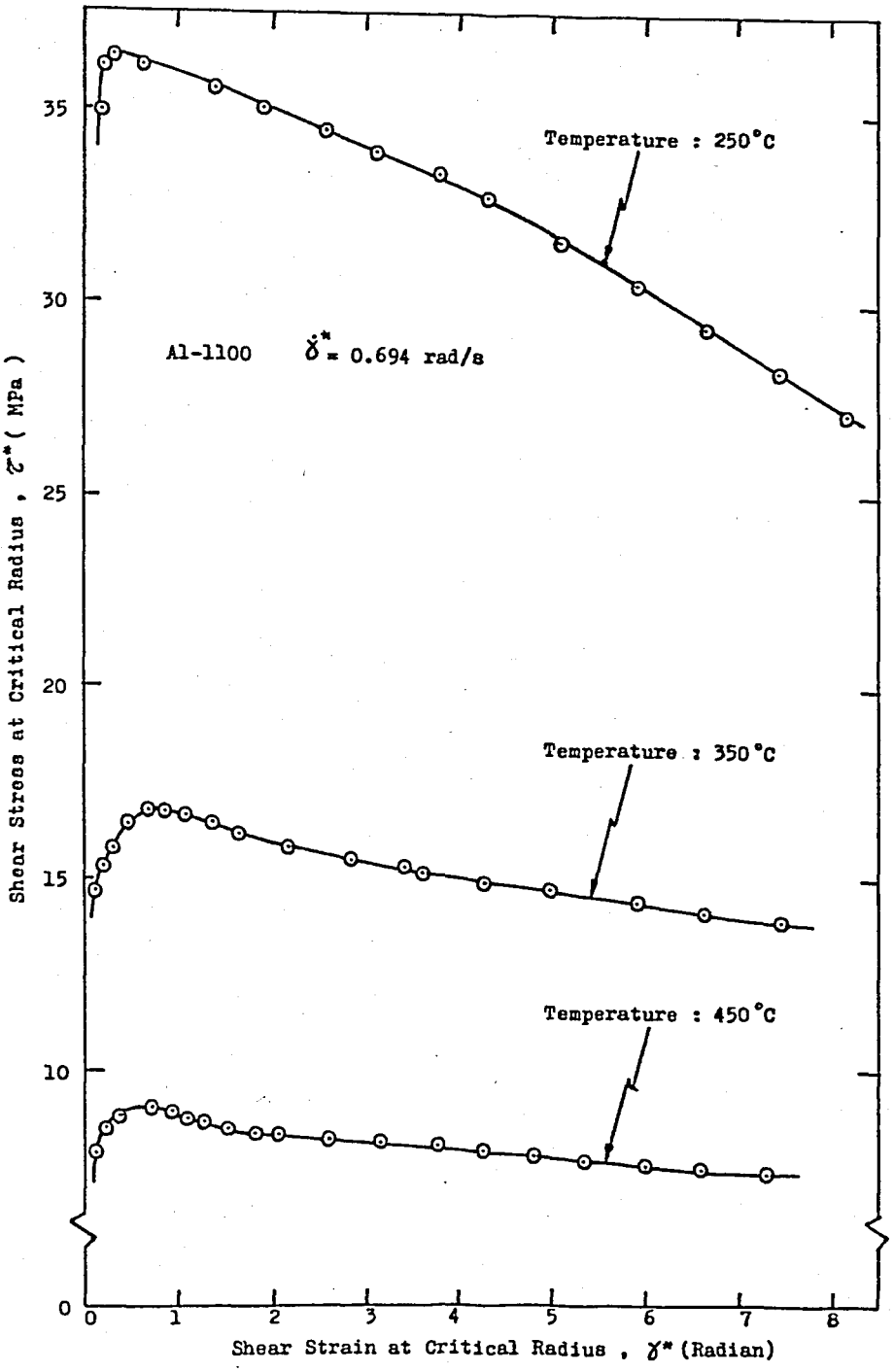
Temperature : 250°C
Al-1100 $\dot{\gamma}^*$ = 0.694 rad/s
Temperature : 350°C
Temperature : 450°C
Shear Stress at Critical Radius , τ^* (MPa)
Shear Strain at Critical Radius , γ^* (Radian)
0
10
15
20
25
30
35
0
1
2
3
4
5
6
7
8

(a)

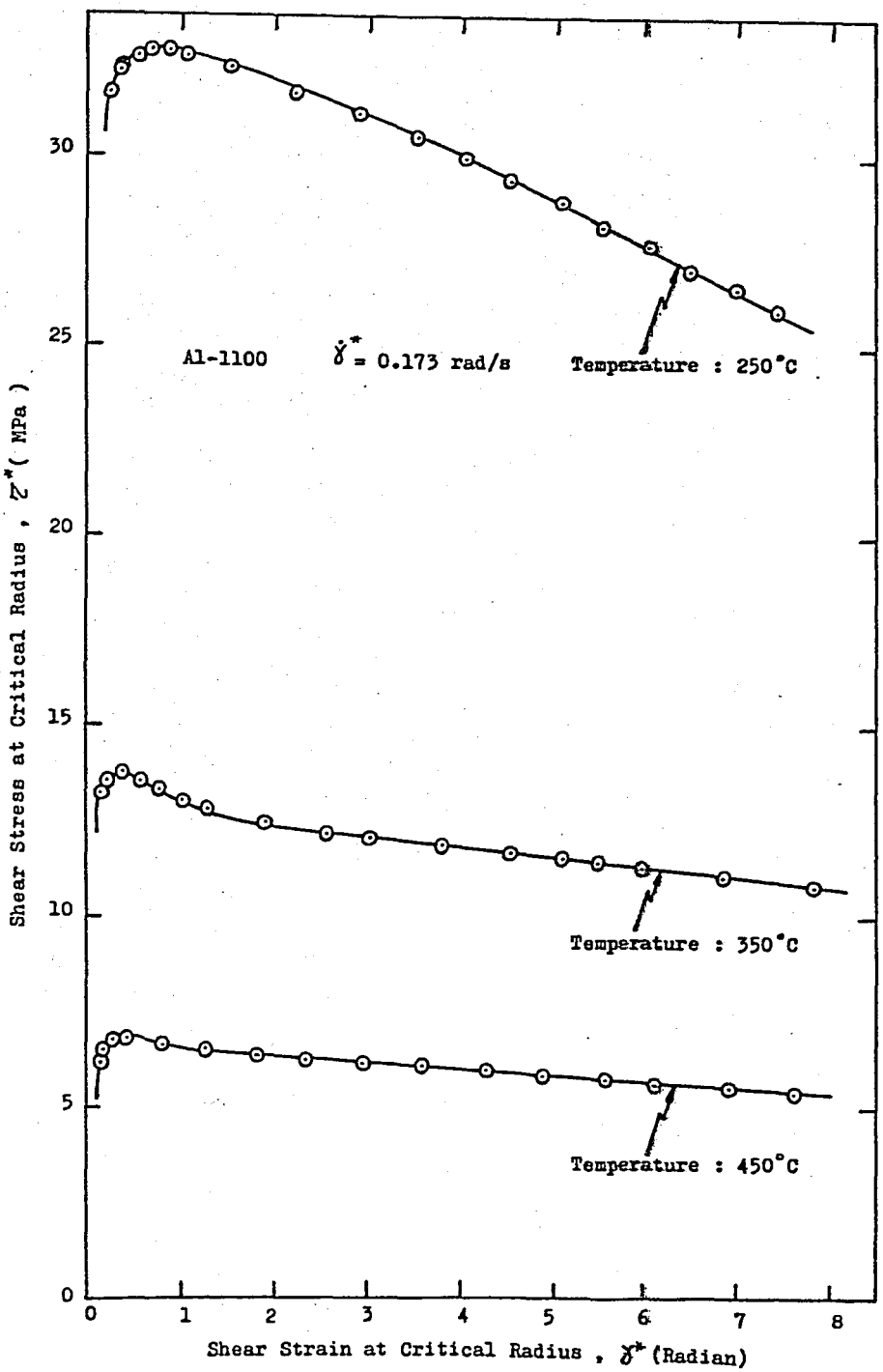
Al-1100
$\dot{\gamma}^*$ = 0.173 rad/s
Temperature : 250°C
Temperature : 350°C
Temperature : 450°C
Shear Stress at Critical Radius , τ^* (MPa)
Shear Strain at Critical Radius , γ^* (Radian)
0
5
10
15
20
25
30
1
2
3
4
5
6
7
8

(b)

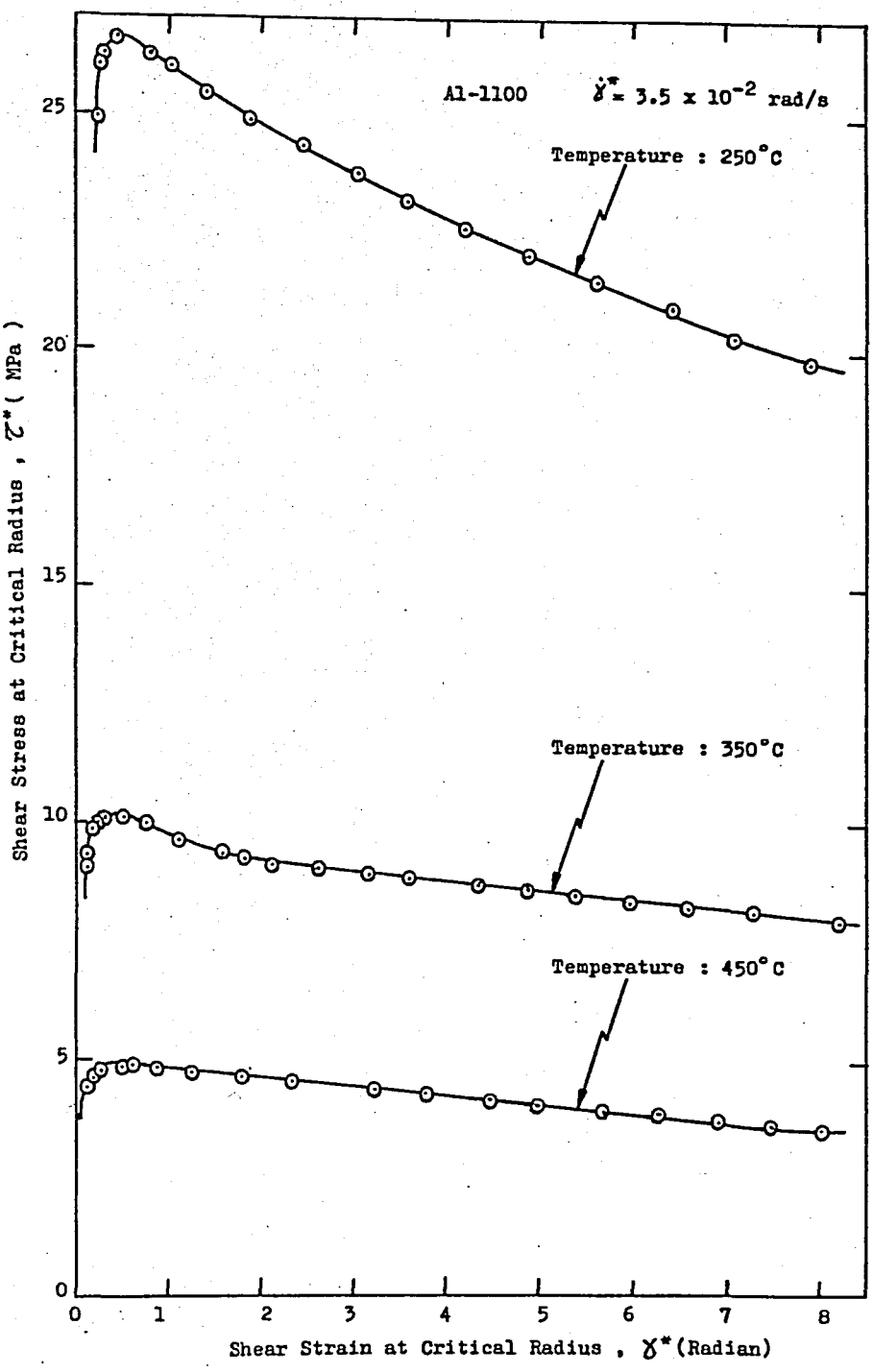
Al-1100
$\dot{\gamma}^* = 3.5 \times 10^{-2}$ rad/s
Temperature : 250°C
Temperature : 350°C
Temperature : 450°C
Shear Stress at Critical Radius , τ^* (MPa)
Shear Strain at Critical Radius , γ^* (Radian)
0
5
10
15
20
25
0
1
2
3
4
5
6
7
8

(c)

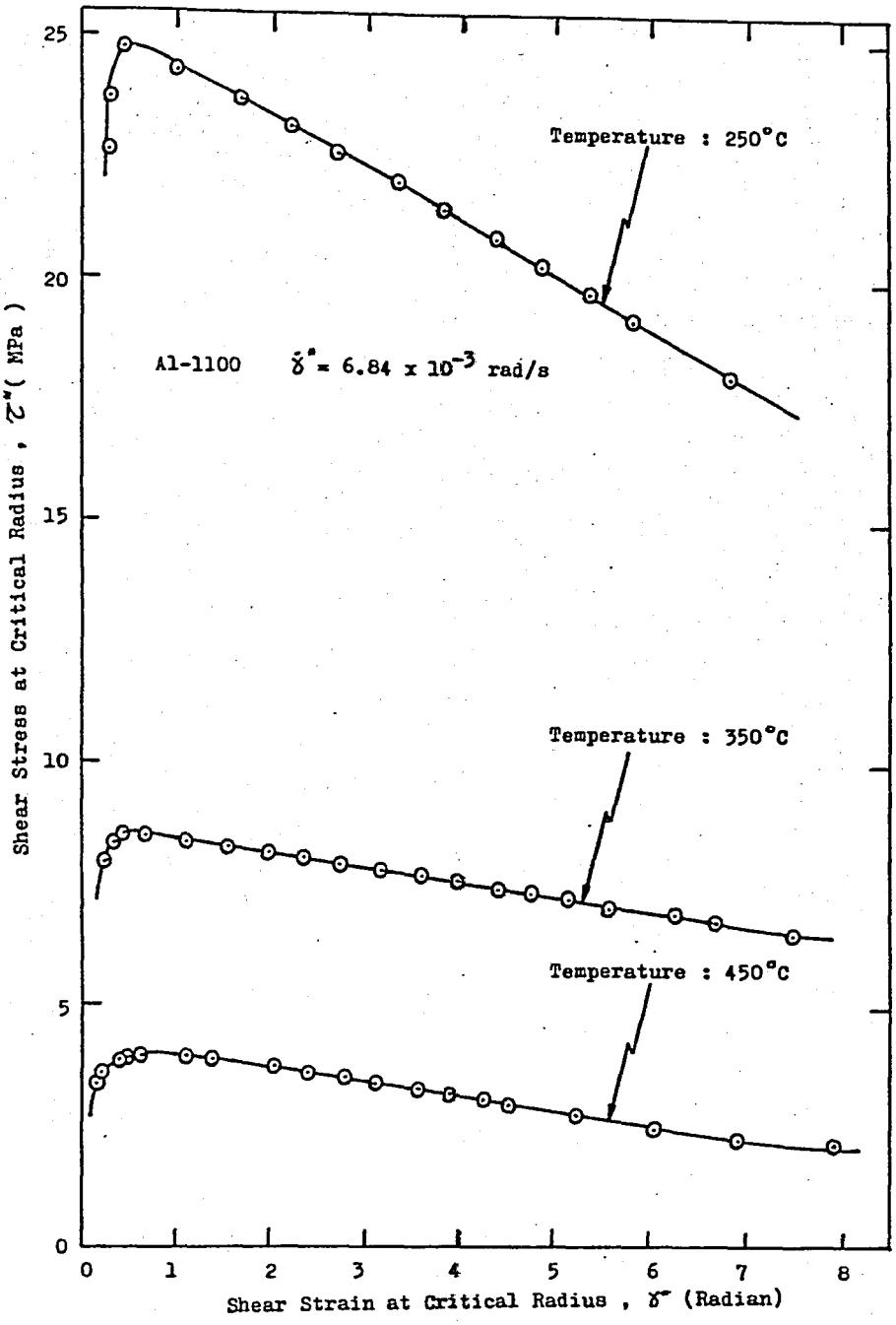

(d)

Figure 20 - Effects of temperature on the deformation behavior of aluminum 1100 at constant shear strain rate. (a) $\dot{\gamma}^* = 0.694$ rad/s, (b) $\dot{\gamma}^* = 0.173$ rad/s, (c) $\dot{\gamma}^* = 3.5 \times 10^{-2}$ rad/s (c) $\dot{\gamma}^* = 6.84 \times 10^{-3}$ rad/s.

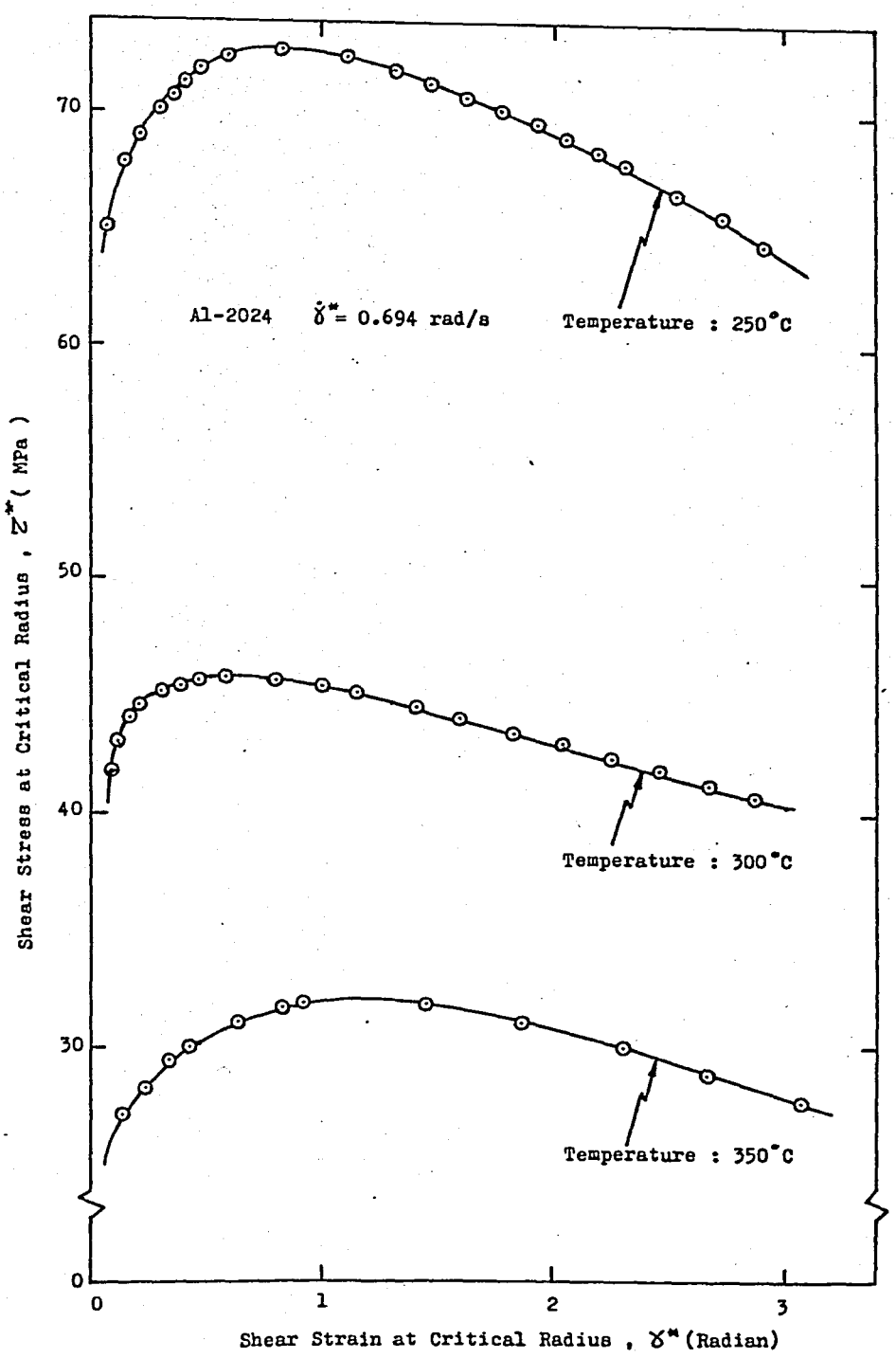
Al-2024 $\dot{\gamma}^*$= 0.694 rad/s
Temperature : 250°C
Temperature : 300°C
Temperature : 350°C
Shear Stress at Critical Radius , τ^*(MPa)
Shear Strain at Critical Radius , γ^*(Radian)
70
60
50
40
30
0
0
1
2
3

(a)

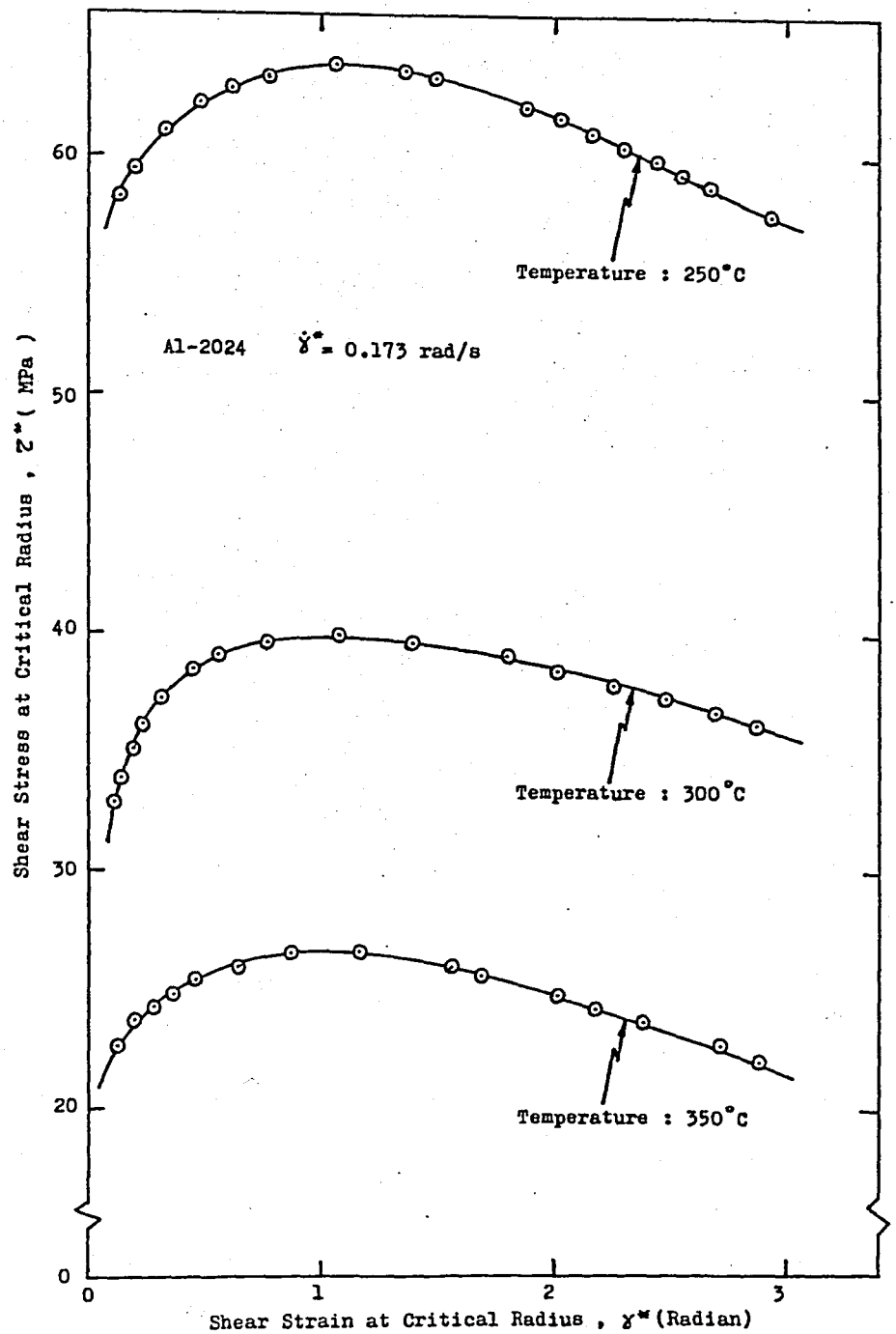
Shear Stress at Critical Radius , Z* (MPa)
Shear Strain at Critical Radius , γ* (Radian)
Al-2024 γ̇* = 0.173 rad/s
Temperature : 250°C
Temperature : 300°C
Temperature : 350°C
0
20
30
40
50
60
0
1
2
3

(b)

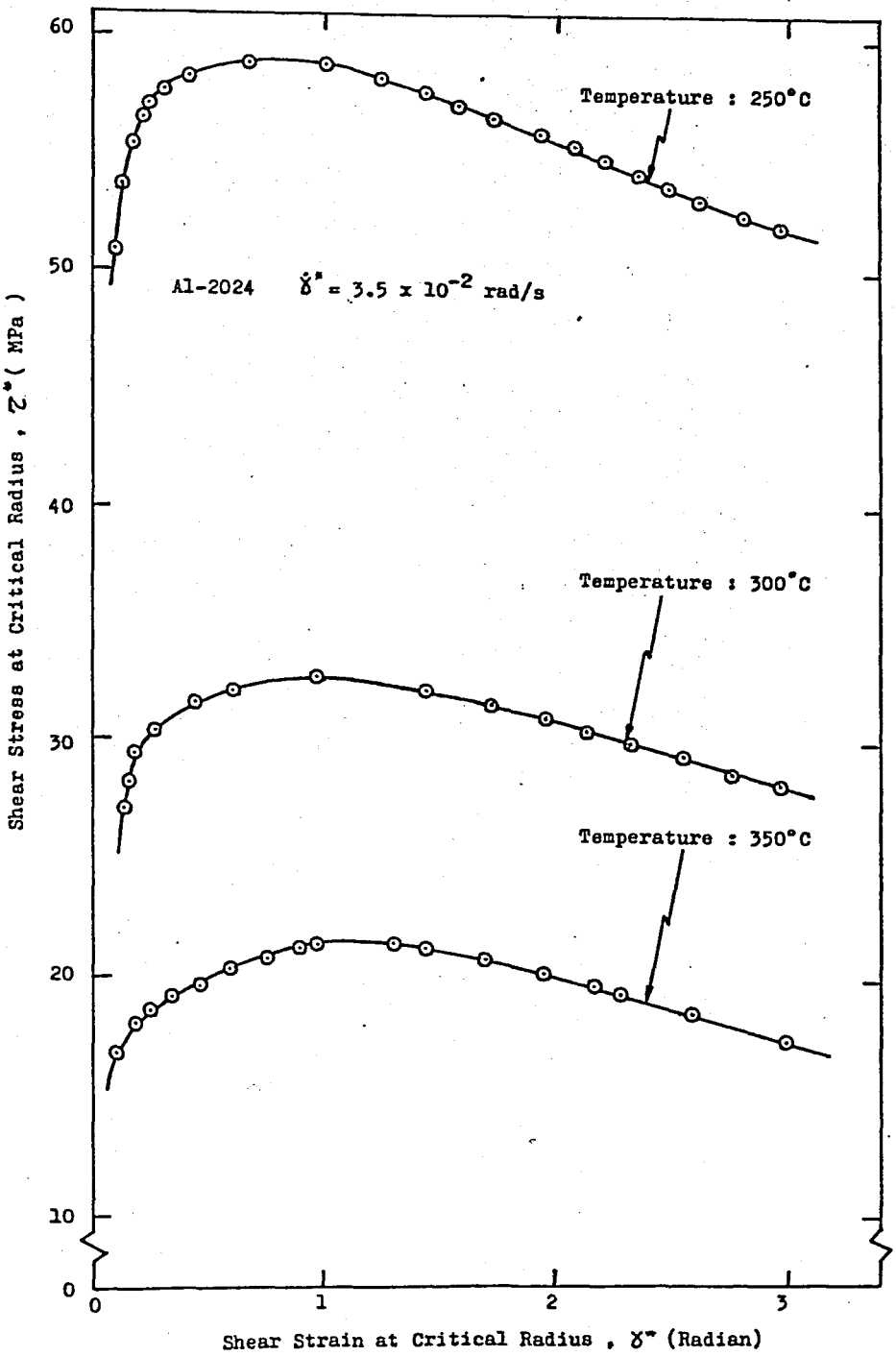
Temperature : 250°C
Al-2024 $\dot{\gamma}^* = 3.5 \times 10^{-2}$ rad/s
Temperature : 300°C
Temperature : 350°C
Shear Stress at Critical Radius , τ^* (MPa)
Shear Strain at Critical Radius , γ^* (Radian)
60
50
40
30
20
10
0
0
1
2
3

(c)

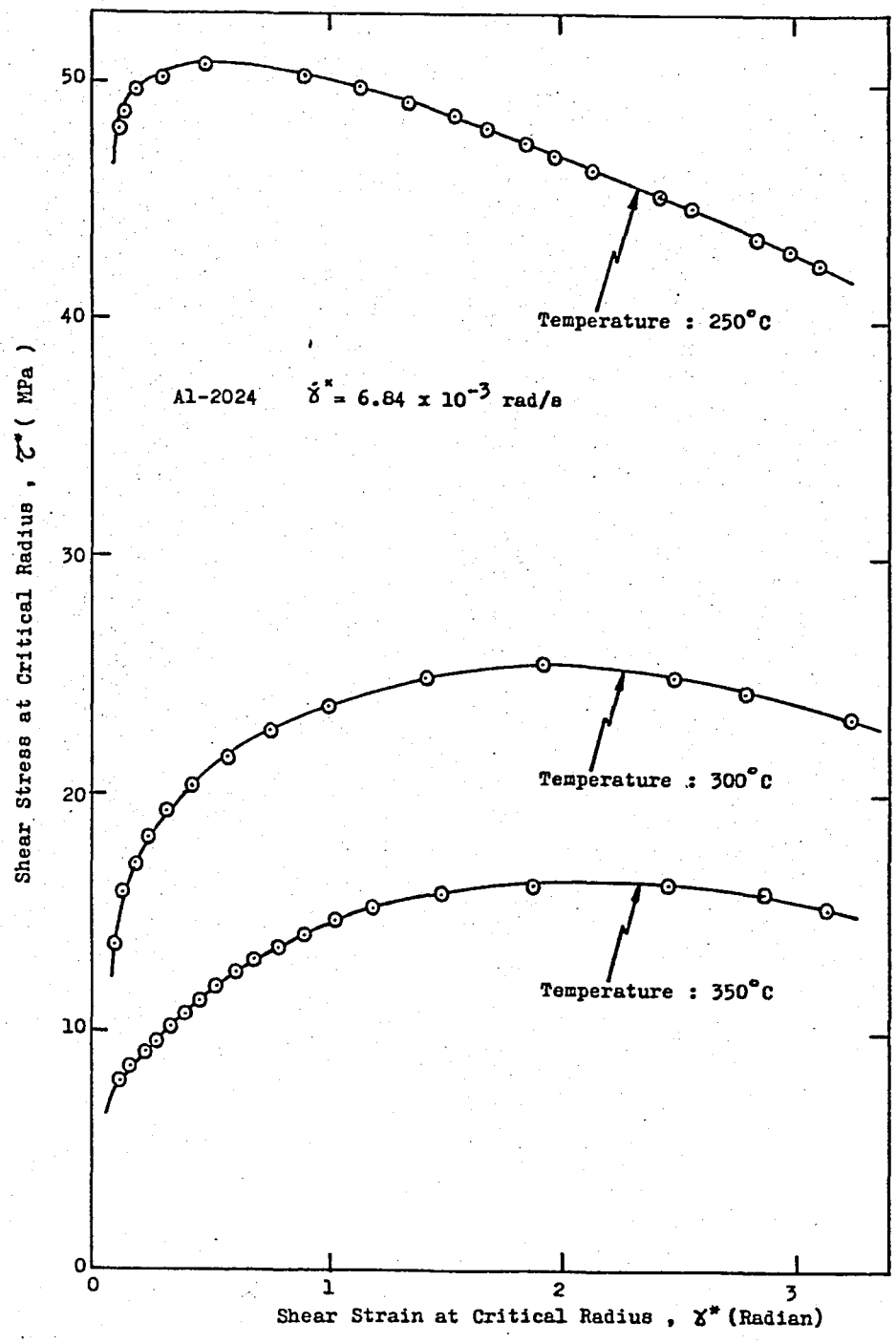

(d)

Figure 21 - Effects of temperature on the deformation behavior of aluminum alloy 2024 at constant shear strain rate.
(a) $\dot{\gamma}^* = 0.694$ rad/s, (b) $\dot{\gamma}^* = 0.173$ rad/s
(c) $\dot{\gamma}^* = 3.5 \times 10^{-2}$ rad/s, (d) $\dot{\gamma}^* = 6.84 \times 10^{-3}$ rad/s.

Figure 22 shows the effects of strain rate on the deformation behavior of aluminum 1100 for three different constant temperatures. Here, shear stress at critical radius is plotted as a function of shear strain at the same location. From 22(a) to 22(c), each figure belongs to a different constant temperature and includes flow curves obtained for four shear strain rate values (0.694 rad/s, 0.173 rad/s, 3.5×10^{-2} rad/s, 6.84×10^{-3} rad/s). Temperatures range from 250^{o}C to 450^{o}C and are given in decreasing order in Figures 22(a) to 22(c).

In Figure 23, strain rate effects on the deformation behavior of aluminum alloy 2024 are shown for three different constant temperatures. Here again the variations of shear stress and shear strain are given for the critical radius. Shear strain rate values are the same as those chosen for aluminum 1100, and temperatures range from 250^{o}C to 350^{o}C. From Figure 23(a) to Figure 23(c), each figure belongs to a different constant temperature and they are ordered according to the decreasing temperatures.

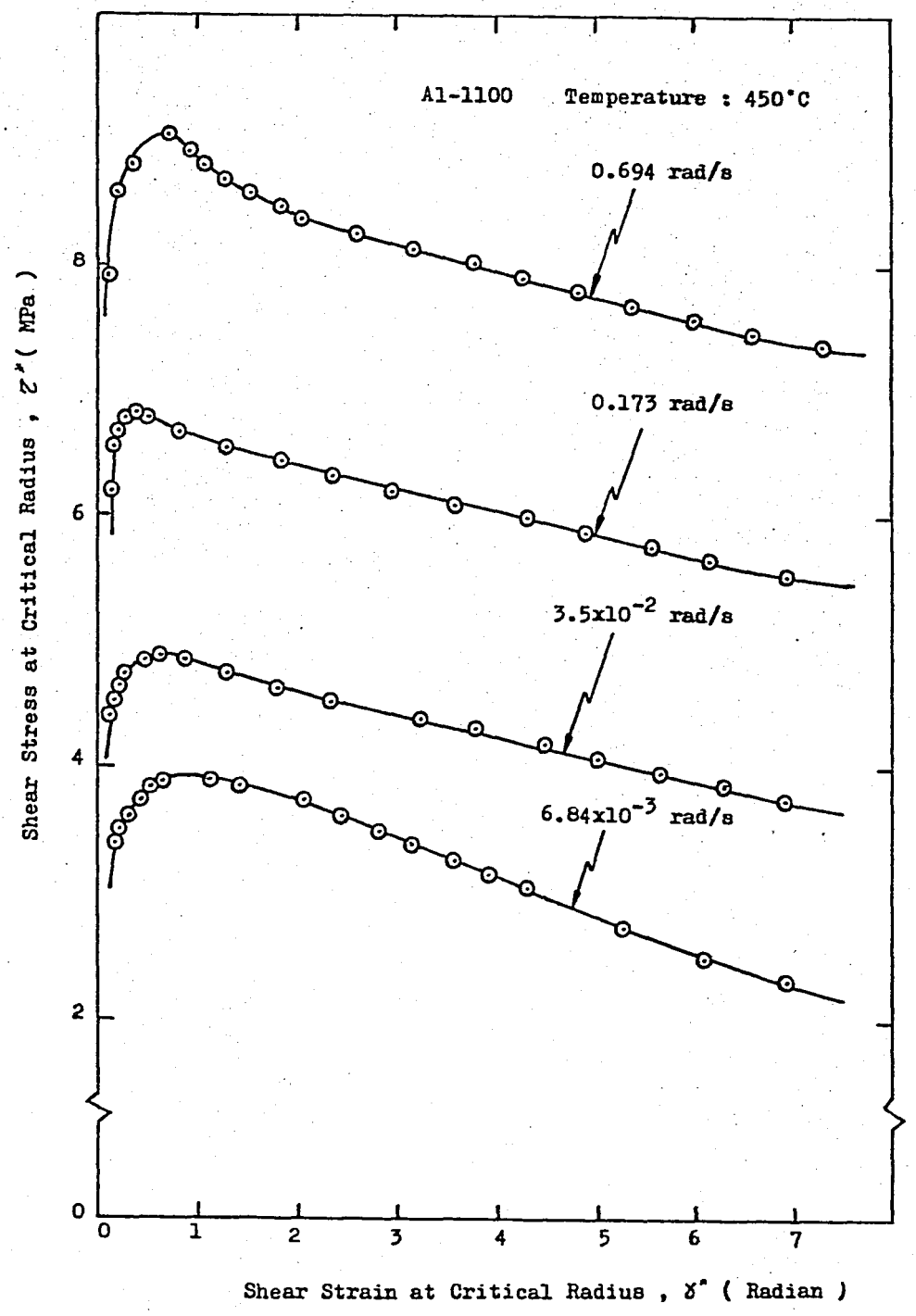
Al-1100 Temperature : 450°C
0.694 rad/s
0.173 rad/s
3.5x10^-2 rad/s
6.84x10^-3 rad/s
Shear Stress at Critical Radius , τ* (MPa)
Shear Strain at Critical Radius , γ* (Radian)
0
2
4
6
8
0
1
2
3
4
5
6
7

(a)

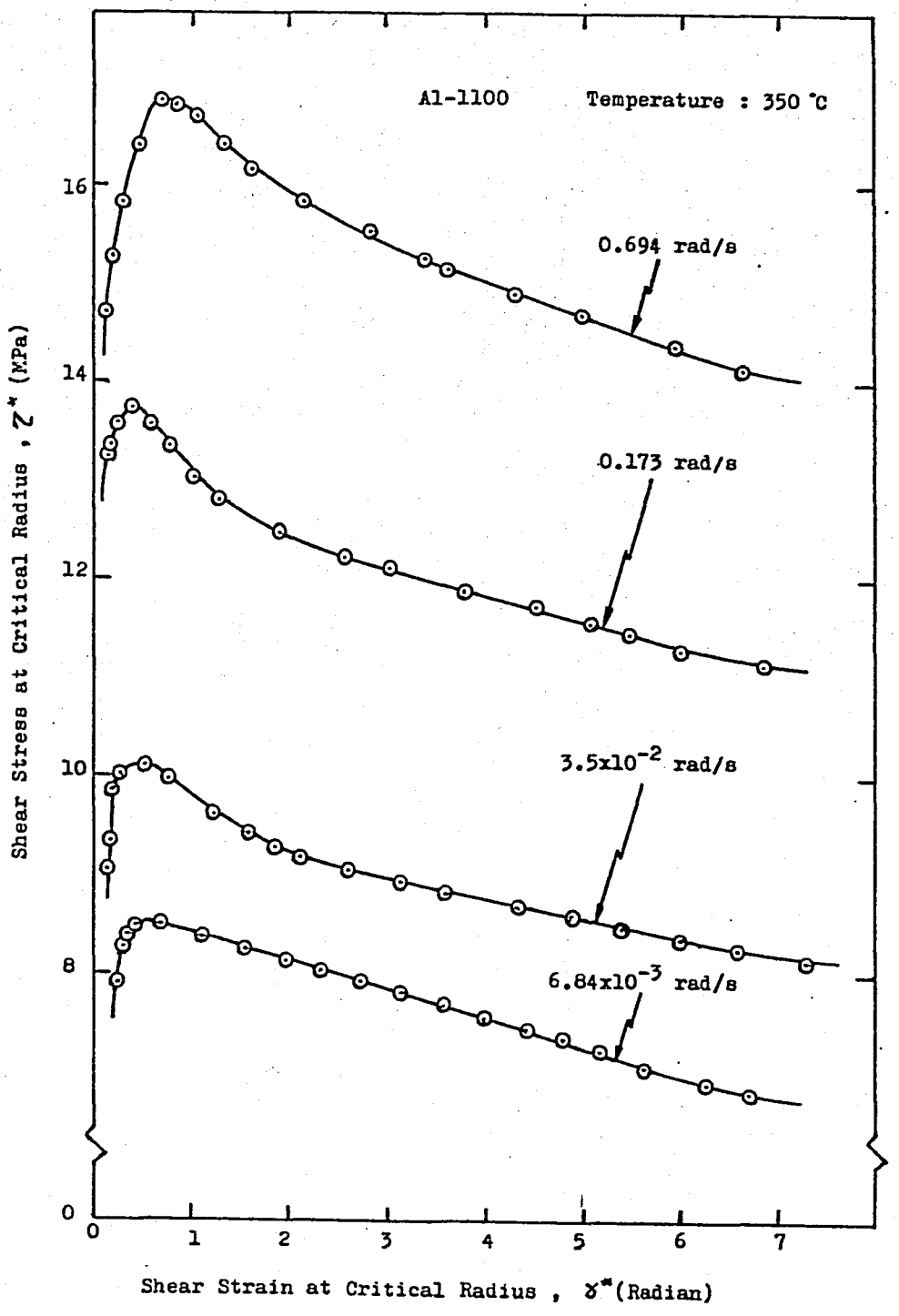
Al-1100
Temperature : 350 °C
0.694 rad/s
0.173 rad/s
3.5x10^{-2} rad/s
6.84x10^{-3} rad/s
Shear Stress at Critical Radius , τ^* (MPa)
Shear Strain at Critical Radius , γ^* (Radian)
0
8
10
12
14
16
0
1
2
3
4
5
6
7

(b)

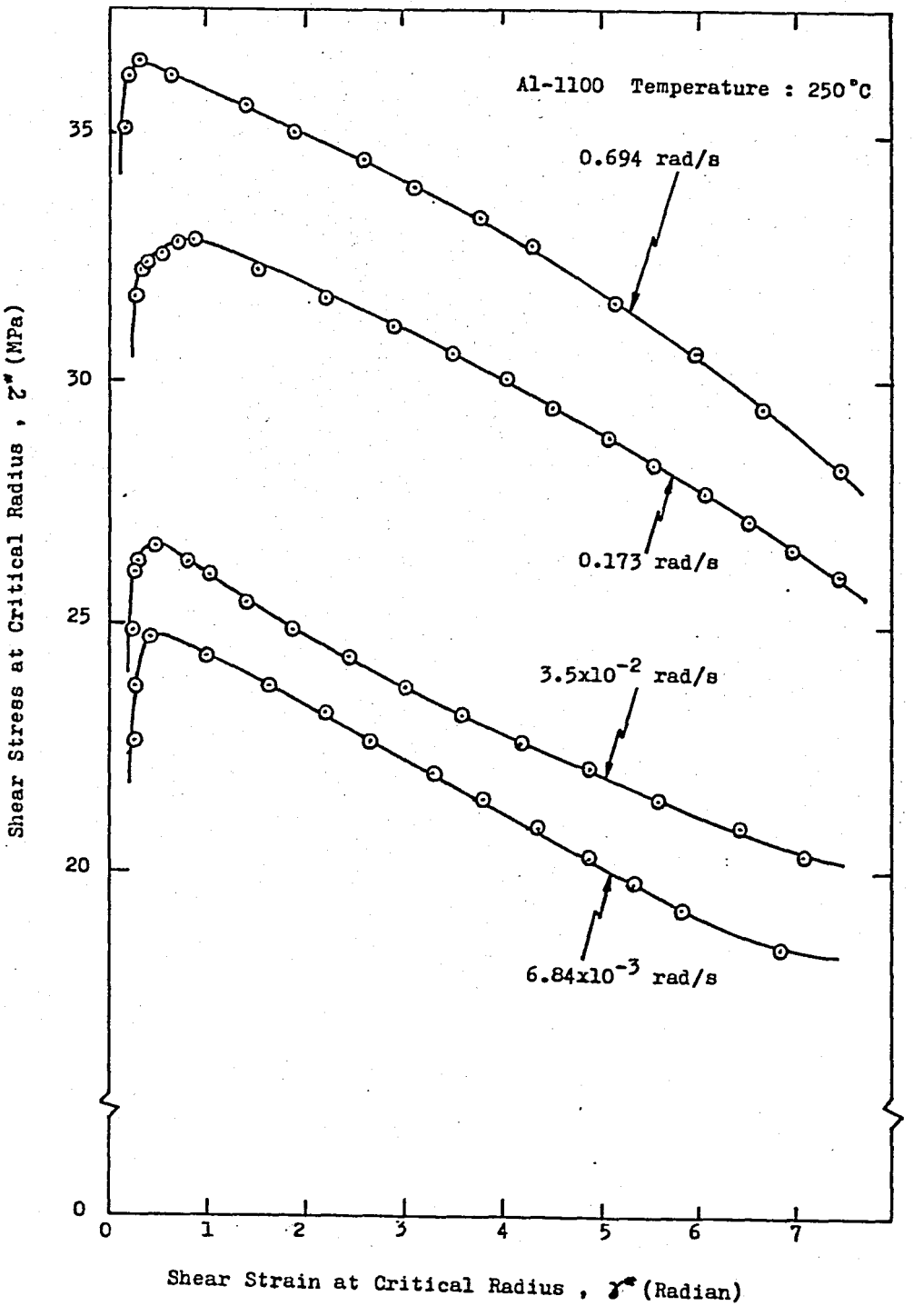

(c)

Figure 22 - Effects of strain rate on the deformation behavior of aluminum 1100 at constant temperature. (a) T = 450°C, (b) T = 350°C, (c) T = 250°C.

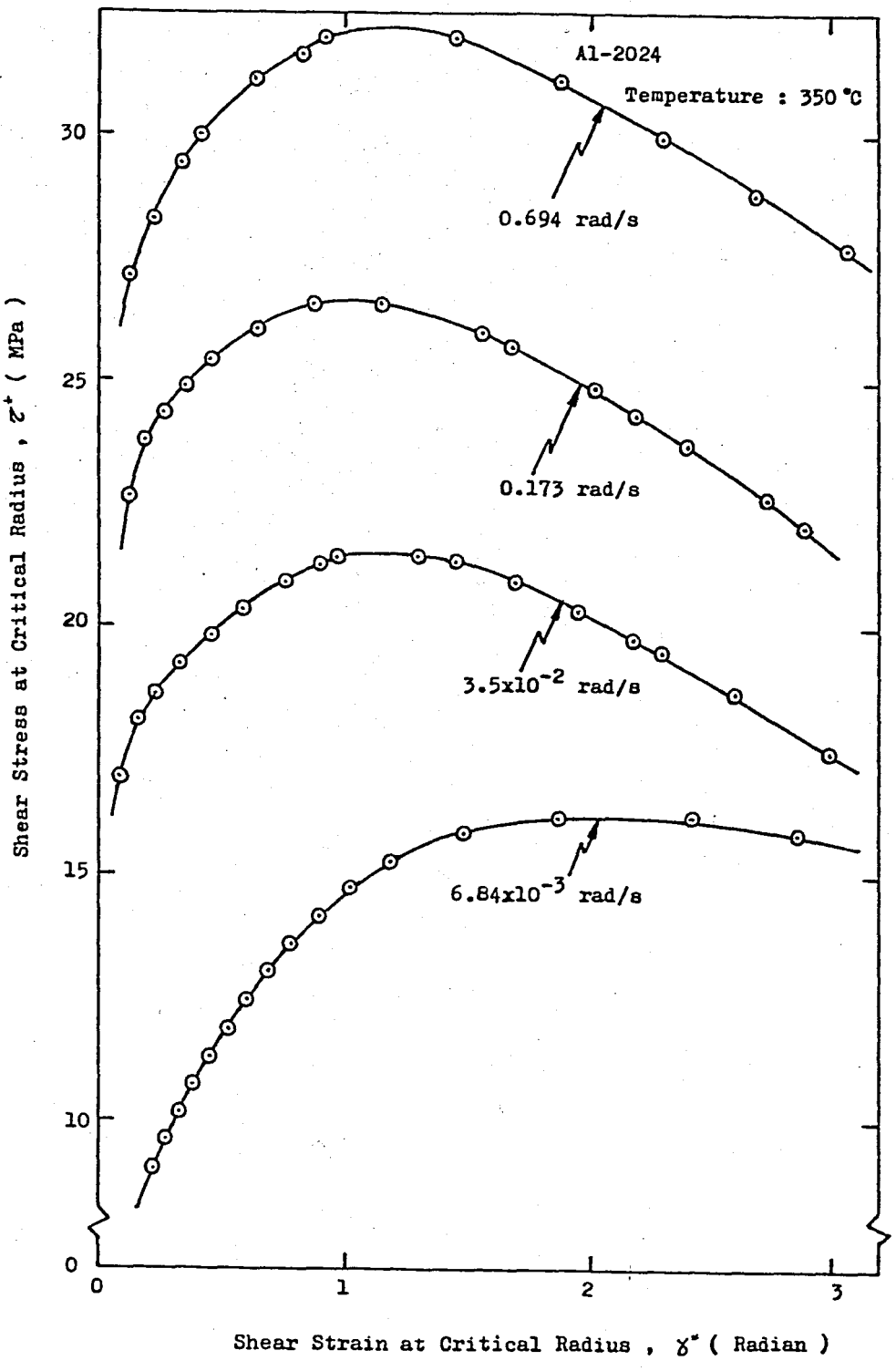
Al-2024
Temperature : 350 °C
0.694 rad/s
0.173 rad/s
3.5x10^-2 rad/s
6.84x10^-3 rad/s
Shear Stress at Critical Radius , τ* (MPa)
Shear Strain at Critical Radius , γ* (Radian)
0
10
15
20
25
30
0
1
2
3

(a)

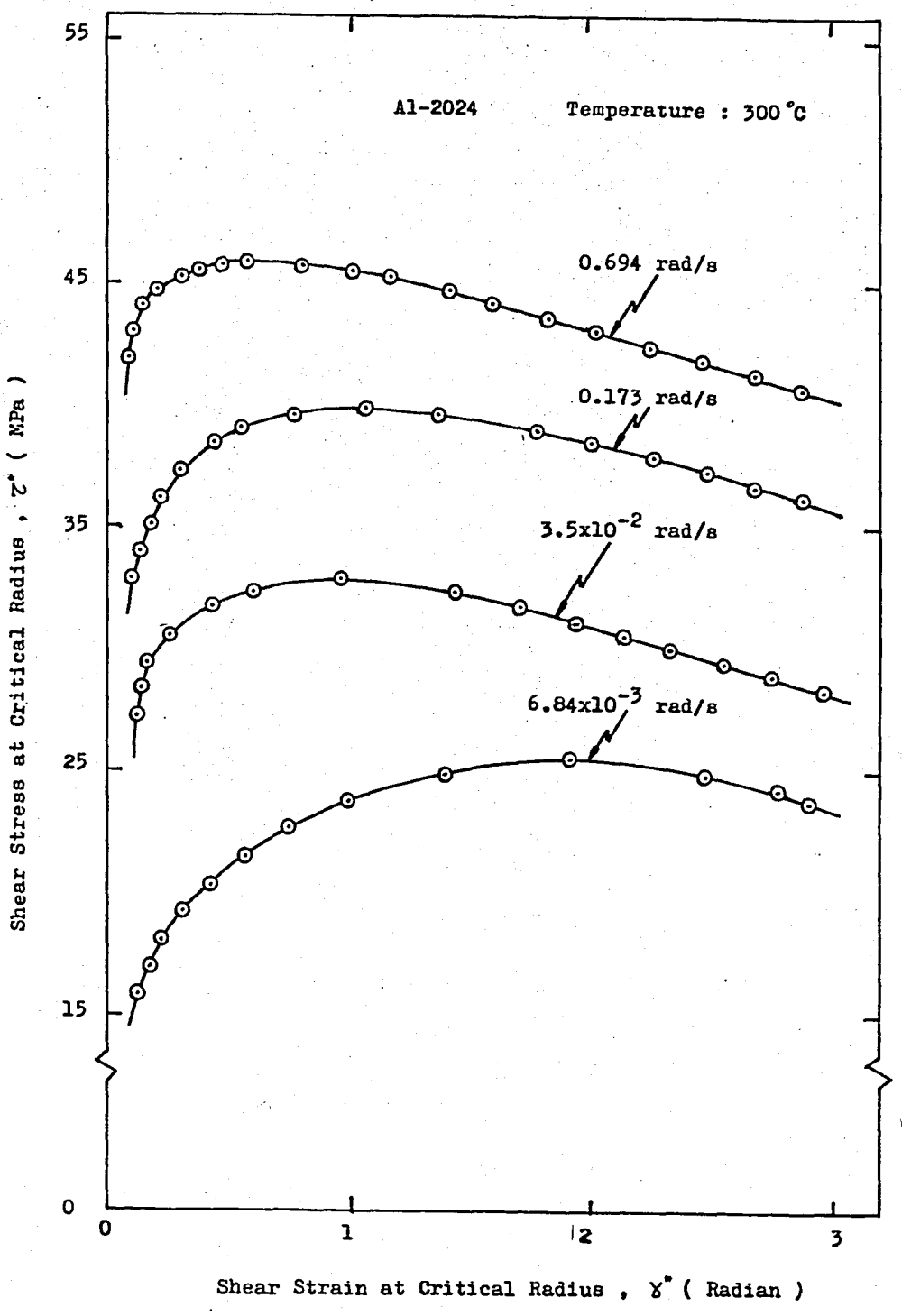
Al-2024
Temperature : 300 °C
0.694 rad/s
0.173 rad/s
3.5x10^-2 rad/s
6.84x10^-3 rad/s
Shear Stress at Critical Radius , τ* (MPa)
Shear Strain at Critical Radius , γ* (Radian)
55
45
35
25
15
0
0
1
2
3

(b)

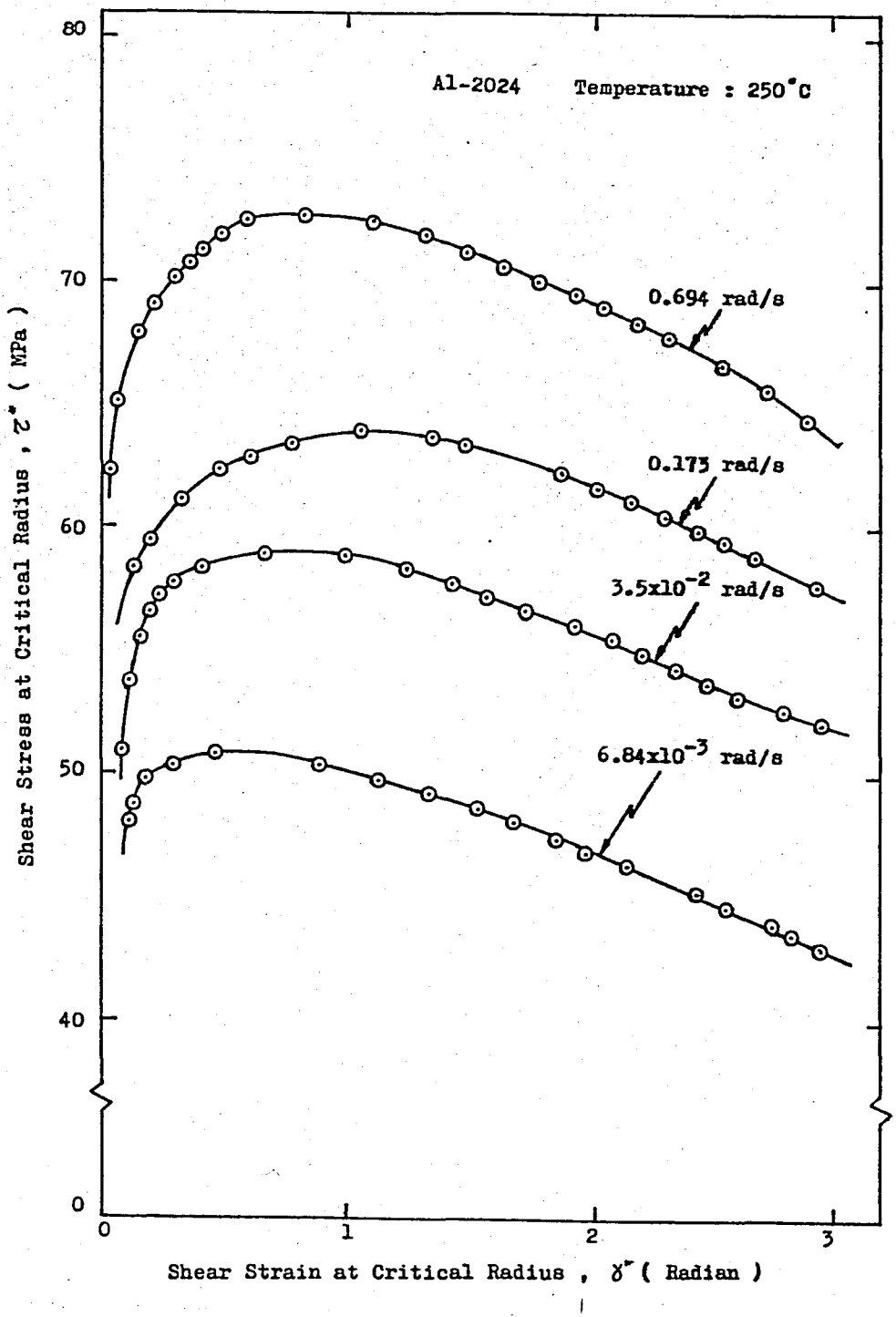

(c)

Figure 23 - Effects of strain rate on the deformation behavior of aluminum alloy 2024 at constant temperature.
(a) T = 350°C, (b) T = 300°C, (c) T = 250°C.

6.2 MICROSTRUCTURES

Figure 24 shows the initial microstructure of aluminum 1100 in as-extruded and air-cooled condition. Figure 24(a) and Figure 24(c) were taken from the near-surface region and near-axis region, respectively. The transition-region between these two structures of different character is shown in Figure 24(b). All microphotographs belong to a cross-section perpendicular to extrusion direction.

(a)

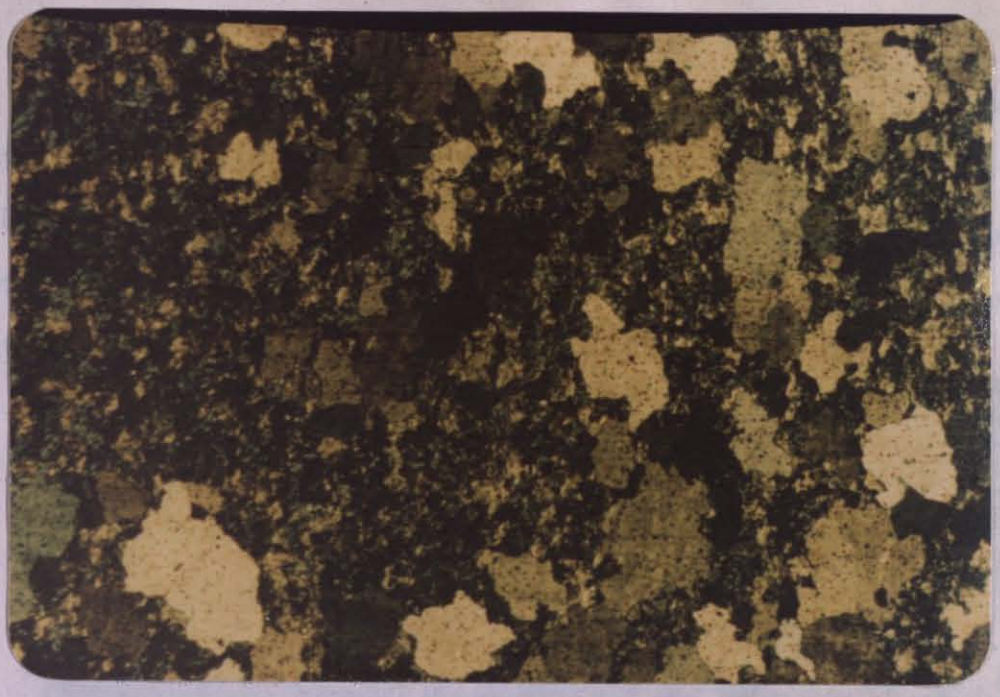

(b)

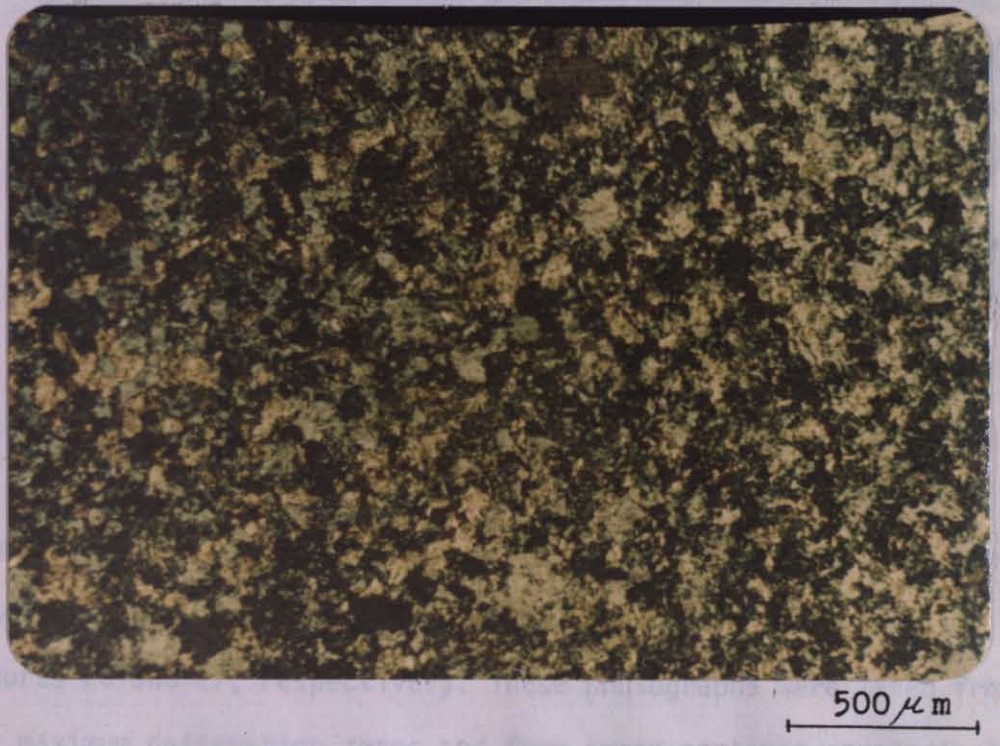

(c)

Figure 24 - Initial microstructure of aluminum 1100, extruded, air-cooled, polarized light, magnification 50X, (a) Near-surface region, (b) Transition region, (c) Near-axis region.

Figure 25 shows the microstructure of an aluminum 1100 specimen deformed at 250°C and with a critical-radius-shear-strain-rate of 6.84×10^{-3} rad/s, and, then, air-cooled. It was taken from the maximum deformation zone and from a cross-section perpendicular to specimen axis.

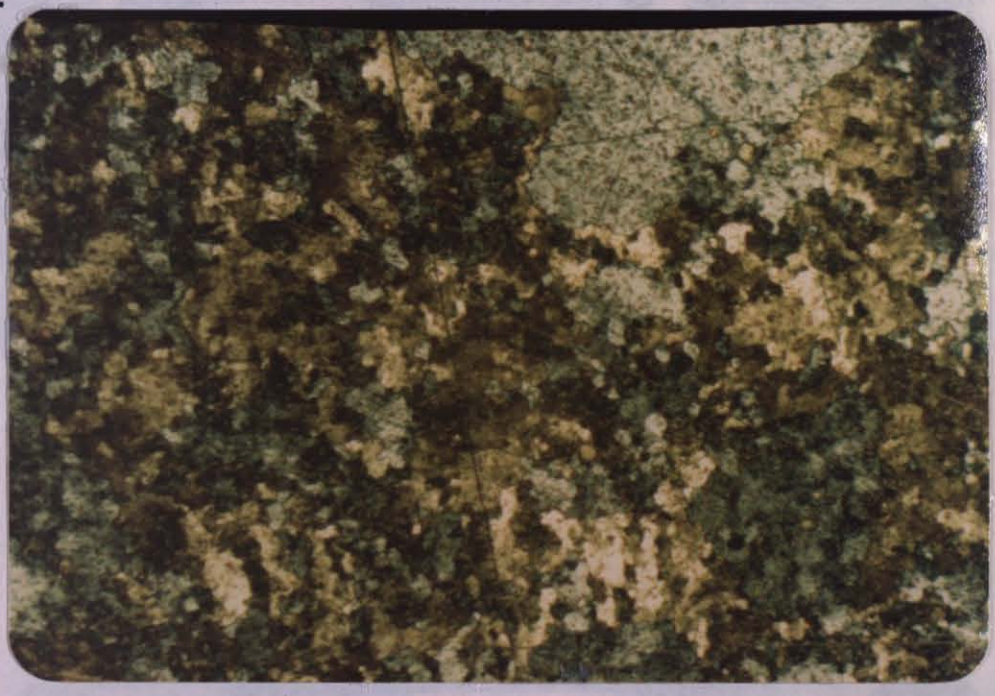

Figure 25 - Aluminum 1100, after hot-torsion at 250°C with a deformation rate of $\dot{\gamma}^{*} = 6.84 \times 10^{-3}$ rad/s and cooling in air, polarized light, magnification 200 X.

The microphotographs shown in Figure 26 and 27 were taken from specimens deformed at 450°C and then air-cooled. Deformation rates were $\dot{\gamma}^{*} = 6.84 \times 10^{-3}$ rad/s and $\dot{\gamma}^{*} = 0.694$ rad/s for those in Figures 26 and 27, respectively. These photographs were taken from the maximum deformation zones and from cross-sections perpendicular to specimen axes.

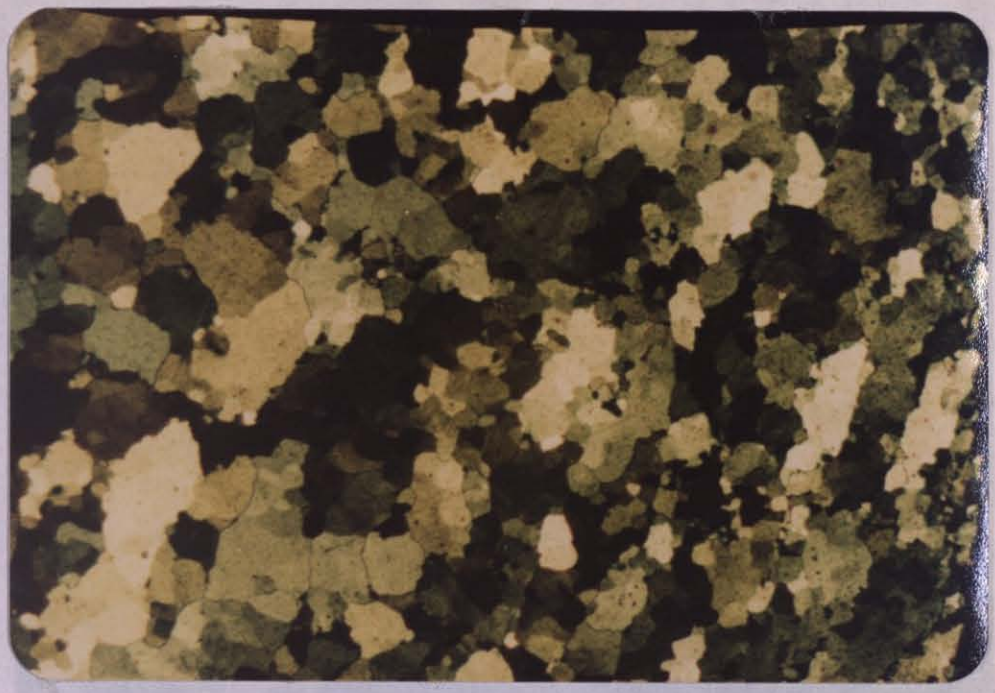

(a)

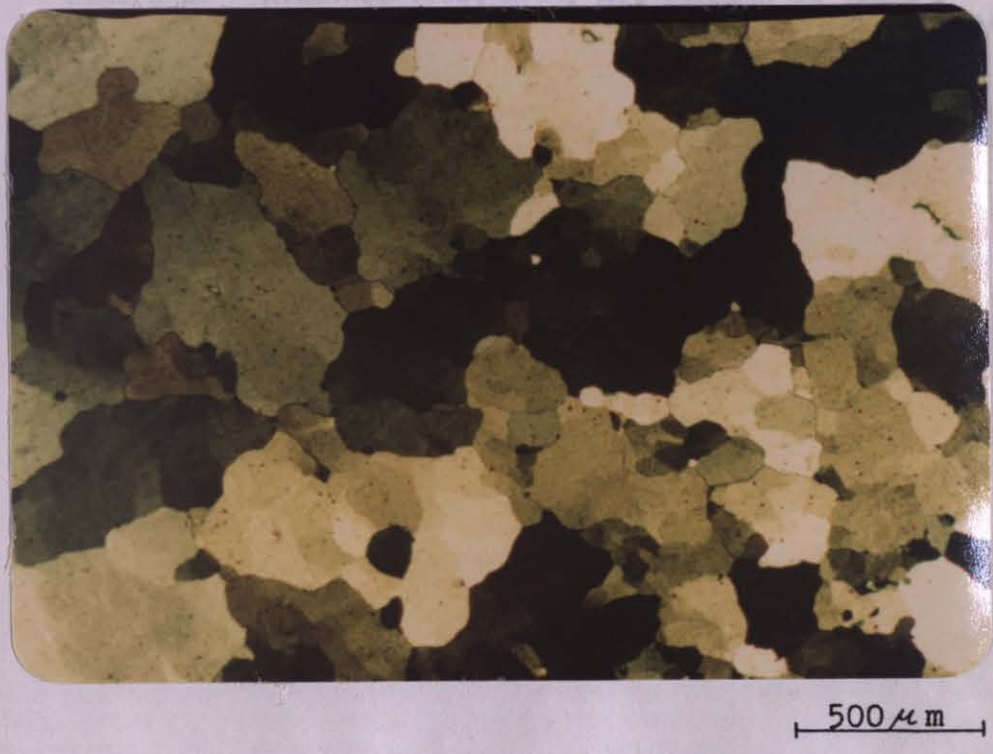

(b)

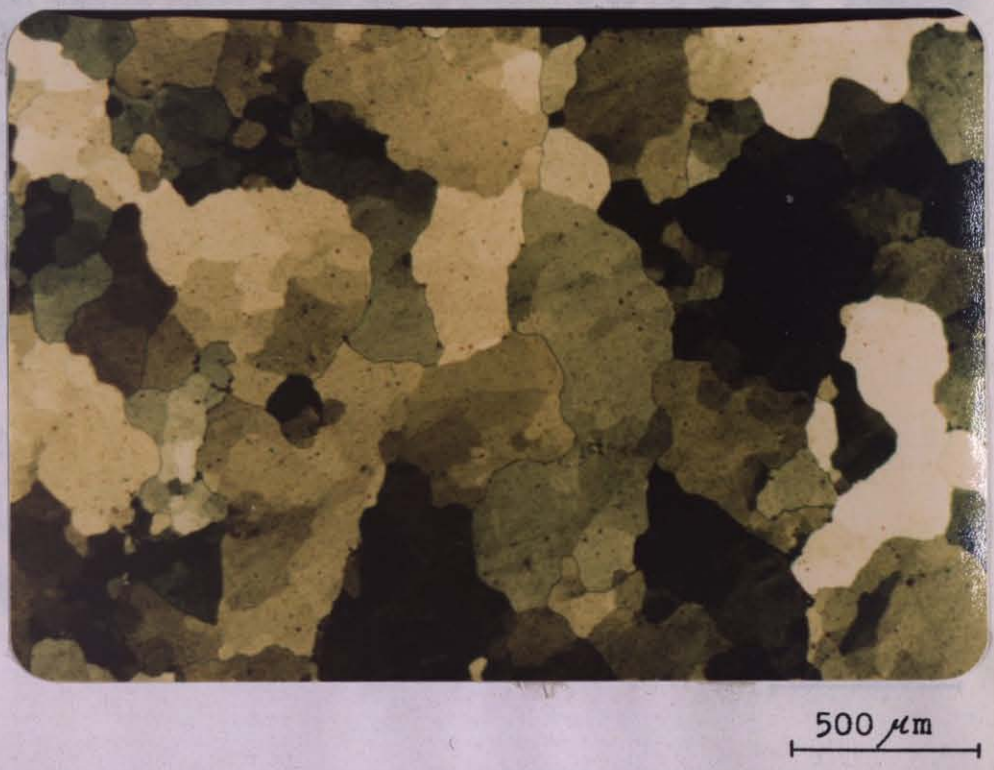

(c)

Figure 26 - Aluminum 1100, after hot-torsion at 450°C with a deformation rate of $\dot{\gamma}^{*} = 6.84 \times 10^{-3}$ rad/s and cooling in air, polarized light, magnification 50 X. (a) Near-surface region, (b) Transition region, (c) Near-axis region.

(a)

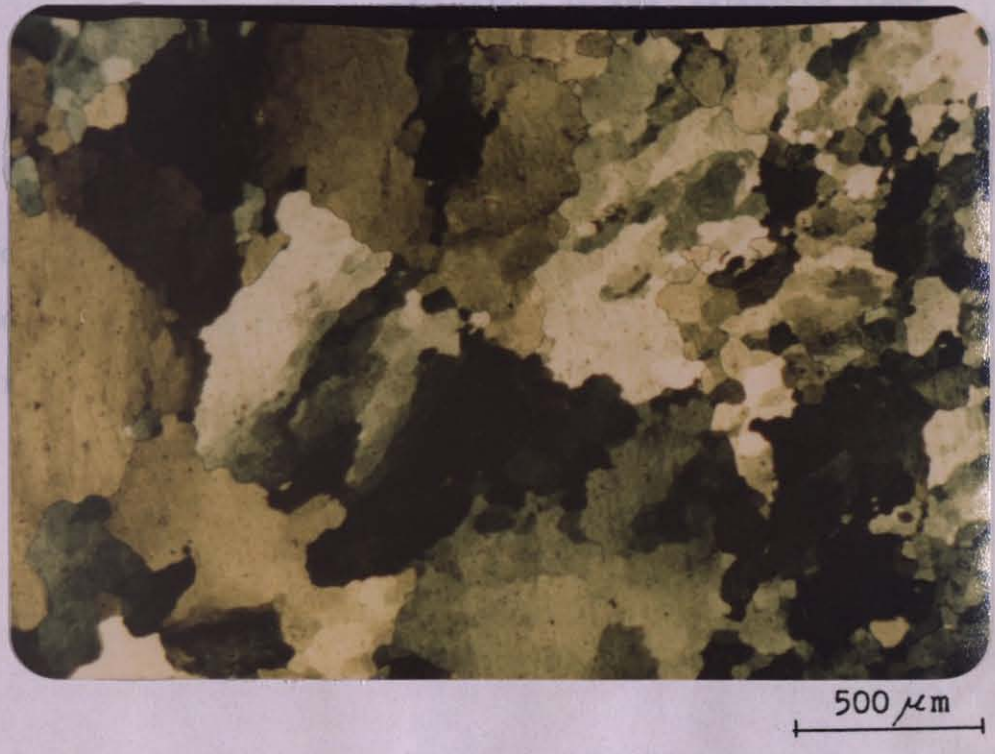

(b)

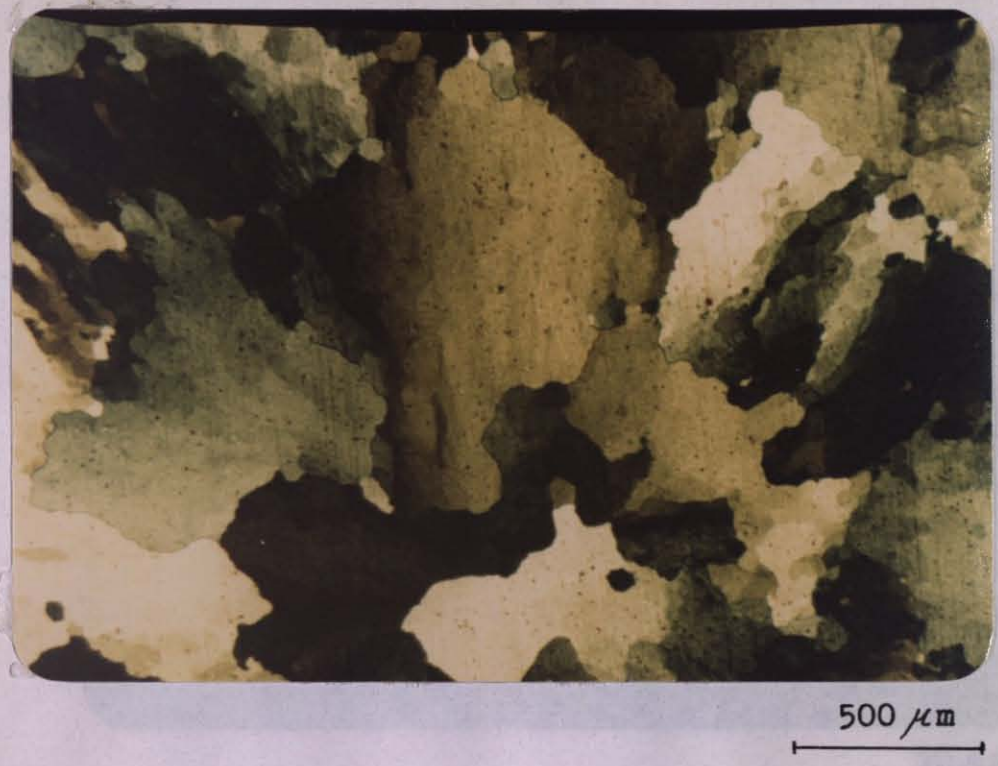

(c)

Figure 27 - Aluminum 1100, after hot-torsion at 450°C with a deformation rate of $\dot{\gamma}^* = 0.694$ rad/s and cooling in air, polarized light, magnification 50 X. (a) Near-surface region, (b) Transition region, (c) Near-axis region.

The initial microstructure of aluminum alloy 2024 in as-extruded and water-quenched condition is shown in Figure 28. This micro-photograph was taken from a cross-section perpendicular to extrusion direction.

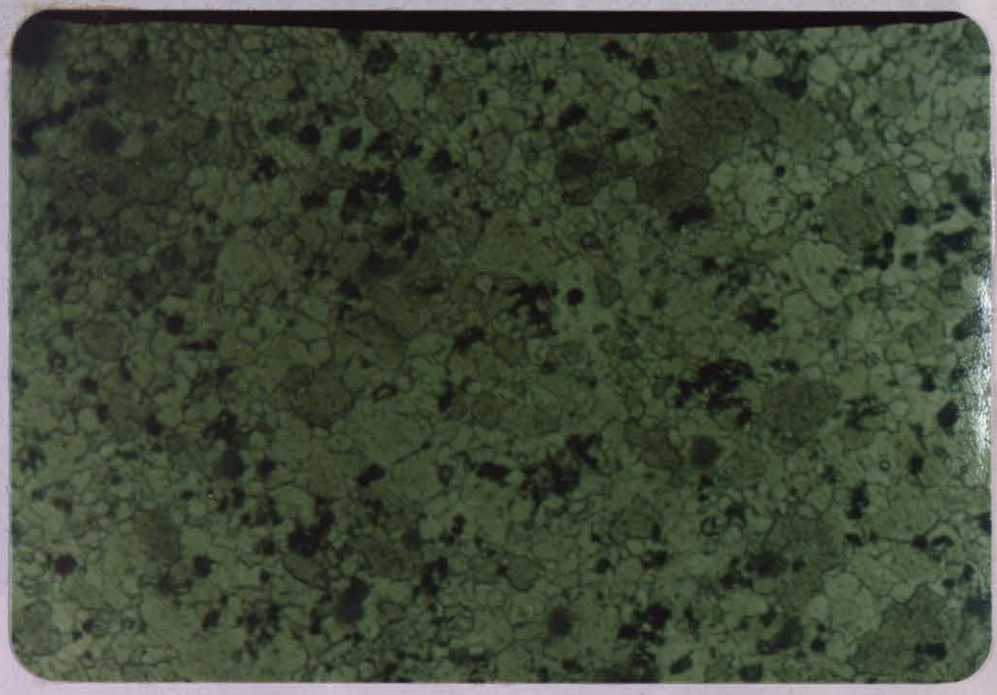

Figure 28 - Initial microstructure of aluminum alloy 2024, extruded, water-quenched, magnification 500 X.

Figures 29 and 30 show the microstructures of aluminum alloy 2024 after hot-torsion at 250°C and 350°C, respectively. These microphotographs were taken from the fracture zone and from a cross-section perpendicular to axes of specimens.

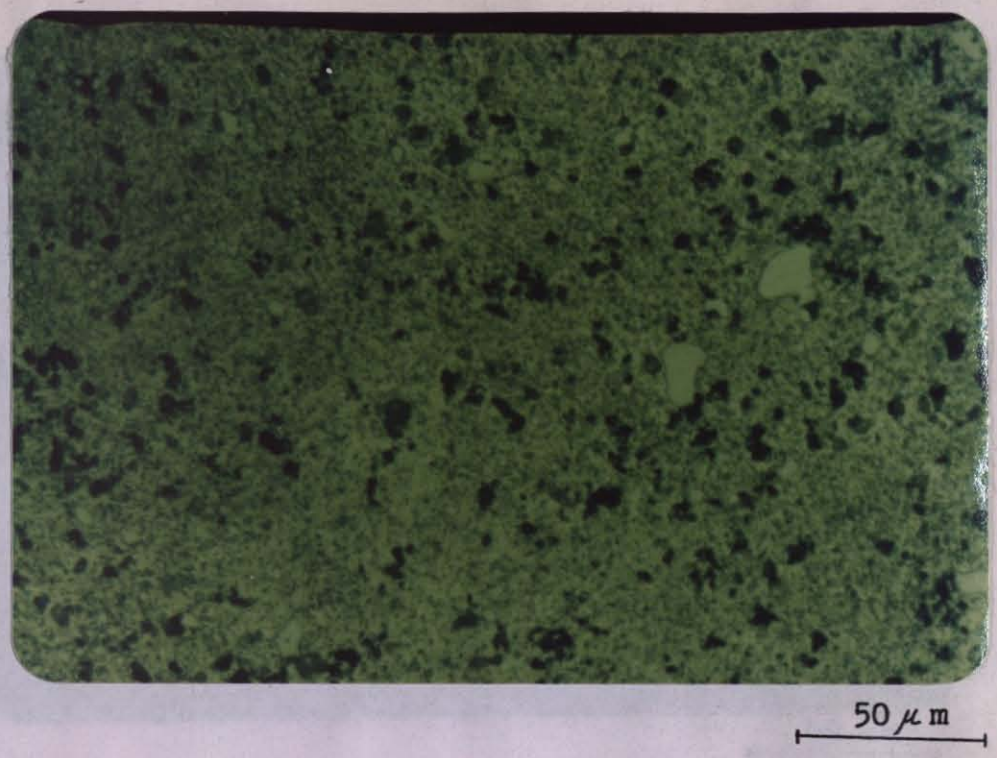

(a)

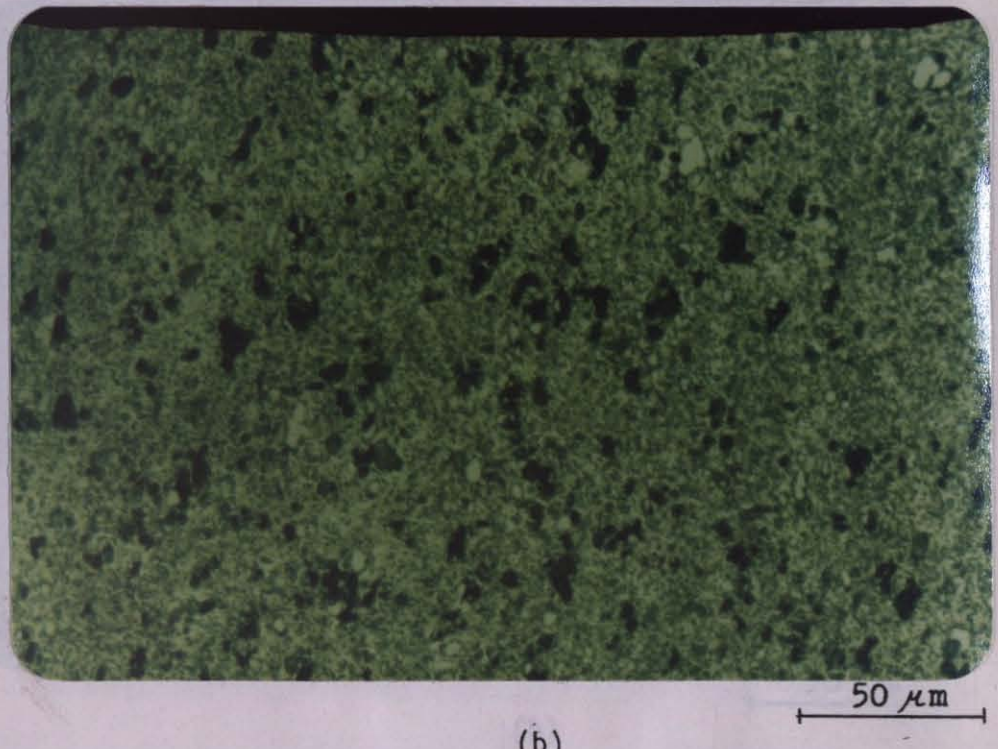

(b)

Figure 29 - Aluminum alloy 2024, after hot-torsion at 250°C and cooling in air, magnification 500 X.
(a) $\dot{\gamma}^* = 6.84 \times 10^{-}$ rad/s, (b) $\dot{\gamma}^* = 0.694$ rad/s.

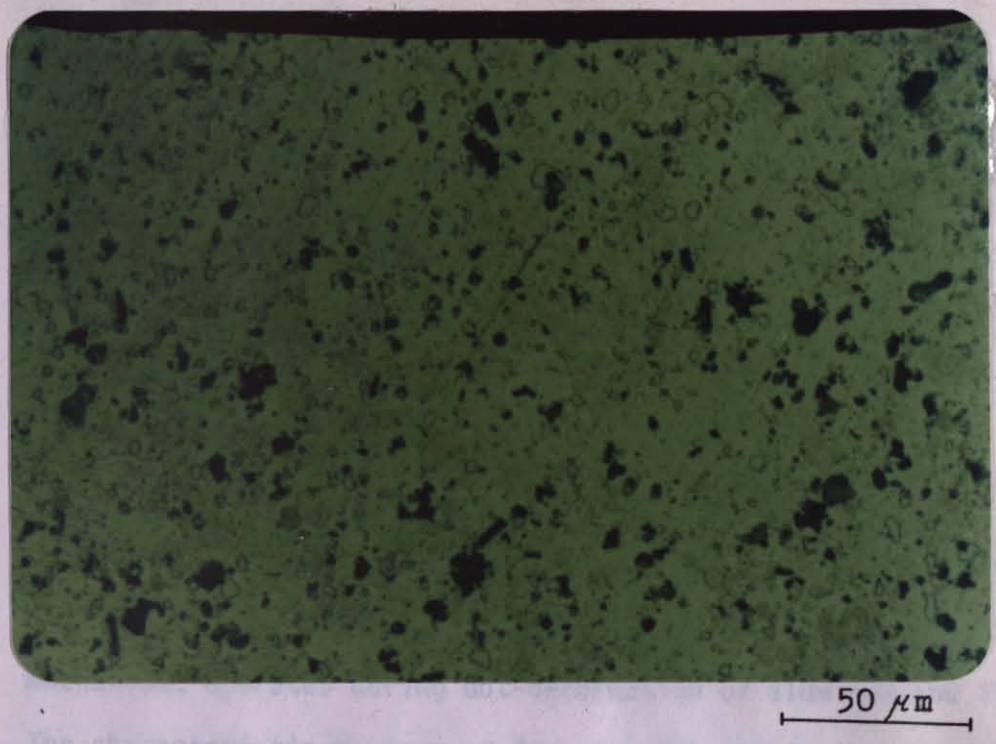

(a)

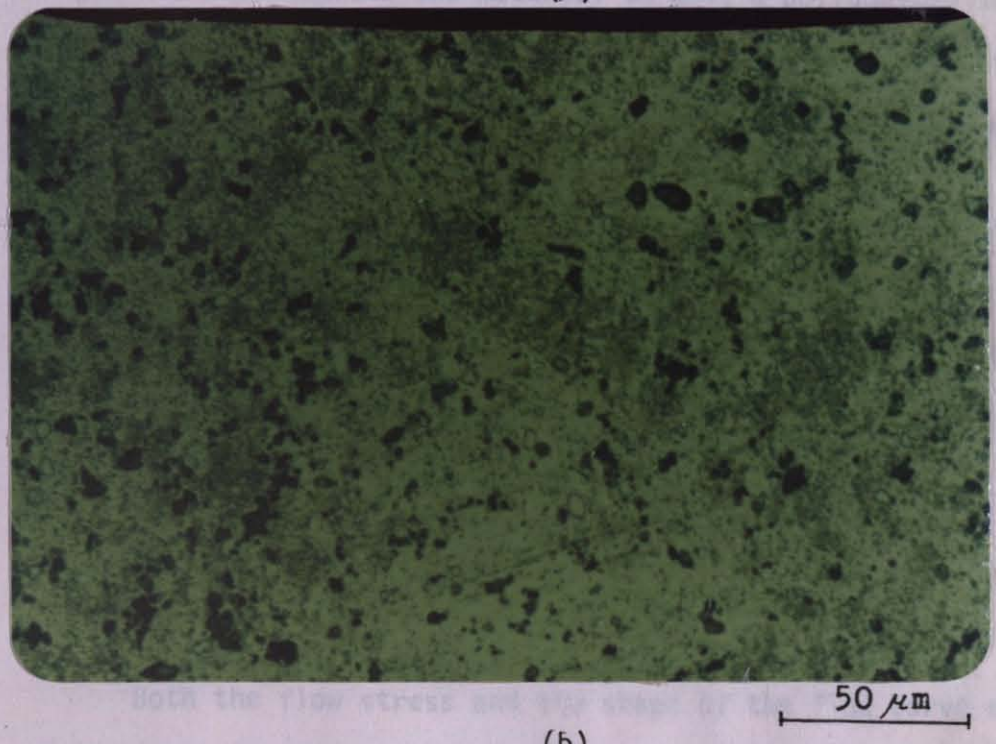

(b)

Figure 30 - Aluminum alloy 2024, after hot-torsion at 350°C and cooling in air, magnification 500 X. Deformation rates:
(a) $\dot{\gamma}^{*} = 6.84 \times 10^{-}$ rad/s, (b) $\dot{\gamma}^{*} = 0.694$ rad/s.

VII. DISCUSSION

The high temperature deformation behavior of aluminum has been studied extensively in recent years /7,24,26-28,55-60/. It is now well established that dynamic recovery, a kind of thermal softening mechanism, operates during hot-deformation of aluminum and its alloys. The characteristic feature of dynamic recovery is the formation of subgrains, which causes the material to have a polygonized structure. Due to the replacement of strained grains by the new strain-free subgrains, metal can be deformed up to high strains without cracking.

The flow curves specific to aluminum-base materials exhibit an interaction between strain hardening and dynamic-recovery-originated thermal softening processes. Factors such as temperature, strain rate, chemical composition etc. affect the occurence of these two opposite processes and, in turn, the flow behavior of material.

7.1 DEFORMATION BEHAVIOR

7.1.1 Effects of Temperature

Both the flow stress and the shape of the flow curve of aluminum-base materials are highly affected by temperature (Figures 20 and 21).

The decrease of flow stress with increasing temperature may be

explained by the increased movement ability of dislocations. As temperature gets higher, the movement of dislocations on their slip planes becomes easier and this causes the metal to deform under the effect of lower stresses. Additionally, dislocations gain the ability of climbing and cross-gliding, which gives them power to bypass the obstacles and to travel greater distances in response to the existing stress field.

As can be best seen from Figures 21(c) and 21(d), the peak of flow curve tends to move towards higher strain values with increasing temperature. This is a result of increased rate of dislocation annihilation, whose interference with the rate of dislocation generation determines the strain hardening exponent. Parallel to the increase of temperature, strain hardening exponent decreases and this results in the movement of the peak towards high strains.

7.1.2 Effects of Strain Rate

Figures 22 and 23 show the effects of strain rate on the deformation behaviors of aluminum 1100 and aluminum alloy 2024 at high temperatures.

Similar to the effect of temperature rise, the decrease of strain rate lowers the flow stress of both materials. It has been stated /55/ that the dislocation density almost remains constant, but the size of dislocation cells increases with the decrease of strain rate. If the dislocation density does not change substantially one should conclude that the decrease of flow stress caused by the low strain rate is due to the increase of the size of the dislocation

cell structure and to the decreased rate of movement of the moving individual dislocations.

Low strain rates require longer time intervals for a certain amount of deformation, thereby increasing the probability of the replacement of dislocation obstacles that have left their places by the new ones. As a consequence, the rate of diminishing of flow curve after peak value is passed becomes lower for low strain rates. This effect can be best seen from Figures 23(a) and 23(b).

7.1.3 Effects of Alloying Elements

There exists a perceptible difference between the flow curves of aluminum 1100 and aluminum alloy 2024 (Figures 20, 21, 22 and 23). Although recovery is the dynamic restoration mechanism for both metals, its amount decreases with the amount of alloying elements, which lowers the stacking fault energy /61,62/. Therefore, the alloy 2024 has higher strength and lower ductility than aluminum 1100, and it tends to fracture at high strain values where aluminum 1100 approaches to a steady-state deformation regime.

7.2 MICROSTRUCTURES

Aluminum has the highest stacking fault energy among all fcc metals /26/ and, like other metals of high stacking fault energy, it undergoes dynamic recovery in the deformation zone and static recrystallization in the cooling zone.

Since the microstructures observed in the present study were

taken after hot torsion followed by cooling in air, they reflect the statically recrystallized condition of materials

The initial microstructures of two materials shown in Figures 24 and 28 should be somehow different from those existing at the start of deformation. This is because of the long time elapsed during heating and holding periods prior to testing.

In Figures 26 and 27, the variation of microstructures from surface to center are shown for deformed and statically recrystallized aluminum 1100. The larger size of grains in near-axis region may be due to the relatively high temperature of this zone during cooling period. Another possible explanation of this might be the high rate of recrystallization in highly deformed near-surface region, since an increase in recrystallization rate with strain is accompanied by a decrease in recrystallized grain size /62/.

At relatively lower temperatures, recrystallization never starts or cannot continue after strating (Figure 25).

It is well known /17,62/ that addition of alloying elements have an effect of retardation on recrystallization. This is mainly due to the drag effect of impurity atoms on moving grain boundaries. An increase in solute concentration can also affect recrystallization indirectly through its influence on the preceding recovery process. No perceptible recrystallization exists in the microphotographs of deformed aluminum alloy 2024 (Figures 29 and 30).

In Figure 31, two microphotographs taken from the surface of deformed aluminum 1100 specimens are shown. These were taken for the

search of a critical radius zone, where stress becomes independent of material properties, on the microstructure. Although no sign of such a specific region exists in Figure 31(a), a transition zone between fine- and coarse-grained regions is apparent in Figure 31(b) and this zone matches with the critical radius. Transition regions of this type exist also in places different from critical radius zone. Keeping this fact in view, it can only be pointed out that the existence of a critical radius zone with an outstanding microstructural feature is a matter open to discussion. It requires a more detailed investigation at the level of electron microscopy.

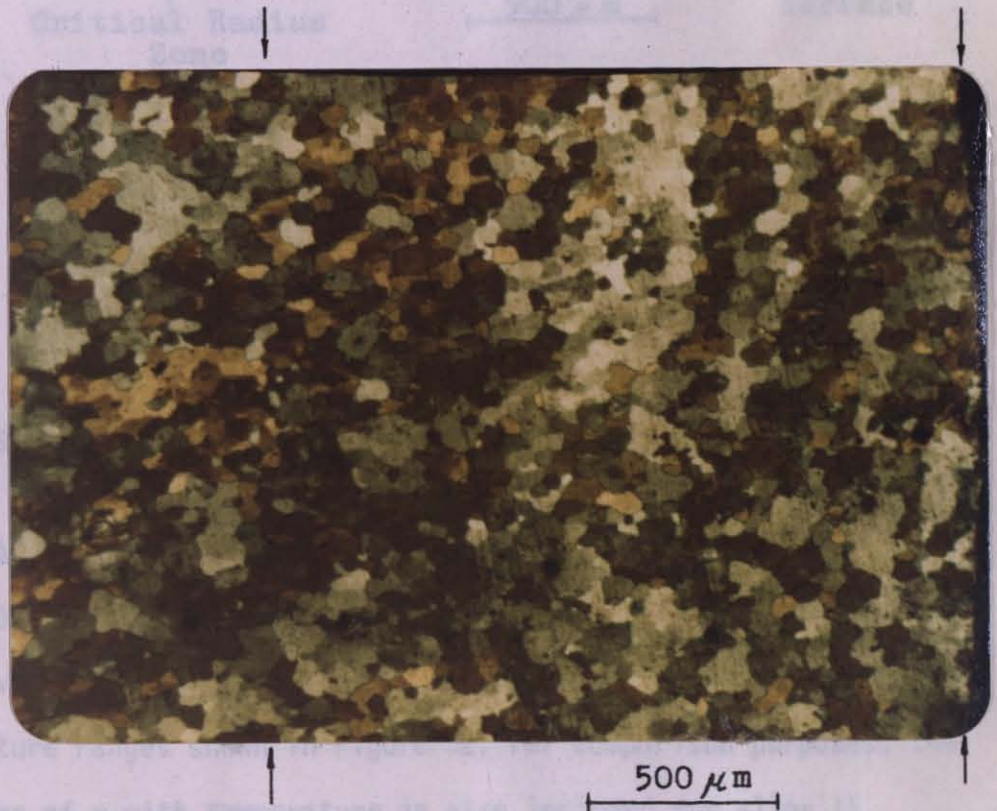

(a)

(b)

Figure 31 - Aluminum 1100, after hot-torsion at 450°C followed by cooling in air, polarized light, magnification 50 X. Deformation rates: (a) $\dot{\bar{\gamma}}^{*} = 0.694$ rad/s, (b) $\dot{\bar{\gamma}}^{*} = 6.84 \times 10^{-3}$ rad/s.

7.3 STRAIN RATE SENSITIVITY

As temperature increases, both aluminum 1100 and aluminum alloy 2024 become more strain-rate-sensitive. Their strain rate sensitivity coefficients (m) exhibit a linear increase in the temperature ranges shown in Figure 32. For comparison purposes, the variation of m with temperature is also included for alloy 1S (chemical composition (wt %) : Cu (0.002), Fe (0.7), Mg (<0.001), Si (0.05), Ti (0.002), Zn (<0.001), Ga (0.007), V (0.004), B (4 ppm), Al (balance)) /20/. This material shows similar behavior to aluminum 1100, probably due to their nearness in aluminum content.

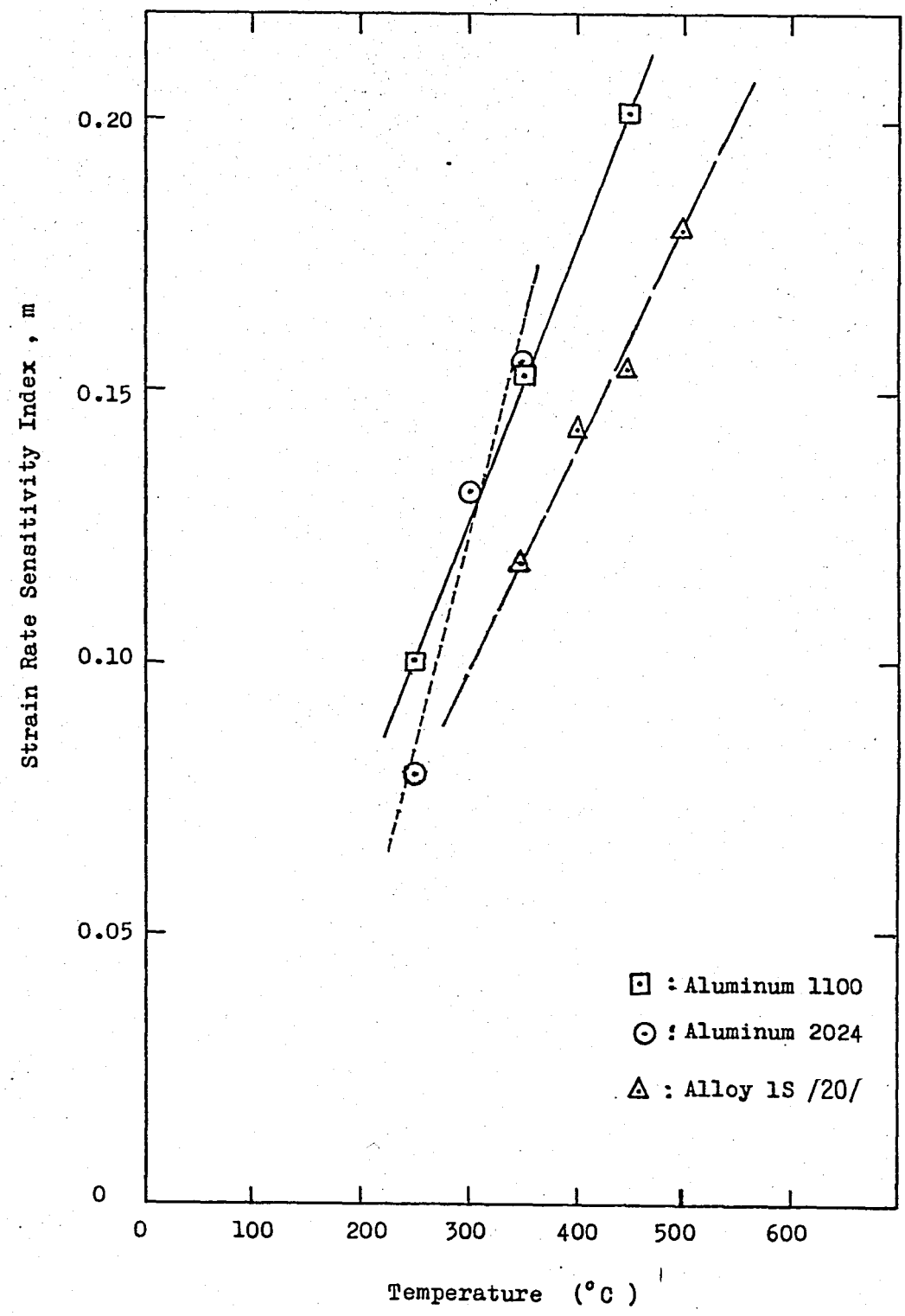

Figure 32 - Variation of Strain Rate Sensitivity Index with Temperature.

7.4 LENGTH CHANGE

During hot-torsion axial stresses develop and if free end testing is applied these stresses result in length changes, shortening for most of the materials including steels and lengthening for aluminum /15/. The origin of the axial stresses is still uncertain, although it has been attributed to anisotropy and texture development in the specimens /5,17,63/.

In the present study, specimens of aluminum 1100 exhibited outstanding length changes (Figure 33). The lengths of those made of less ductile aluminum alloy 2024, on the other hand, could not be measured because of their fracture during testing.

As can be seen from Figure 33, the length changes of aluminum 1100 specimens are of high levels for low strain rate and high temperature condition. This may probably result from the ease of texture developments at high temperatures and from the increased time interval for a certain amount of deformation, which allows for texture developments.

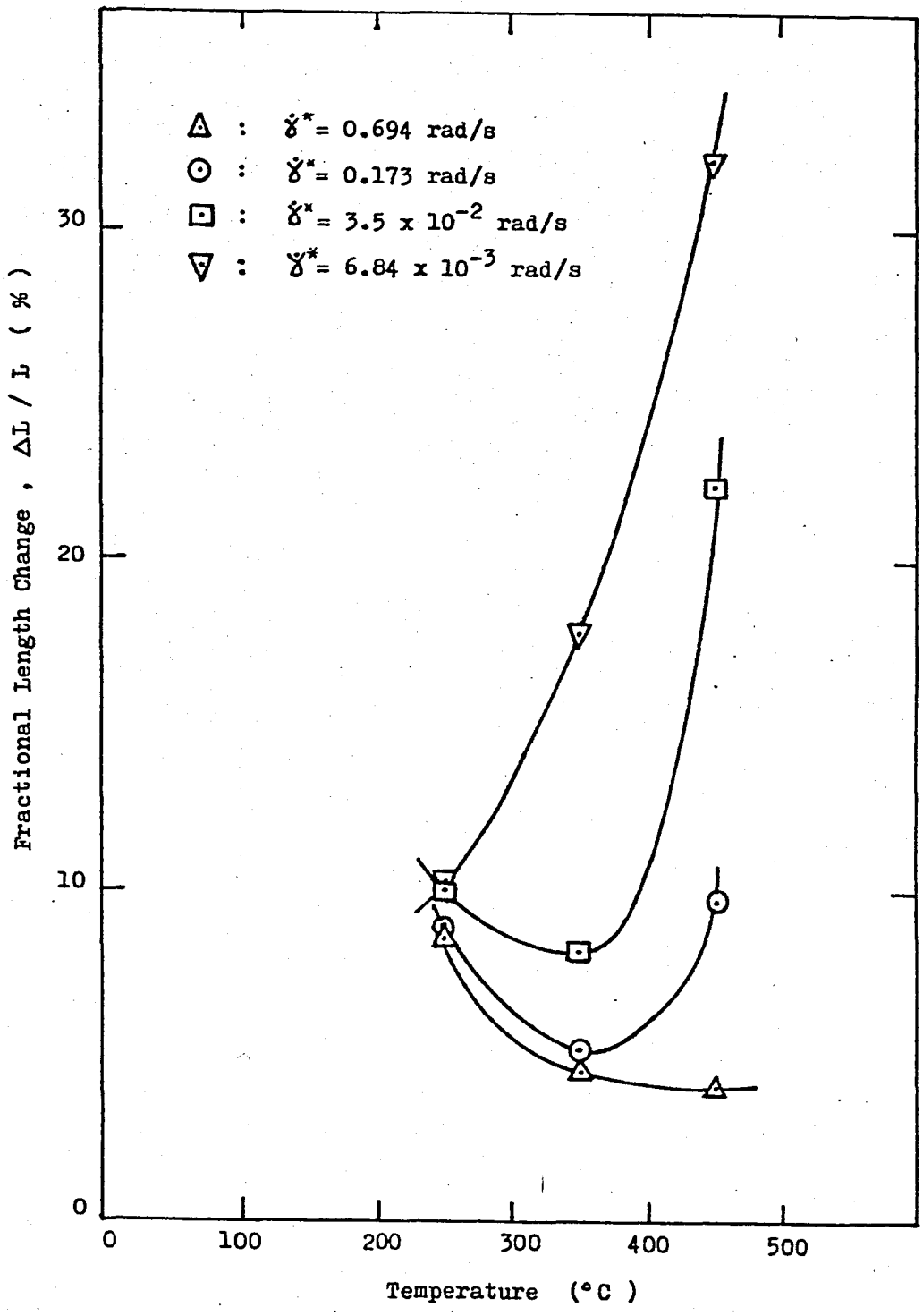

Figure 33 - Effects of Temperature and Strain Rate on the Length Changes of Aluminum 1100 Specimens During Hot-Torsion Testing.

VIII. CONCLUSION

i. For aluminum 1100 and aluminum alloy 2024, both the magnitude of flow stress and the shape of flow curve are highly dependent on temperature and strain rate during hot-deformation.

ii. As a result of the interaction between strain hardening and thermal softening mechanisms, flow curves of both materials pass through a peak value, after which aluminum alloy 2024 tends to fracture while aluminum 1100 approaches to a steady-state deformation.

iii. During a hot-torsion testing the length of the deformation zone cannot be restricted to a predetermined value. Deformation extends into neighbouring zones and this extension increases with increasing temperature.

iv. The length of aluminum 1100 specimens increase during free-end hot-torsion testing. The length change is maximum for the "high temperature and low strain rate" condition.

APPENDIX A

TABLE IV - Torque-twist angle data of aluminum 1100 for $\dot{\theta}$=2.233 rad/s.

Temperature: 250°C		Temperature: 350°C		Temperature: 450°C	
M (Nm)	θ (Radian)	M (Nm)	θ (Radian)	M (Nm)	θ (Radian)
28.00	0.40	12.00	0.28	7.00	0.40
31.00	0.43	13.00	0.38	7.60	0.70
32.00	0.60	13.50	0.60	7.80	1.16
32.20	0.90	14.00	0.94	8.00	2.29
32.00	1.93	14.50	1.53	7.90	3.03
31.50	4.30	14.90	2.21	7.80	3.50
31.00	5.80	14.85	2.70	7.70	4.09
30.50	7.90	14.75	3.42	7.60	4.92
30.00	9.56	14.50	4.30	7.50	5.85
29.50	11.68	14.30	5.13	7.40	6.59
29.00	13.19	14.00	6.78	7.30	8.35
28.00	15.65	13.75	8.90	7.20	10.16
27.00	18.20	13.50	10.70	7.10	12.09
26.00	20.43	13.40	11.40	7.00	13.74
25.00	22.91	13.20	13.50	6.90	15.53
24.00	25.10	13.00	15.75	6.80	17.20
23.00	27.38	12.75	18.75	6.70	19.30
22.00	29.63	12.50	21.00	6.60	21.20
21.00	31.60	12.30	23.50	6.50	23.50
20.40	32.82	12.00	27.10	6.40	26.43

TABLE V - Torque-twist angle data of aluminum 1100 for $\dot{\theta} = 0.558$ rad/s.

Temperature: 250°C		Temperature: 350°C		Temperature: 450°C	
M(Nm)	θ (Radian)	M(Nm)	θ (Radian)	M(Nm)	θ (Radian)
28.00	0.78	11.70	0.48	5.50	0.45
28.50	0.95	11.80	0.57	5.80	0.55
28.60	1.17	11.90	0.62	5.90	0.62
28.80	1.65	12.00	0.76	6.00	0.87
29.00	2.16	12.15	1.21	6.03	0.92
29.00	2.66	12.00	1.84	6.03	1.42
28.80	3.20	11.80	2.42	6.00	1.59
28.50	4.65	11.50	3.25	5.90	2.58
28.00	6.80	11.30	4.00	5.80	4.08
27.50	8.85	11.00	5.95	5.70	5.89
27.00	10.82	10.80	8.10	5.60	7.55
26.50	12.40	10.70	9.55	5.50	9.50
26.00	13.90	10.50	12.00	5.40	11.56
25.50	15.62	10.40	14.29	5.30	13.80
25.00	17.02	10.25	16.02	5.20	15.74
24.50	18.70	10.20	17.30	5.10	17.88
24.00	20.00	10.00	18.95	5.00	19.76
23.50	21.60	9.80	21.70	4.90	22.30
23.00	22.90	9.60	24.80	4.80	24.48
22.00	25.78	9.40	27.96	4.70	27.40

TABLE VI - Torque-twist angle data of aluminum 1100 for $\dot{\theta} = 0.112$ rad/s.

Temperature: 250°C		Temperature: 350°C		Temperature: 450°C	
M(Nm)	θ (Radian)	M(Nm)	θ (Radian)	M(Nm)	θ (Radian)
22.00	0.77	8.00	0.45	3.90	0.42
23.00	0.82	8.25	0.50	4.00	0.53
23.25	0.90	8.70	0.62	4.10	0.64
23.50	1.43	8.85	0.81	4.20	0.81
23.20	2.50	8.95	1.03	4.30	1.53
23.00	3.18	8.95	1.69	4.32	2.00
22.50	4.30	8.80	2.46	4.30	2.80
22.00	5.75	8.50	3.90	4.20	4.07
21.50	7.48	8.30	5.00	4.10	5.69
21.00	9.31	8.20	5.70	4.00	7.99
20.50	10.95	8.10	6.70	3.90	10.40
20.00	12.88	8.00	8.23	3.80	12.13
19.50	15.00	7.90	9.90	3.70	14.42
19.00	17.22	7.80	11.40	3.60	16.12
18.50	19.74	7.70	13.70	3.50	18.26
18.00	21.80	7.60	15.40	3.40	20.17
17.50	24.26	7.50	17.00	3.30	22.20
17.00	26.70	7.40	18.90	3.20	24.00
16.50	29.30	7.30	20.80	3.10	25.78
16.00	33.10	7.20	23.00	3.00	27.79

TABLE VII - Torque-twist angle data of aluminum 1100 for $\dot{\theta} = 0.022$ rad/s.

Temperature: 250°C		Temperature: 350°C		Temperature: 450°C	
M(Nm)	θ (Radian)	M(Nm)	θ (Radian)	M(nm)	θ (Radian)
20.00	0.78	7.00	0.78	3.00	0.57
21.00	0.86	7.10	0.83	3.10	0.68
21.50	1.10	7.30	0.94	3.20	0.98
21.85	1.31	7.40	1.07	3.30	1.36
21.50	3.05	7.50	1.27	3.40	1.65
21.00	5.11	7.50	2.21	3.43	2.00
20.50	6.76	7.40	3.53	3.43	3.61
20.00	8.18	7.30	4.90	3.40	4.51
19.50	10.20	7.20	6.26	3.30	6.60
19.00	11.60	7.10	7.40	3.20	7.75
18.50	13.40	7.00	8.58	3.10	9.00
18.00	14.94	6.90	9.93	3.00	10.05
17.50	16.44	6.80	11.30	2.90	11.52
17.00	17.85	6.70	12.60	2.80	12.58
16.50	19.40	6.60	14.00	2.70	13.84
16.00	21.00	6.50	15.10	2.60	14.62
15.50	23.18	6.40	16.30	2.40	16.90
15.00	24.90	6.20	17.70	2.20	19.59
14.50	27.50	6.10	19.75	2.00	22.30
13.75	32.50	6.00	21.10	1.80	25.50

TABLE VIII - Torque-twist angle data of aluminum alloy 2024 for $\dot{\theta}$ = 2.233 rad/s.

Temperature: 250°C		Temperature: 300°C		Temperature: 350°C	
M(Nm)	θ (Radian)	M(Nm)	θ(Radian)	M(Nm)	θ(Radian)
60.00	0.45	37.00	0.28	20.00	0.18
61.00	0.65	38.00	0.33	24.00	0.40
62.00	0.90	39.00	0.49	25.00	0.72
62.50	1.08	39.50	0.66	26.00	1.07
63.00	1.23	40.00	0.97	26.50	1.34
63.50	1.46	40.20	1.18	27.00	1.73
64.00	1.80	40.40	1.48	27.50	2.03
64.25	2.50	40.50	1.80	28.00	2.61
64.00	3.35	40.40	2.50	28.25	2.90
63.50	4.00	40.20	3.15	28.25	4.60
63.00	4.48	40.00	3.63	27.50	5.92
62.50	4.95	39.50	4.45	27.00	6.52
62.00	5.40	39.00	5.00	26.50	7.27
61.50	5.83	38.50	5.72	25.50	8.44
61.00	6.20	38.00	6.36	24.50	9.70
60.50	6.63	37.50	7.05	23.50	10.68
60.00	7.00	37.00	7.70	22.50	11.90
59.00	7.70	36.50	8.39	21.50	12.88
58.00	8.27	36.00	8.96	20.50	13.65
57.00	8.80	35.00	10.21	19.60	14.05

TABLE IX - Torque-twist angle data of aluminum alloy 2024 for $\dot{\theta} = 0.558$ rad/s.

Temperature: 250°C		Temperature: 300°C		Temperature: 350°C	
M(Nm)	θ (Radian)	M(Nm)	θ (Radian)	M(Nm)	θ (Radian)
51.50	0.43	29.00	0.34	15.00	0.22
52.50	0.61	30.00	0.44	20.00	0.39
53.00	0.81	31.00	0.58	21.00	0.60
54.00	1.00	32.00	0.72	21.50	0.84
55.00	1.45	33.00	0.97	22.00	1.14
55.50	1.84	34.00	1.40	22.50	1.45
56.00	2.35	34.50	1.75	23.00	2.03
56.50	3.20	35.00	2.41	23.50	2.76
56.25	4.08	35.25	3.33	23.50	3.65
56.00	4.49	35.00	4.30	23.00	4.91
55.00	5.66	34.50	5.58	22.75	5.30
54.50	6.13	34.00	6.30	22.00	6.37
54.00	6.54	33.50	7.06	21.50	6.90
53.50	6.98	33.00	7.79	21.00	7.55
53.00	7.38	32.50	8.42	20.00	8.60
52.50	7.73	32.00	8.98	19.50	9.09
52.00	8.12	31.50	9.86	18.50	9.93
51.00	8.90	31.00	10.40	18.00	10.30
50.00	9.64	30.50	11.19	17.50	10.52
49.50	9.96	30.00	11.82	17.25	10.61

TABLE X - Torque-twist angle data of aluminum alloy 2024 for $\dot{\theta} = 0.112$ rad/s.

Temperature: 250°C		Temperature: 300°c		Temperature: 350°C	
M(Nm)	θ (Radian)	M(Nm)	θ (Radian)	M(Nm)	θ (Radian)
45.00	0.28	24.00	0.39	15.00	0.30
47.50	0.37	25.00	0.45	16.00	0.52
49.00	0.50	26.00	0.53	16.50	0.75
50.00	0.62	27.00	0.82	17.00	1.05
50.50	0.73	28.00	1.36	17.50	1.45
51.00	0.90	28.50	1.88	18.00	1.85
51.50	1.25	29.00	3.00	18.50	2.38
52.00	2.01	28.50	4.50	18.80	2.84
52.00	3.01	28.00	5.37	18.95	3.07
51.50	3.76	27.50	6.11	18.95	4.12
51.00	4.34	27.00	6.69	18.85	4.56
50.50	4.76	26.50	7.29	18.50	5.33
50.00	5.22	26.00	7.97	18.00	6.16
49.50	5.84	25.50	8.63	17.50	6.88
49.00	6.30	25.00	9.28	17.25	7.22
48.50	6.70	24.50	10.03	16.50	8.20
48.00	7.10	24.00	10.60	15.50	9.44
47.50	7.50	23.50	11.20	15.00	9.74
47.00	7.91	23.00	11.72	14.50	10.15
46.50	8.51	22.50	12.18	14.00	10.56

TABLE XI - Torque-twist angle data of aluminum alloy 2024 for $\dot{\theta} = 0.022$ rad/s.

Temperature: 250°C		Temperature: 300°C		Temperature: 350°C	
M(Nm)	θ (Radian)	M(Nm)	θ (Radian)	M(Nm)	θ (Radian)
42.50	0.36	12.00	0.30	7.00	0.38
43.00	0.40	14.00	0.42	7.50	0.48
44.00	0.54	15.00	0.56	8.00	0.70
44.50	0.90	16.00	0.73	8.50	0.86
44.90	1.42	17.00	0.99	9.00	1.03
44.50	2.70	18.00	1.32	9.50	1.21
44.00	3.41	19.00	1.77	10.00	1.43
43.50	4.05	20.00	2.35	10.50	1.65
43.00	4.65	21.00	3.10	11.00	1.88
42.50	5.09	22.00	4.40	11.50	2.16
42.00	5.60	22.60	6.01	12.00	2.45
41.50	5.98	22.00	7.75	12.50	2.80
41.00	6.48	21.50	8.70	13.00	3.22
40.00	7.37	21.00	9.08	13.50	3.74
39.50	7.75	20.50	10.12	14.00	4.67
39.00	8.36	20.00	10.82	14.30	5.90
38.50	8.57	19.50	11.55	14.30	7.60
38.00	8.94	19.00	12.27	14.00	9.02
37.50	9.35	18.50	12.91	13.50	9.85
37.00	9.75	18.00	13.40	13.00	10.42

APPENDIX B

```
 1    PROGRAM INTEG(INPUT,OUTPUT)
 2    PRINT*,' ENTER DELX'
 3    READ*,DELX
 4    PRINT*,DELX
 5    PRINT*,' ENTER R'
 6    READ*,R
 7    PRINT*,R
 8    PRINT*,' ENTER RN'
 9    READ*,RN
10    PRINT*,RN
11    PRINT*,' ENTER P'
12    READ*,P
13    PRINT*,P
14    IF (P.EQ.0.)STOP
15    INTEGRATION
16    SUM=0.
17    X=0.
18
19    X=X+DELX
20    SUM=SUM+(R/(R+RN-SQRT(ABS(RN*RN-X*X))))**((3+P)/P)*DELX
21    IF (X.LT.RN)GO TO 2
22    PRINT*,' THE INTEGRAL = ',SUM
23    GOTO 1
24    STOP
25    END

      PROGRAM-UNIT LENGTH              215B =  141
      CM STORAGE USED                632008 =  26240
      COMPILE TIME                   0.283 SECONDS

 ENTER DELX
.001
 ENTER R
7.5
 ENTER RN
3.5
 ENTER P
.1004
 THE INTEGRAL = 1.136498413875
 ENTER P
.153
 THE INTEGRAL = 1.377312615562
 ENTER P
.2016
 THE INTEGRAL = 1.552731508765
 ENTER P
.0795
 THE INTEGRAL = 1.018435283201
 ENTER P
.1317
 THE INTEGRAL = 1.287612707262
 ENTER P
.1554
 THE INTEGRAL = 1.386866888712
```

BIBLIOGRAPHY

1. Greasley, A.; Sheppard, T., "Flow Stress Mapping from Extrapolated Laboratory Data", Journal of Mechanical Working Technology, Vol.11, pp.201-214, 1985.

2. Eleiche, A.M.; Duffy, J., "Effects of Temperature on the Static and Dynamic Stress-Strain Characteristics in Torsion of 1100-0 Aluminum", International Journal of Mechanical Sciences, Vol.17, pp.85-95, 1975.

3. Shapiro, E.; Dieter, G.E., "High Temperature-High Strain Rate Fracture of Inconel 600", Metallurgical Transactions, Vol.1, pp. 1711-1719, June 1970.

4. Nicholas, T.; Lawson, J.E., "On the Determination of the Mechanical Properties of Materials at High Shear-Strain Rates", Journal of the Mechanics and Physics of Solids, Vol.20, pp.57-64, 1972.

5. Rao, K.P.; Doraivelu, S.M., "Flow Curves and Deformation of Materials at Different Temperatures and Strain Rates", Journal of Mechanical Working Technology, Vol.6, pp.63-88, 1982.

6. Deutsche Gesellschaft für Metallkunde, "Methods Used in the Determination of Hot Working Parameters", Atlas Der Warmformgebungseigenschaften von Nichteisenmetallen, Vol.1, Germany, pp.3-18, 1978.

7. Kortmann, J., "Ermittlung des Umformverhaltens von Aluminiumlegierungen im Torsionsversuch", Neue Hütte, Vol.22, No.7, pp. 371-375, July 1977.

8. Witzel, W., "Warmtorsionsversuche mit Reinaluminium(I)", Aluminium, Vol.58, No.10, pp.588-592, 1982.

9. Witzel, W., "Warmtorsionsversuche mit Reinaluminium (II)", Aluminium, Vol.58, No.10, pp. 664-669, 1982.

10. Kovacevic, R.; Funke, P., "Ermittlung der Formänderungsfestigkeit im Warmverdrehversuch", Stahl und Eisen, Vol.98, No.21, pp.1077-1081, 1978.

11. Semiatin, S.L.; Lahoti, G.D., "Deformation and Unstable Flow in Hot Torsion of Ti-6Al-2Sn-4Zr-2Mo-0.1Si", Metallurgical Transactions A, Vol.12A, pp.1719-1728, October 1981.

12. Chen, H.S.; Erdmann-Jesnitzer, F., "Warmtorsion zur Festigkeitssteigerung von Aluminium als Thermomechanisches TORREK-Verfahren", Metall, Vol.28, No.1, pp.13-21, January 1974.

13. Weiss, H.; Skinner, D.H.; Everett, J.R., "A Torsion Machine for Programmed Simulation of Hot Working", Journal of Physics: E, Scientific Instruments, Vol.6, pp.709-714, 1973.

14. Shapiro, E.; Dieter, G.E., "Fracture and Ductility in Hot Torsion of Nickel", Metallurgical Transactions, Vol.2, pp.1385-1391, May 1971.

15. Moore, P., "Methods for Studying Hot Workability: A Critical Assessment", Deformation Under Hot Working Conditions, Iron and Steel Institute, London, Special Report No:108, pp.103-106, 1968.

16. Ueki, M.; Horie, S.; Nakamura T., "Evaluation of Hot Workability of 5083 Alloy by the Torsion Test Using Tubular Specimens", Journal of Mechanical Working Technology, Vol.11, pp.355-364, 1985.

17. Sellars, C.M.; Tegart, W.J., "Hot Workability", International Metallurgical Reviews, Vol.17, pp.1-24, 1972.

18. Fulop, S.; Cadien, K.C.; Lutov, M.J.; McQueen, H.J., "A Servo-Controlled Hydraulic Hot-Torsion Machine for Hot Working Studies", Journal of Testing and Evaluation, Vol.5, pp.419-426, 1977.

19. McQueen, H.J.; Jonas, J.J., "Hot Workability Testing Techniques", Metal Forming,Interrelation Between Theory and Practice, A.L. Hoffmanner, Ed., Plenum Publishers, New York, pp.393-428, 1971.

20. Sheppard, T.; Wright, D.S., "Determination of Flow Stress: Part 1, Constitutive Equation for Aluminum Alloys at Elevated Temperatures", Metals Technology, pp.215-223, June 1979.

21. Sheppard, T.; Wright, D.S., "Determination of Flow Stress: Part 2, Radial and Axial Temperature Distribution During Torsion Testing", Metals Technology, pp.224-229, June 1979.

22. Lahoti, G.D.; Altan, T., "Prediction of Temperature Distributions in Axisymmetric Compression and Torsion", Transactions of the ASME, paper no.74-WA/Prod-10, pp.1-8, 1974.

23. Johnson, G.R., "Dynamic Analysis of a Torsion Test Specimen Including Heat Conduction and Plastic Flow", Journal of Engineering Materials and Technology, Vol.103, pp.201-206, July 1981.

24. Farag, M.M.; Sellars, C.M.; McG. Tegart, W.J., "Simulation of Hot Working of Aluminum", Deformation Under Hot Working Conditions, Iron and Steel Institute, London, Special Report No: 108, pp.60-67, 1968.

25. Faessel, A., "La Simulation du laminage par l'essai de torsion", C.I.T., No.4, 1976.

26. McQueen, H.J., "Deformation Mechanisms in Hot Working, Journal of Metals, pp.31-38, April 1968.

27. Cotner, J.R., McG. Tegart, W.J., "High Temperature Deformation of Aluminum-Magnesium Alloys at High Strain Rates", Journal of the Institute of Metals, Vol.97, pp.73-79, 1969.

28. Vaughan, T.B., "The Laboratory Simulation of an Aluminum Slab-Rolling Schedule", Deformation Under Hot Working Conditions, Iron and Steel Institute, London, Special Report No: 108, pp.68-77, 1968.

29. Hartley, C.S.; Srinivasan, R., "Constitutive Equations for Large Plastic Deformation of Metals", Journal of Engineering Materials and Technology, Vol.105, pp.162-167, July 1983.

30. Hart, E.W., "Consitutive Relations for the Nonelastic Deformation of Metals", Journal of Engineering Materials and Technology, pp.193-202, July 1976.

31. Spittel, M.; Neubaurer, S., "Betrachtungen zur Mathematischen Fliesskurvenformulierung", Neue Hütte, Vol.28, No.1, pp.21-25, January 1983.

32. Bogon, P.; Kandler, T.; Wagener, H.W., "Anwendungsbezogene Mathematische Beschreibung von Fliesskurven Metallischer Workstoffe", Draht, Vol.34, No.10, pp.483-487, 1983.

33. Beiss, P.; Broichhausen, J., "Warmformänderungsfestigkeit von Aluminiumwerkstoffen", Metall, Vol.33, No.6, pp.639-644, June 1979.

34. Grabianowski, A., "Anwendung Verschiedener Verformungsmasse zur Beschreibung der Fliesskurven von Eisen und Messing", Metall, Vol.37, No.11, pp.1133-1136, November 1983.

35. Miller, A.K.; Sherby, O.D., "A Simplified Phenomenological Model for Nonelastic Deformation: Predictions of Pure Aluminum Behaviour for Incorporation of Solute Strengthening Effects", Acta Metallurgica, Vol.26, pp.289-304, 1978.

36. Ghosh, A.K., "A Physically-Based Constitutive Model for Metal Deformation", Acta Metallurgica, Vol.28, pp.1443-1465, 1980.

37. Sheppard, T.; Wright, D.S., "Determination of Flow Stress: Part 1. Constitutive Equation for Aluminum Alloys at Elevated Temperatures", Metals Technology, pp.215-223, June 1979.

38. Pewelski, O.; Rasp, W.; Koropp, J., "Ein Universell Anwendbarer Algorithmus zur Interpolation von Fließkurven für Metalle", Archiv Für Das Eisenhüttenwesen, Vol.53, No.5, pp.169-176, May 1982.

39. Hockett, J.E., "On Relating the Flow Stress of Aluminum to Strain, Strain Rate, and Temperature, Transactions of the Metallurgical Society of AIME, Vol.239, pp.969-976, 1967.

40. Johnson, G.R.; Hoegfeldt, J.M.; Lindholm, U.S.; Nagy, A., "Response of Various Metals to Large Torsional Strains Over a Large Range of Strain Rates - Part 1: Ductile Metals", ASME Journal of Engineering Materials and Technology, Vol.105, pp.42-47, January 1983.

41. Johnson, G.R.; Hoegfeldt, J.M.; Lindholm, U.S.; Nagy, A., "Response of Various Metals to Large Torsional Strains Over a Large Range of Strain Rates - Part 2: Less Ductile Metals", ASME Journal of Engineering Materials and Technology, Vol.105, pp.48-53, January 1983.

42. Pöhlandt, K.; Tekkaya, A.E.; Lach, E., "Torsion Test on Solid and Tubular Specimens for Testing the Plastic Behaviour of Metals", Archiv Für Das Eisenhüttenwesen, Vol.55, No.4, pp.149-158, April 1984.

43. Nadai, A., Plasticity, McGraw-Hill, New York and London, pp. 126-128, 1931.

44. Swift, W.A.C., "The Acquisition and Processing of Torque-Twist Data in Torsion Testing with Overstrain", Strain, pp.161-172, October 1974.

45. Atanasiu, N.; Teodosiu, C., "Ermittlung der Umformeigenschaften von Aluminiumlegierungen im Torsionsversuch", Aluminium, Vol.55. pp.536-538, 1979.

46. Chait, R., "Flow and Fracture of High Strength Steels in Torsion", Journal of Testing and Evaluation, Vol.1, No.5, pp.435-438, September 1973.

47. Brown, M.W., "Torsional Stresses in Tubular Specimens", Journal of Strain Analysis, Vol.13, No.1, pp.23-28, 1978.

48. Fields, D.S.,Jr,; Backofen, W.A., American Society for Testing and Materials Proceedings, Vol.57, pp.1259-1272, 1957.

49. Canova, G.R.; Shrivastava, S.; Jonas, J.J.; Sell, C.G., "The Use of Torsion Testing to Assess Material Formability", Formability of Metallic Materials- 2000 A.D., ASTM STP 753, J.R.Newby and B.A. Niemeier, Eds., American Society for Testing and Materials, pp.189-210, 1982.

50. Barraclough, D.R.; Whittaker, H.J.; Nair, K.D.; Sellars, C.M., "Effect of Specimen Geometry on Hot Torsion Test Results for Solid and Tubular Specimens", Journal of Testing and Evaluation, Vol.1, No.3, pp.220-226, 1973.

51. Funke, p,; Preiser, H., "Aufnahme von Fliepkurven im Warmverdrehversuch", Archiv für das Eisenhüttenwesen, Vol.44, No.5, pp.363-368, May 1973.

52. Pöhlandt, K., "Testing Strain-rate-sensitive Materials in the Torsion Test", Materialprüfung, Vol.22, No.10, pp.399-406, October 1980.

53. Lach, E.; Pöhlandt, K., "Prüfung des plastischen Verhaltens Metallisher Werkstoffe im Torsionsversuch", Draht, Vol.33, No.11, pp.689-693, 1982.

54. Pöhlandt, K.; Tekkaya, A.E., "Testing the Plastic Behaviour of Bars and Thin Sheet by Torsion Tests", Matador, Birmingham/ GB, pp.1-7, 1985.

55. Samanta, S.K., "Dynamic Deformation of Aluminium and Copper at Elevated Temperatures", Journal of Mechanics and Physics of Solids, Vol.19, pp.117-135, 1971.

56. Stüwe, H.P., "Do Metals Recrystallize During Hot Working?", Deformation Under Hot Working Conditions, Iron and Steel Institute, London, Special Report No.108, pp.1-6, 1968.

57. Sedlacek, V., "Dynamische Erholung und Rekristallisation", Neue Hütte, Vol.22, No.9, pp.465-469, September 1977.

58. Raybould, D.; Sheppard, T., "Plastic Flow in Thermally Activated Mechanical-Working Processes", Journal of the Institute of Metals, Vol.101, pp.45-52, 1973.

59. Stüwe, H.P., "Dynamische Erholung bei der Warmverformung", Acta Metallurgica, Vol.13, pp.1337-1342, 1965.

60. Usui, E.; Inaba, T.; Shinano, N., "Influence of Mn and Mg Additions on Hot Deformation of Aluminum and Aluminum Alloys", Zeitschrift für Metallkunde, Vol.77, No.3, 1986.

61. McQueen, H.J., "The Experimental Roots of Thermomechanical Treatments for Aluminum Alloys", Thermomechanical Processing of Aluminum Alloys, Ed. by James G. Morris, TMS-AIME, 1979.

62. McQueen, H.J.; Jonas, J.J., "Recovery and Recrystallization During High Temperature Deformation", Treatise on Materials Science and Technology, R.J. Arsenault, Ed., Academic Press, New York, Vol.6. pp.393-493, 1975.

63. Montheillet, F.; Cohen, M.; Jonas, J.J., "Axial Stresses and Texture Development During the Torsion Testing of Al, Cu, and ∝- Fe", Acta Metallurgica, Vol.32, No.11, pp.2077-2089, 1984.